NEUTRAL PION AND ETA PRODUCTION

IN DEEP INELASTIC MUON SCATTERING AT 480 GEV

by

Erik J. Ramberg

Dissertation submitted to the Faculty of the Graduate School
of The University of Maryland in partial fulfillment
of the requirements for the degree of
Doctor of Philosophy
1989

Advisory Committee:

> Dr. George Snow, Chairman/Advisor
> Dr. A.D. Vernekar
> Dr. Victor Korenman
> Dr. O.W. Greenberg
> Dr. N. Hadley

ABSTRACT

Title of Dissertation: NEUTRAL PION AND ETA PRODUCTION
IN DEEP INELASTIC MUON SCATTERING AT 480 GEV

Erik Joel Ramberg, Doctor of Philosophy, 1989

Dissertation directed by: Dr. George Snow, Physics Dept.

In this thesis, the production of neutral pi mesons and eta mesons in muon deep inelastic scattering is studied. The energy of the incident muons averaged 480 Gev and two different targets were used–liquid hydrogen and liquid deuterium. Multiplicites of these mesons as a function of event variables are discussed. Fragmentation of the target into pi zero mesons is measured and described in the context of the Lund model.

Dedication

This thesis is dedicated to Phil Steinberg.
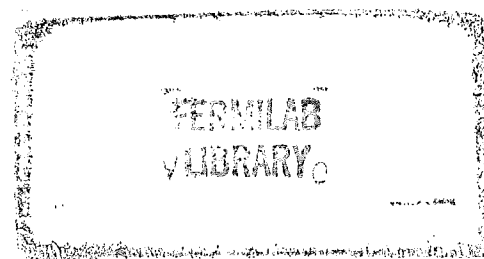
Acknowledgments

It has been my great fortune to have been helped by two outstanding advisors during my graduate career. I would like to acknowledge and thank Phil Steinberg for the immense impact he had on my development as a scientist. This thesis is dedicated to his memory. And I would like to thank George Snow for taking me the rest of the way.

Thanks to all you other guys, too. You know who you are.

Table of Contents

List of Tables

List of Figures

1. Introduction

1.1 Motivations and Goals

Physics is a field of science concerned with finding the rules by which the substance of the Universe behaves. Early in the history of their field, physicists concentrated on the study of objects that they encountered in their everyday world – falling objects, colliding objects, the behavior of sunlight, and electricity and magnetism. Steadily, however, physicists have either decreased or increased their scale so that now they postulate the existence of things that can never be seen; hidden universes or, in the case of high energy physicists, quarks. At these levels, one simply has to propose a model and repeatedly test it at every opportunity. If the model proliferates in extra parameters or limitations then one has to scrap it and start anew. Even if it doesn't suffer from these problems, it is possible that a completely different model will supplant it in the future. Besides the crucial requirement of experimental verifiability, a good model has one extra ingredient–it explains things succintly and to the point. Because the scale of modern-day physics is so vastly different from that which we are accustomed to, a model satisfying all these requirements is hard to come by. The research presented here is intended to test one prediction of a complex, multi-parameter model, the Lund model of subnuclear structure and interactions. The model's prediction is for the distribution in phase-space of final state pi-zero mesons in muon-nucleon deep inelastic scattering It will be tested using data from the experimental apparatus known as E665 at the Fermi National Accelerator Lab-

oratory.

The primary motivation behind this research is to test the theory of Quantum Chromodynamics, or QCD. This is the quantum gauge field theory of the color degree of freedom. Since color is postulated to be a property of quarks and since it is postulated that quarks are part of the substructure of nucleons, and since nucleons make up the vast majority of known matter then it follows that testing QCD is important if we wish to understand the structure of the Universe.

QCD provides one explanation of what a nucleon is composed of. The prediction of QCD is that it contains three valence quarks of different colors, with an attractive force between all three due to the color field. This color force field, as in the electric field, can be thought of as being carried by an intermediate particle, in this case the gluon (analogous to the photon for the electric field). Like the photon, the gluon can form virtual pairs of particles, a colored quark and a colored anti-quark. However, unlike the photon, which is chargeless, the gluon itself carries a color charge. Thus the nucleon is thought to be composed of a bound state of three valence quarks, an indeterminate and changing number of force carrying gluons, and a 'sea' of virtual quark-antiquark pairs. Even though QCD was formed as a theory in the mid 1970's, there have been no confirmed observations of free quarks or gluons. This is explained by the occurence of 'confinement', the postulate that the color field grows in magnitude

with separation of the interacting particles. It is as if they were connected by a stretched rubber band or string. Each end of this string is analogous to a quark. Confinement is then the statement that no matter how much energy you put into stretching a string you can never create a string with only one end—the most you can do is break the string. This is the idea behind the Lund model of QCD; quarks and gluons are joined by something analogous to a string. It is thus called a 'string model of QCD'.

Now, in high energy interactions, such as the deep inelastic scattering of a muon off of a nucleon, a large amount of energy is transferred to one of the constituent quarks. The subsequent fragmentation of the nucleon and production of final state particles will then be a function of several things:

1. The initial distribution of constituents.

2. Their initial motions and the forces between them.

3. How these constituents become separated from their parent nucleon and how new ones are formed.

4. How these fragments of original and newly formed constituents become attached again, and

5. How these reattachments are affected by the surrounding nucleons when this occurs in a heavy nucleus.

Deep inelastic scattering experiments are designed to study all these questions.

1.2 Deep Inelastic Scattering

1.2.1 A Short History of D.I.S.

In 1911, the Nobel Laureate Ernest Rutherford made the important discovery of the atomic nucleus by scattering alpha particles off a thin gold foil. This laid to rest the Thomson model of the atom which postulated a uniformly distributed positive charge and forced physicists to accept a pointlike concentration of positive charge in the center of every atom. Since then, nuclear scattering experiments have been solely concerned with uncovering the substructure of the nucleus from this pointlike exterior.

To do this, physicists rely heavily on the knowledge of electromagnetic interactions in the quantum realm. The most common technique has been to observe the interactions of a charged lepton with the nucleus of an atom when they exchange a virtual photon. As one increases the energy of the incoming lepton beam the maximum possible momentum of this virtual photon increases and, by the uncertainty principle, the smaller is the distance scale that one can explore.

Until the mid 1960's, the incoming lepton had been the electron. It is easily produced and easily manipulated. The ground-breaking experiments were at the Cornell synchrotron, with 2-GeV electrons, and at SLAC, with its 20-GeV linearly accelerated electrons. In a long series of experiments performed there and elsewhere, the elastic form factors of the nucleus were studied, giving

information on the distribution and motion of the protons and neutrons that resided there [1] . In the late 1960's SLAC performed a series of inelastic scattering experiments with their excellent electron beam and powerful detectors and conclusively proved that the nucleons in the nucleus had substructure. Bjorken showed that the data supported a model of the proton and neutron which had essentially freely moving charged constituents or 'partons' [2] . These partons have been usually associated with the postulated particle, the quark.

Since these experiments, no major advance in beam energy in deep inelastic scattering has been made with electrons. This is because of the enormous synchrotron radiation problems associated with the very low mass electron. The natural extension has been to use beams of very high energy muons. These are produced when pions, formed in high energy proton interactions, decay. Since it is easy to accelerate protons to high energies, these decay muons can then have very high energies indeed. The muon beam used in E665 has an average energy of 480 GeV. The advantage to using muons, besides their higher energy reach, is that the radiation length for muons is more than four orders of magnitude greater than for electrons. This means that the electromagnetic corrections for high energy muons are much less than for electrons. It also means that muons are highly penetrating particles and can be easily identified by this characteristic. The main disadvantage is that the quality of the beam is much poorer than for an electron beam due to the random nature of the pion decays. The

ways in which E665 has attempted to deal with the ever-present 'halo' of muons accompanying the beam is described below in the Apparatus section.

Despite the problems in producing and steering beams of muons, many of the major high energy laboratories in the world have done so. A short list of muon scattering experiments at the Bevatron, Brookhaven, SLAC, Serpukhov, CERN and Fermilab is given in Table 1 . (See also references [1,3] for more detailed discussions of some of these experiments). As can be seen, the available energy has increased one hundred fold and many targets and effects have been studied. E665 is the latest, and possibly the last, in the long history of muon deep inelastic scattering experiments.

1.2.2 The Fundamental Process

Any introduction to deep inelastic scattering theory begins with an obligatory Feynman diagram of the process and a discussion of the relevant variables. Conforming to this tradition I therefore begin with a Feynman diagram, shown here in Fig. 1 .

The incoming and outgoing muon have four-momenta labelled with unprimed and primed variables respectively. The photon that is exchanged between the charged muon and the charged parton inside the target has four-momentum q. The parton has four-momentum p which is some fraction x of the nucleon's four-momentum P. The resulting final state of the disintegrated nucleon has some characteristic invariant mass W^2 . Besides these variables, one can define

Table 1. Muon D.I.S. Experiments. This table gives a short historical
listing of muon scattering experiments that have been performed

Muon Scattering Experiments				
YEAR	GROUP	ENERGY	TARGET	INVESTIGATED
1961	Bevatron	2	Pb and C	μe universality
1968-74	Brookhaven	1.5 to 7.3	H	μe universality
1969	Harvard-McGill	$Q^2 < 1.8$	C	form factors
1971	Harvard	2	Pb	'trident' process
1974	SLAC-40" b.c.	16	H	ρ^o production
1975	SLAC-s.c.	14		recoil hadrons
1970-73	F.N.A.L. E26	150	Fe/scin.	Bjorken scaling
1976	Serpukhov	21		parity violations
1976-78	CHIO	150	Fe	final state analysis
	FNAL-Michigan	270	Fe	final state analysis
1979	BFP	270	Fe	ψ and charm production
	BCDMS	120-200	C	Weak-E.M. interference
1978-present	EMC	280	H/D/C/Fe	hadronic final states

two dimensionless scalars from relativistically-invariant products:

$$x = -\frac{q^2}{P \cdot q} \tag{1}$$

$$y = \frac{E - E'}{E} \tag{2}$$
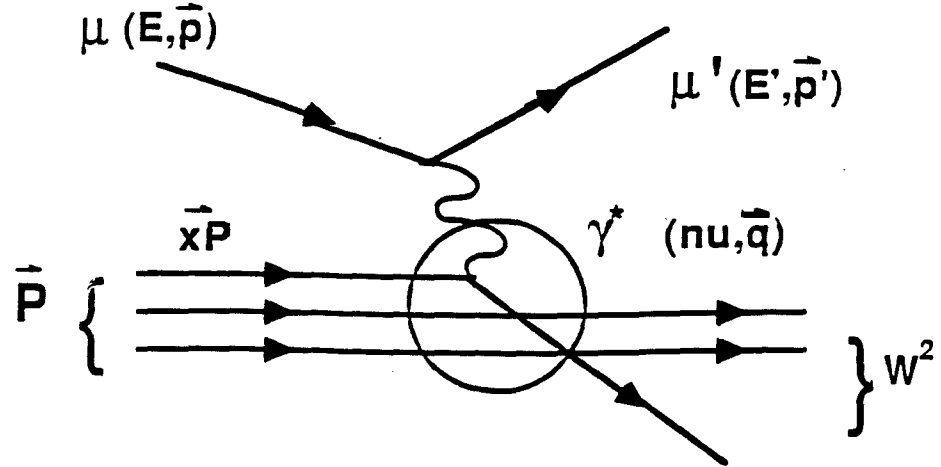
Figure 1. Deep Inelastic Scattering. The scattering of a muon off of a nucleon with an exchanged virtual photon.

One can make a simplistic argument to demonstrate the role of the first variable, called Bjorken x. If one postulates a mass m of the struck parton which carries a fraction ξ of the nucleons momentum, then:

$$(\xi P + q)^2 = m^2 \tag{3}$$

or

$$\xi^2 M^2 + 2\xi(P \cdot q) + q^2 = m^2 \tag{4}$$

If one neglects all masses, then:

$$\xi = \frac{-q^2}{2P \cdot q} = x \tag{5}$$

Thus x can be thought of as the fractional momentum of the struck parton in a high energy environment. It is also called the Bjorken scaling variable for reasons explained below. If one neglects only m, then ξ is:

$$\xi = \frac{2x}{[1 + (1 - \frac{4M^2}{q^2})^{\frac{1}{2}}]} \tag{6}$$

and is called the Nachtmann variable. It is sometimes used, instead of Bjorken x, in the analysis of structure functions. Besides these relations, the following is true (neglecting the mass of the muon):

$$Q^2 = -q^2 = 4EE' \sin^2(\frac{\theta_\mu}{2}) \tag{7}$$

$$\nu = E - E' \tag{8}$$

$$W^2 = (P + q)^2 = M^2 - Q^2 + 2M\nu \tag{9}$$

$$z = \frac{E_h}{\nu} \tag{10}$$

$$x_F = \frac{2 \cdot p_{par}}{W} \tag{11}$$

$$\eta = -\frac{1}{2} ln(\frac{E + p_{par}}{E - p_{par}}) \simeq -ln(tan\frac{\theta_\mu}{2}) \tag{12}$$

Q^2 is the mass squared of the virtual photon and ν is the energy it transmits to the parton. W^2 is the mass squared of the hadronic final state. The variable z is the fraction of the available energy carried by a final state hadron. x_F, or 'Feynman x', is the fraction of the available momentum in the center of mass system, carried by a final state hadron, that is parallel to the virtual photon direction. At large values of x_F, it is approximately equivalent to the variable z. Finally, η is called 'rapidity' and is a useful variable because for any Lorentz boost it transforms with an additive constant.

1.2.3 Scattering Theory and Structure Functions

In the scattering of subatomic particles, the quantity one measures is the probability of a given event as a function of relevant kinematical variables, i.e. the 'cross section' or its differential behavior. What follows below is a short explanation of the theory of cross sections in particle scattering for unpolarized particles.

In the simple case of one structureless Dirac particle, the muon for instance, scattering off of another, the process depends on one variable only – q^2, or the

momentum transfer. The differential cross section can be calculated exactly and turns out to be:

$$\frac{d\sigma}{dq^2} = \frac{4\pi\alpha^2}{q^4}\frac{E'}{E}\cos^2\frac{\theta}{2}(1 + \frac{Q^2}{2M^2}\tan^2\frac{\theta}{2}) \qquad (13)$$

which is the same as the Rutherford formula except for the second term, which is due to the recoil of the target. If the target particle is structureless but has electric and magnetic moments, then the differential cross section is modified slightly:

$$\frac{d\sigma}{dq^2} = \frac{4\pi\alpha^2}{q^4}\frac{E'}{E}\cos^2\frac{\theta}{2}(\frac{G_E^2 + \frac{Q^2 G_M^2}{4M^2}}{1 + \frac{Q^2}{4M^2}} + \frac{Q^2 G_M^2}{2M^2}\tan^2\frac{\theta}{2}) \qquad (14)$$

where G_E and G_M are the electric and magnetic form factors of the target. Now, if the target has structure as well, then one has to introduce an extra variable to allow for inelastic scattering and the formula becomes the following general one:

$$\frac{d^2\sigma}{dq^2 d\nu} = \frac{4\pi\alpha^2}{q^4}\frac{E'}{E}\cos^2\frac{\theta}{2}(W_2(q^2,\nu) + \frac{2W_1(q^2,\nu)}{\nu}\tan^2\frac{\theta}{2}) \qquad (15)$$

One can see how the structure functions W_1 and W_2 correspond to the form factors in the elastic case. These structure functions fully define the structure

of the target.

When one performs deep inelastic scattering using neutrinos as the lepton probe, the above theory is modified. The exchange particle in the interaction is one of the intermediate vector bosons, the W^+ or W^- in charged current interactions or the Z^o in neutral current interactions. In these weak interactions parity is not conserved and a new term can be introduced in the structure function. This term is proportional to

$$W_3(q^2, \nu) \sin^2 \frac{\theta}{2} \tag{16}$$

where W_3 is a new structure function analogous to W_1 and W_2.

1.2.4 The Parton Model

It was noticed in the experimental data from SLAC that the structure functions obtained from electron-proton scattering did not show a dependence on q^2, but only on x. This matched the prediction of Bjorken, which was based on his parton model of the nucleon [2].

Bjorken's parton model states simply that the nucleon is composed of structureless components, called partons. When viewed in the frame in which the nucleon has infinite momentum, the interaction of a lepton with these partons can be viewed as instantaneous and incoherent. The center of momentum frame of reference in high-energy deep inelastic scattering is a good approximation of this infinite momentum case, so we expect the model's predictions to hold true.

Bjorken showed that if one uses the following assumptions:

1. The partons are free inside the nucleon

2. Their mass and transverse momentum are negligible

3. The scattering process is incoherent and instantaneous

4. The longitudinal four-momentum of a parton is a fraction x_i of the proton's four-momentum:

$$p_i^\mu = x_i \cdot P^\mu \qquad (17)$$

then one can write down the following very general expression for W_2:

$$\nu W_2(\nu, q^2) = \sum_{N \, partons} P(N) \sum_{i=1}^{N} Q_i^2 \times \int_0^1 dx \, f_N(x) \, \delta(x - \frac{Q^2}{2M\nu}) \equiv F_2(x) \quad (18)$$

where P(N) is the probability of finding a given configuration N of partons, Q_i is the charge on a given parton, and $f_N(x)$ is the probability of finding a parton with momentum xP in this configuration. In this framework, F(x) is interpreted as the mean square of the charge of the partons times the probability of finding a parton with four-momentum p. Thus W_2 is now a function of only one variable, Bjorken x, and this function can be interpreted to yield the momentum distribution of partons inside the nucleon.

Figure 2 shows the original data from SLAC that support this idea of 'scaling' with the variable x [4] .

$$F(\omega) = \nu \frac{d^2\sigma/d\Omega dE'}{(d\sigma/d\Omega)_{MOTT}} \left[1 + 2\frac{1}{1+R}\left(1 + \frac{\nu^2}{Q^2}\right)Tan^2\frac{\theta}{2} \right]^{-1}$$
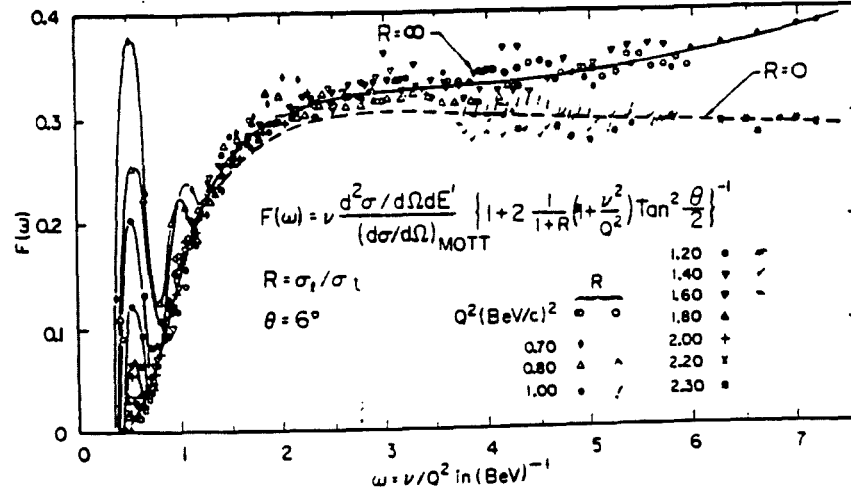
Figure 2. Bjorken Scaling. Q^2 Independence of Structure Functions

It can be shown in this framework that F_1 (which is now also a function only of x: $W_1(Q^2,\nu) = F_1(x)$) is no longer an independent function but is related to F_2, depending on the spin of the partons:

$$\frac{F_2 - 2xF_1}{F_2} = \frac{\sigma_L}{\sigma_T} = f(parton\ spin) \tag{19}$$

SLAC data has shown that F_1 is non-zero and that the ratio

$$R = \frac{\sigma_L}{\sigma_T} \tag{20}$$

is very small. [5] It follows from this that the nucleon is composed of relatively free spin 1/2 partons since the 'Callan-Gross' relation for spin 1/2 partons is that:

$$F_1(x) = 2xF_2(x) \tag{21}$$

The cross sections are now essentially given by the single structure function F_2. This relation does not hold exactly because all of the assumptions of the Parton Model are not correct. The partons making up the proton are not necessarily massless and are certainly not totally free in their motion. Other realities are that the partons exhibit random transverse motions, the so-called 'primordial k_T', and the scattering process is not instantaneous but exerts a force as the partons cross the nucleon. In addition, the presence of gluon bosons in the target nucleon also allow $\sigma_L \neq 0$ in a way predictable by QCD. The ratio R is then not exactly zero but approximately:

$$R \approx \frac{4\left\langle k_T^2 \right\rangle + m_q^2}{Q^2} \tag{22}$$

Figure 3 shows results for the value of R as a function of Q^2 [6]. The best fit to this data was used for correcting our Monte Carlo simulation.

1.2.5 QCD and the Parton model

Bjorken's parton model detailed above has been very successful indeed, and the identification of partons with spin 1/2 fractionally charged quarks has yielded
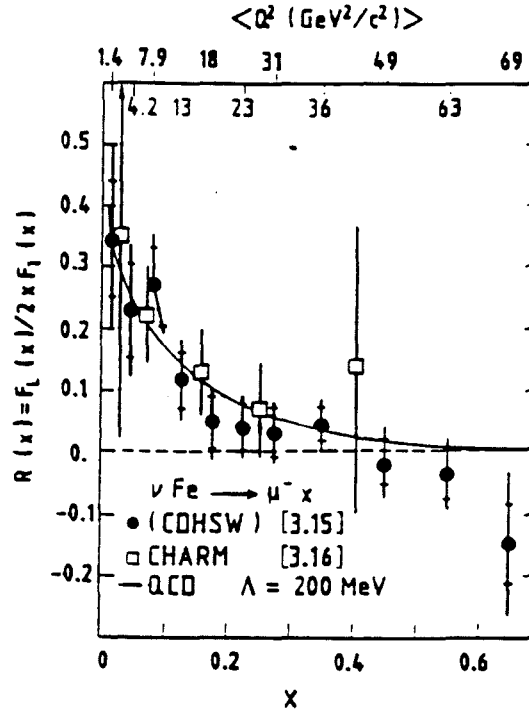
Figure 3.   Experimental Results for R.   The data from neutrino
scattering experiments CDHSW and CHARM shows a non-zero value
for R at low Q^2.

a consistent view of the interior of the neutron and proton that agrees with the

quantum field theory of QCD and is substantiated by data. Many reviews exist

concerning this subject and I will not go into too much detail concerning the

results of this 'quark parton model'. [6-9]

It was deduced from the properites of heavy, spin 3/2 hadrons that the

constituents of hadrons must carry an extra degree of freedom besides isotopic

spin, able to take on three values. This degree of freedom, called color and

represented by the gauge group SU(3), is an additional quantum number carried

by the partons, from now on to be identified as 'quarks'. From the highly symmetric grouping of hadrons into isospin-hypercharge multiplets, it has been deduced that quarks are arranged into at least three isospin doublets, with the famous labels (or 'flavors') up, down, strange, charm, top and bottom (u,d,c,s,t,b for short). Each quark carries color and it seems to be a rule of nature that a net color charge cannot exist in isolation. This means that hadrons must consist of a bound quark-antiquark pair, the mesons, or of three differently colored quarks, the baryons. The force between quarks is carried by the 'gluon' gauge boson and this force increases as the distance between quarks increases, keeping them locked permenantly inside the hadron with no identity possible outside that framework. This is called 'confinement'. The strength of the 'strong nuclear force' is on the order of the strong coupling constant:

$$\alpha_S(Q^2) \propto \frac{1}{ln(\frac{Q^2}{\Lambda^2})} \tag{23}$$

where Λ is an experimentally determined parameter which describes the scale of QCD. As can be seen, this 'running coupling constant' increases as Q^2 decreases. Using the Uncertainty Principle as a guide, this means that α_S increases as two quarks separate in distance. This is equivalent to the previous statement about quark confinement.

QCD is introduced into the parton model via the Altarelli-Parisi equations,

which describe the change in F_2 as a function of Q^2. [10] As was stated previously, F_2 is proportional to the sum of the square charge of the quarks times their momentum distributions:

$$F_2(x) = x \cdot [\frac{4}{9}(u(x) + \bar{u}(x)) + \frac{1}{9}(d(x) + \bar{d}(x)) + ...] \qquad (24)$$

where the fractions come from the square of the fractional charge of the quarks and where the sum runs over all flavors of quarks. The functions u(x), d(x), etc. are the probability distributions of finding a quark of a given flavor in the nucleon with a given x value. These quark distributions can be separately determined by doing the same scattering experiments off of hydrogen and deuterium targets, with the difference between the two being proportional to the difference of the 'valence' quark distributions, $u_v(x)$ and $d_v(x)$ in the proton:

$$\frac{1}{2}F_2^{\mu D} - F_2^{\mu H} = \frac{1}{2}(F_2^{\mu n} - F_2^{\mu p}) = \frac{-x}{6}(u(x) - d(x)) \qquad (25)$$

This result is obtained using the assumption that the proton and neutron are pure isospin partners of each other, with the u quark distribution in one being identical to the d quark distribution in the other.

Other combinations of structure functions obtained from neutrino and antineutrino data can be used to deduce u(x) and d(x) separately. The distribu-

tions for quarks other than the valence quarks, including the anti-quarks, are all lumped together under the heading of 'sea' quarks. The best results for the quark momentum distributions are shown in Fig. 4 [6]. It should be noted that g(x), the gluon momentum distribution, cannot be measured directly by charged lepton scattering experiments. Measurements of the momentum carried by the charged partons show, however, that the gluon field carries at least half of the net momentum of each nucleon [11].
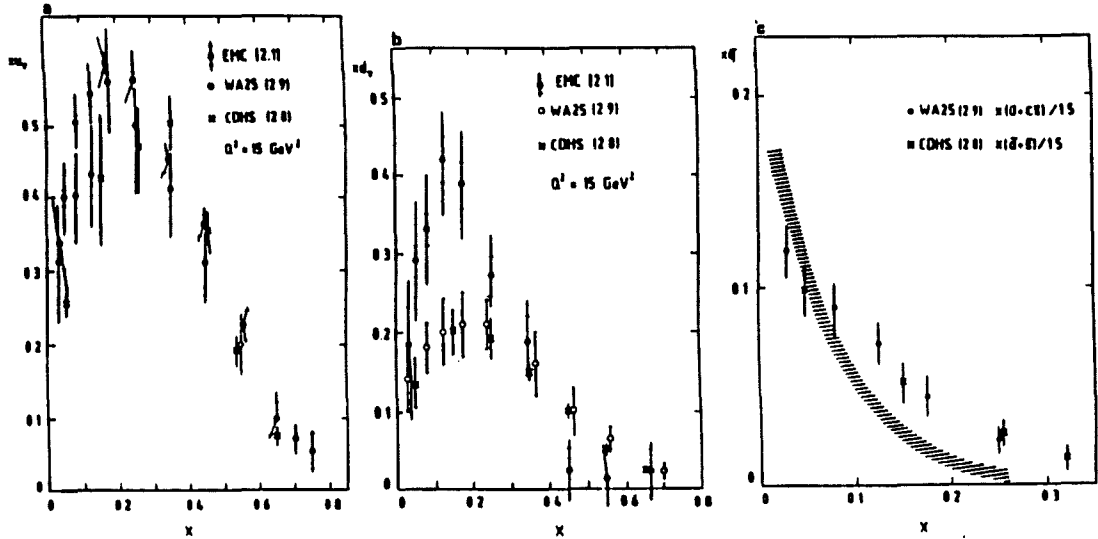
Figure 4. Quark Momentum Distributions. This figure shows the best data for quark momentum distributions. a) u valence quark distribution b) d valence quark distribution and c) sea quark momentum distribution (shaded area is fitted parametrization)

Since the value of the coupling constant α_S depends on Q^2, then so do the quark distributions and thus F_2. Figure 5 shows how $F_2(x)$ violates the

scaling behavior over a large range of Q^2 [6]. In fact, as Eqn. 23 would indicate, F_2 varies logarithmically with Q^2 . Calculating Λ from these scaling violations is practically an industry in itself. (See Ref. 12 for a recent example.) Most estimates lie in the range 100–300 Mev.
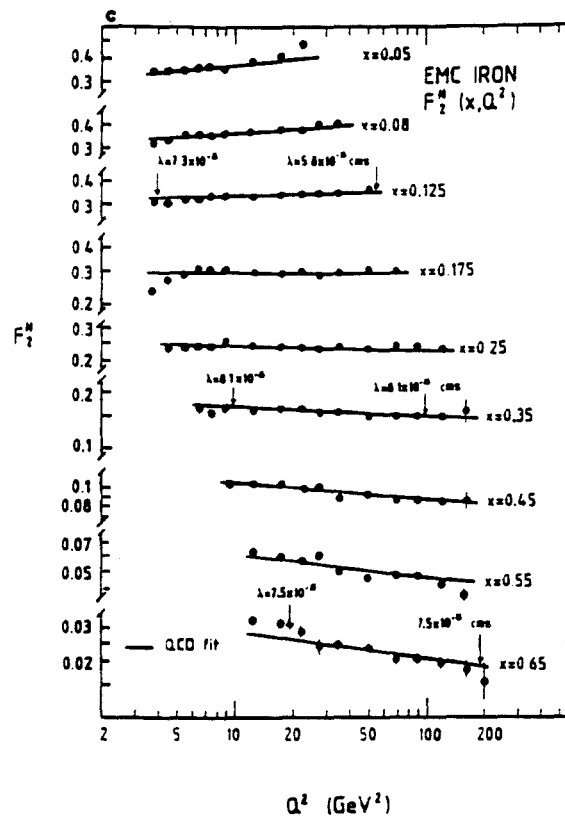
Figure 5. Change in F_2 with respect to Q^2. EMC data showing violations of the scaling behavior of F_2 for different x bins.

1.2.6 Fragmentation of the Nucleon

Now, the quark parton model may tell us approximately what a nucleon is composed of, but it tells us virtually nothing about how a nucleon disintegrates. The reason for this is that the forces get stronger in QCD as the quarks sepa-

rate so that the usual methods of perturbation theory can no longer work. To understand the process involved as envisioned by the Lund model, Fig. 6 shows schematically how, as the struck quark separates from the 'spectator' diquark, $q\bar{q}$ pairs are formed in the vacuum between, resulting eventually in mesons. (The Lund model takes into account the less likely possibility that two $q\bar{q}$ pairs are formed instead of one, resulting in baryons instead of mesons.) The energy for pair production comes from the strong gluon color field strung between all quarks and antiquarks. Essentially, it is the details of this gluon emission and subsequent quark formation that is at the heart of QCD theory. Finally, when there is no energy available for quark separation or formation, fragmentation stops.
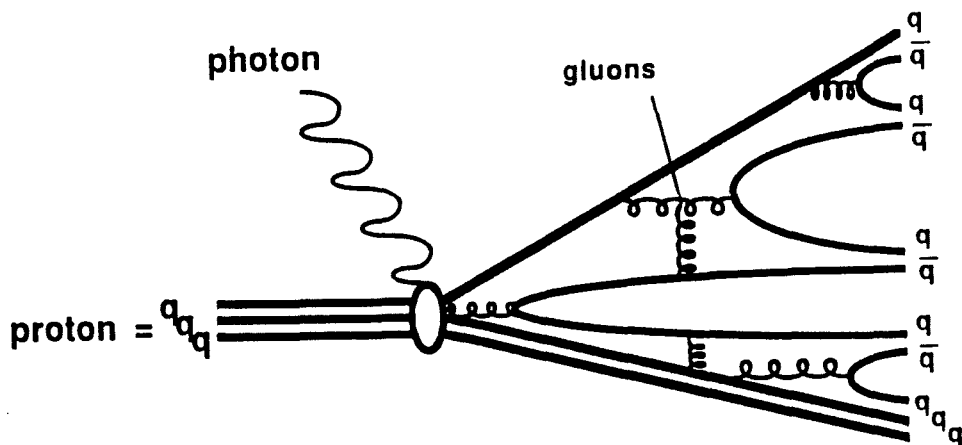
Figure 6.   Fragmentation of a Nucleon in the Lund Model.

Mathematically, one can describe the formation of final states of particles, which are combinations of the quarks and antiquarks formed as described, by

the following approximation:

$$\frac{d^3\sigma_h}{dx\,dQ^2\,dz} \approx F_2(x, Q^2) \cdot D_q^h(z, x, Q^2) \tag{26}$$

where $D^h(z, x, q2)$ is called the 'fragmentation function' and gives the probability of a quark q producing a hadron h with momentum fraction z in a deep inelastic scattering event with kinematic variables x and Q^2. It encapsulates all that is unknown in the process.

The transverse momentum with respect to the virtual photon direction of final state particles emerging from the collision can be modelled with a simple expression:

$$\left\langle p_T^2 \right\rangle^h = \left\langle p_T^2 \right\rangle_{frag} + \left\langle p_T^2 \right\rangle_{QCD} + z^2 \left\langle k_T^2 \right\rangle \tag{27}$$

where

$$\left\langle p_T^2 \right\rangle_{QCD} = \alpha_S(Q^2)\,g(x, y)\,Q^2 \approx \alpha_S(Q^2)\,W^2 \tag{28}$$

is a QCD calculable expression and the other two values describe the way in which primordial k_T and the transverse momentum of the fragmentation process itself show up in the final transverse momentum of the particles emerging from a scatter. It is to verify the values of these variables and check the validity of the QCD assumptions that are major thrusts of this thesis.

1.2.7 π^o Formation and Decay

Pi zero mesons are singled out for study in this thesis because they are a final state particle that can be readily identified, even up to quite high energies, by the electromagnetic calorimeter. The pi zero is an isospin 1, spin 0 meson whose mass is 135 Mev. The intrinsic width of the pi zero is 7.6 ev. It is postulated to contain a linear combination of up-anti up and down-anti down quarks.

To compare in detail the data for pi zero fragmentation results with a QCD prediction, the LUND model for deep inelastic scattering is used. This is described in the Software section. It should be noted, however, that some properties of pi zeros are able to be inferred from the theory given in the previous section. From simple isospin considerations, for example, one may predict that

$$\frac{d\sigma_{\pi^o}}{dx\,dy\,dQ^2} = \frac{1}{2}\Big(\frac{d\sigma_{\pi+}}{dx\,dy\,dQ^2} + \frac{d\sigma_{\pi-}}{dx\,dy\,dQ^2}\Big) \tag{29}$$

The average number of π^o's formed should increase with respect to the logarithm of W^2 because more energy is available in the laboratory frame of reference for production of final state particles. Pi zero formation should fall steeply with respect to the variables z and x_F because, during the formation process, fragmentation into those states with a higher percentage of the available center of mass energy are less probable. The same behavior should be seen with

respect to the transverse momentum because of the Gaussian type of fluctuations that produce p_T. Very little Q^2 dependence of the number of π^o's formed should be evident because of the scaling phenomenon discussed earlier. The low level of scaling violations should be evident only for high Q^2. This should be true of the p_T distribution as well.

From Eqn. 27 and Eqn. 28 we see that the average transverse momentum squared of identified pi zero mesons should increase with respect to W^2. This should also be true for z^2 or x_F. This is because the probability of gluon emission increases as the color field gets stronger. This is true for those cases where the struck quark has a large amount of energy, which occurs for large x_F or z. The p_T spectrum is then shifted toward higher values because of the added p_T of the gluon.

In the fragmentation process, the π^o will have some azimuthal angle ϕ around the virtual photon direction, as defined in Fig. 7 . The average value for cosine of ϕ should not be zero because of the preferred direction of gluon emission in the plane of the muon scatter. Thus, pi zeros produced in those events with large gluon emission, namely those events at higher z or x_F, will have a more negative average value of $\cos(\phi)$, reflecting the opposite direction of the hadron from the gluon direction. This behavior has been seen for charged particles in deep inelastic scattering by EMC. [13]

When a π^o is formed at the interaction point by the processes I have been
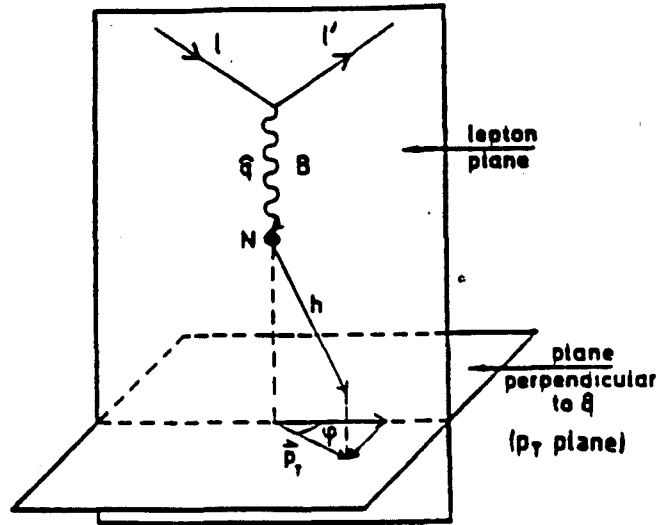
Figure 7. Azimuthal Angle of Hadron Production. This figure shows the plane of production in the lepton scattering process and how the angle ϕ is calculated for hadrons.

describing, it decays almost immediately, having a mean lifetime of $8.4 \cdot 10^{-17}$ seconds. At the speed of light, it can travel a few millionths of a cm during this interval. The dominant decay mode, occuring 98% of the time, is into two high energy photons, which can subsequently be detected by their showering in the electromagnetic calorimeter. The method of identification used in this thesis is to compare the invariant mass of these identified photons to the pi zero mass.

See references [14-17] for details of pi zero production in deep inelastic scattering.

1.2.8 η **Formation and Decay**

The η particle is very similar in its properties to the π^o. It has isospin 0 instead of isospin 1, but has spin 0 like the pi zero meson. Its mass is 548 Mev and it decays into two photons approximately 39% of the time. Its natural width is 1.1 Kev. It is postulated to contain a linear combination of up-anti up, down-anti down and strange-anti strange quarks in its structure. The other decay modes of the eta include a decay into three pions as well as into semileptonic modes. The yield of eta's in deep inelastic events should be much smaller than for pi zero's because of its larger mass and its strange component. The multiplicity of etas should show an increase with the logarithm of W^2, as for π^o's.

2. The Experimental Apparatus

2.1 Introduction

The experiment known as E665 at Fermi National Accelerator Laboratory is situated at the end of one and a half kilometers of beamline, the longest fixed-target beamline in the world as of this writing. This beamline forms and transports the highest energy muon beam, consisting of 480 GeV muons, at a rate of 10^6 muons per second during its highest luminosity. The experimental hall is called NMR or the 'New Muon Lab' and contains the experimental apparatus for one of the most massive fixed target scattering experiments at Fermilab. It consists of a multitude of separate detectors which were constructed by a loose consortium of international collaborating institutions. The institutions and the people employed by them to develop the experimental apparatus are detailed in Table 2 .

Despite this aggregation of separate and disparate tasks and viewpoints, the experiment is notably coherent in design, implementation and use.

The apparatus was based in part on the design of its precursor experiment, NA9, used by EMC, or the European Muon Collaboration, at CERN. In fact, the detectors in the vertex region of E665 are the same as those used by EMC, being transported here after the completion of that experiment. The design is planned around the two huge superconducting spectrometer magnets; the CVM, or 'CERN Vertex Magnet' which contains the target and streamer chamber

Table 2. E665 Participants. This table lists the participants in E665 and the institutions they work for.

E665 Collaboration
April 1989

M.R. Adams[7], S. Aid[6], P.L. Anthony[9], M.D. Baker[9], J.F. Bartlett[4], A.A. Bhatti[11],
H.M. Braun[12], T. Burnett[11], W. Busza[9], J.M. Conrad[6], G.B. Coutrakon[4,c], R. Davisson[11],
S.K. Dhawan[13], W. Dougherty[11], T. Dreyer[5], U. Ecker[12], V. Eckardt[10], M. Erdmann[5],
A. Eskreys[3], K. Eskreys[3], H.J. Gebauer[10], D.F. Geesaman[1], R. Gilman[1], M.C. Green[1,b], J. Haas[5],
C. Halliwell[7], J. Hanlon[4], V.W. Hughes[13], H.E. Jackson[1], D.M. Jansen[11], G. Jancso[10],
S. Kaufman[1], R.D. Kennedy[2], T. Kirk[4], H. Kobrak[2], S. Krzywdzinski[11,c], S. Kunori[6], J. Lord[11],
H.J. Lubatti[11], T. Lyons[9], S. Magill[7], P. Malecki[3], A. Manz[10], D. McLeod[7], H. Melanson[4],
D.G. Michael[6], W. Mohr[5], H.E. Montgomery[4], J.G. Morfin[4], R.B. Nickerson[6], S. O'Day[5],
A.M. Osborne[2,4,6,d], L. Osborne[9], B. Pawlik[3], F.M. Pipkin[6], E.J. Ramberg[8], A. Röser[12],
J. Ryan[9], A. Salvarani[2], M. Schmitt[6], K. P. Schüler[13], E. Sexton[2,7,c], H.J. Seyerlein[10],
A. Skuja[8], S. Söldner-Rembold[10], P.H. Steinberg[8,f], H.E. Stier[5], P. Stopa[10,g], P. Strube[10],
Robert A. Swanson[2], R.L. Talaga[5,h], S. Tentindo-Repond[1,i], H.-J. Trost[10,h], H. Venkataramania[13],
M. Vidal[10], M. Wilhelm[5], J. Wilkes[11], Richard Wilson[6], S. Wolbers[4], T. Zhao[11]

1 Argonne National Laboratory
2 University of California, San Diego
3 Institute of Nuclear Physics, Cracow, Poland
  & Institute of Nuclear Physics & Technology, Cracow, Poland
4 Fermi National Accelerator Laboratory
5 University of Freiburg i.Br.
6 Harvard University
7 University of Illinois at Chicago
8 University of Maryland, College Park
9 Massachusetts Institute of Technology
10 Max Planck Institute for Physics & Astrophysics, Munich
11 University of Washington, Seattle
12 University of Wuppertal
13 Yale University

a Current address: Loma Linda Univ. Medical Center, Loma Linda, California.
b Current address: LeCroy Research Systems, Spring Valley, NY 10977.
c Current address: Physics Dept., FNAL, PO Box 500, Batavia, IL 60510.
d Permanent address: CERN, 23 Geneve 1211, Switzerland.
e Current address: FNAL, CDF, PO Box 500, Batavia, IL 60510.
f Deceased.
g Permanent address: Institute of Nuclear Physics, Cracow, Poland.
h Current address: H.E.P. Div., ANL, Argonne, IL 60439-4843.
i Current address: Northern Illinois University, Dekalb, IL 60115.

inside it, and the old Chicago Cyclotron Magnet, termed CCM, which has seen many incarnations in its long history. It should be noted that the experimental hall had to be built around this latter magnet, because of its sheer size and mass. Many sets of proportional and drift chambers are situated along the

beam direction to give information on forward going particle trajectories. A streamer chamber surrounding the target was used to obtain information on very wide angle tracks. Cerenkov radiation detectors and electromagnetic calorimetry are used in addition to the streamer chamber for particle identification. To separate the scattered muon from the collision products, a 3 x 5 x 7 cubic meter wall of steel is placed after the electromagnetic calorimeter. There are then 3 more walls of concrete that separate a total of four sets of proportional chambers and scintillators that form the muon detection and triggering system. The experimental setup as described gives close to 4π acceptance in the center-of-mass system in the scattering event and is shown in Fig. 8 . Each of the components mentioned will be discussed in the sections below, with emphasis on the electromagnetic calorimeter. For the official publication describing the E665 experimental apparatus see Ref. 18 . (Some figures are taken from that reference.)

2.2 Apparatus

(In the description of the apparatus below, the X axis lies along the beam direction, the positive Y axis points west and the positive Z axis points upward. The U direction is any axis angled between the postive Y and positive Z axes and the V direction is any axis angled between the negative Y and positive Z axes.)
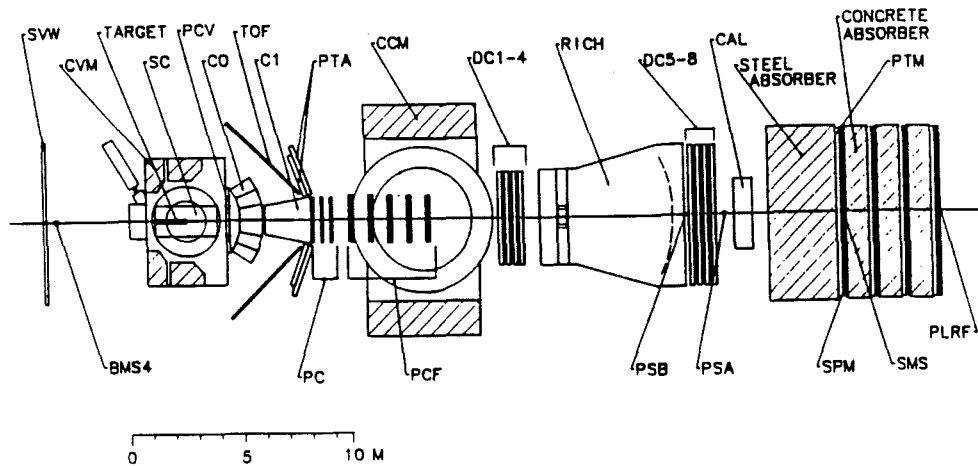
Figure 8. Plan View of Fermilab Experiment E665.

2.2.1 Beam Line

To generate the high-energy, high-intensity muon beam at Fermilab, a fraction of the Tevatron proton beam was steered into the NM beamline at the Fermilab switchyard. For the 1987-88 run, the energy of these protons was approximately 800 GeV and the intensity averaged around 10^{12} protons per 20 second spill. Shortly thereafter these protons encounter about .5 m of Beryllium where high energy nuclear interactions take place producing a flood of π and k mesons. The pions and kaons are then allowed to enter the 1.1 km decay region. This is an evacuated beam pipe surrounded by many sets of focusing-defocusing quadropole magnets. This set of magnets and beam pipe is termed a 'FODO'. The 95% of mesons that don't decay are absorbed by 11 m of Beryllium at the end of the FODO while the muons that have been formed from meson decays pass through this barrier. The resulting muons enter another long FODO re-

gion 420 m in length, 33 m of which also contain 'mupipe'. Mupipe is beam pipe

which has a toroidal magnetic field inside it. This field enhances the proportion

of forward going muons and thus helps get rid of the potentially troubling 'halo'

of wide angle muons that inevitably accompany the highly penetrating beam.

By the time the muon beam enters the experimental hall, only 20-30% of the

muons are in this halo, and of those the majority are very close to the beamline.

Figure 9 shows a schematic of the beamline just described.
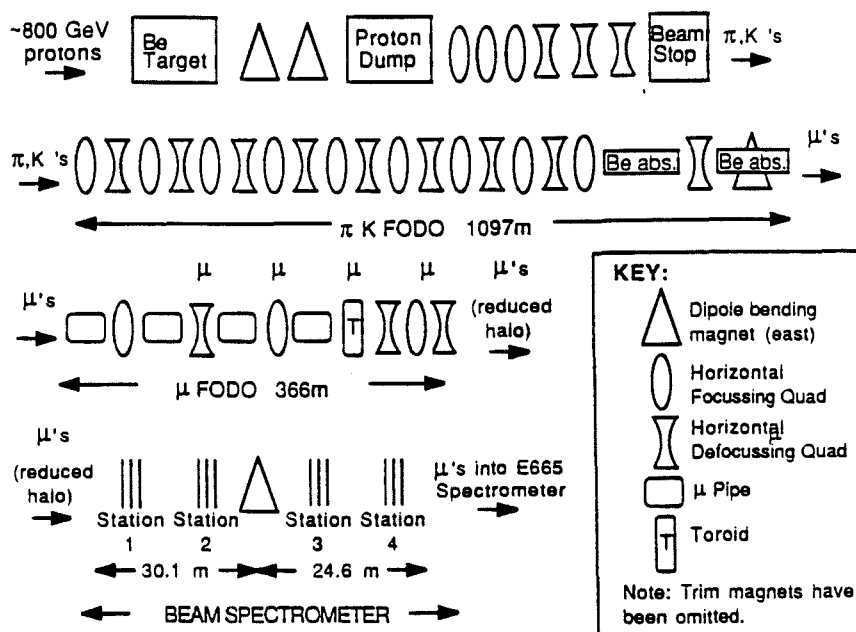
Figure 9. Fermilab Muon Beamline. Detailed description of the NM beamline at Fermilab.

The muon beam during the 1987-88 run averaged 480 GeV in energy with

an approximately 100 GeV momentum spread and had a transverse size of ap-

proximately 5 cm. Hadron contamination was minimal. Figure 10 shows typical

momentum and spatial beam profiles. The maximum beam intensity for the run was 2×10^7 muons per spill. The muons in the beam preserve the RF structure of the main Tevatron ring (53 MHz, or 19 ns in period) and this fact was used for refining the trigger. During the run an electron beam was made for calibration purposes. To accomplish this, the Beryllium primary target was removed and replaced upstream with an alternate one. All charged particles after this new target were swept away, leaving photons and other neutrals. In place of the original primary target, .1 radiation lengths of lead were installed to produce the electrons from photon conversion. Of course, the large Be absorber downstream was rolled away.
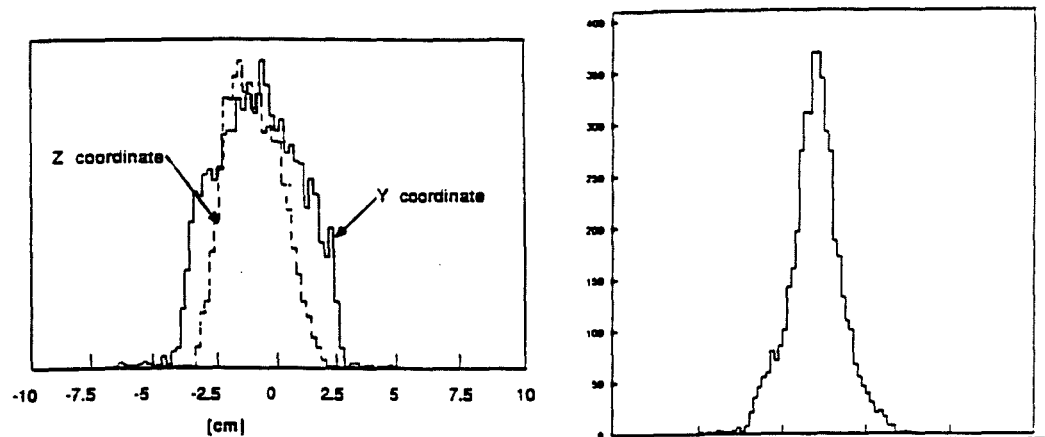
Figure 10. Beam Profile. a) Typical Y and Z beam profiles for LAT data. b) Typical momentum spectrum for LAT data during hydrogen run (GeV).

2.2.2 Beam Spectrometer

The momentum and trajectory of the incoming muons are measured by the Beam Spectrometer which consists of two sets of detector elements on each side of a 3 milliradian final bend. They form a 27 m lever arm on either side for precision angular measurements on the order of 10 microradians or about .5% in momentum. Each station has 6 multi-wire proportional counters with 1 mm wire spacing. Two are oriented in the Y direction and two in the Z direction, with the two offset by one-half of the wire spacing. Two more chambers are oriented in the U and V directions . Also in each station are two sets of scintillating counters, one in the Y and one in the Z orientation. The scintillating planes have 12 or 13 thin strips and allow for fast triggering using the incoming beam.

2.2.3 Halo Vetoing

Directly in front of the fourth and final beam station is a wall of scintillators with a hole in the center, allowing for vetoing of muons in the halo region that would miss the target. The 28 counters cover an area approximately 7 meters by 3 meters. A thin steel wall is used to support these heavy counters and to prevent secondary interactions from triggering the beam stations.

2.2.4 Superconducting Spectrometer Magnets

As was mentioned earlier, there are two very large superconducting dipole magnets used in E665. Their fields were opposite in polarity and adjusted in magnitude such that non-interacting muons of all energies would be focused at

one value of y at the first plane of muon proportional chambers. It can be shown then that the y position of the muon at this focusing plane will be related to the value of θ for a deep inelastic scattering event.

The CERN Vertex Magnet, or CVM, had a field of 1.5 Tesla while the CCM had a field strength of 1.2 Tesla. The region between the pole tips of the CVM contained the streamer chamber and target assembly and this region could be seen from above. Three high speed, precision cameras were mounted on the top of this magnet and took pictures of the streamer chamber events. The CCM contained five triplet sets of proportional chambers to measure the curvature of tracks in this region of magnetic field.

2.2.5 Streamer Chamber and Target

Inside the aperture of the CVM lies the streamer chamber and inside that lies the target. Three different targets were used in the 1987-1988 run; liquid hydrogen, liquid deuterium and pressurized xenon. The vessel holding the xenon was different in design than the former two cryogenic targets but all were necessarily nonmetallic. Each target was one meter long and approximately 10 cm in diameter and lay in the upstream half of the streamer chamber. The streamer chamber had grids above and below the target whose voltage was pulsed to $\pm$ 350 kV in a 10 ns period when triggered. The streamers formed in approximately a microsecond around the tracks of outgoing particles and these streamers were then photographed by the cameras mentioned above. Since the cameras could

not operate as fast as the nominal trigger rate for the run, only a small fraction of events were recorded on film. To enhance the sample of true deep inelastic scattering events a new trigger was formed, based on the multiplicity in the wire chambers directly downstream of the CVM (see the Triggering section).

2.2.6 Vertex Detectors

The vertex region can be considered to be the detectors situated between the two large spectrometer magnets. These include the following:

- PCV chambers. These are a set of 6 proportional chambers situated at the downstream aperture of the CERN vertex magnet. They cover a majority of the area of the aperture.

- Cerenkov detectors. Directly downstream of the PCV chambers lies the segmented Cerenkov light detector termed C0. The six modules lie on a curve to ensure that tracks entering them are parallel to their axis. Downstream of the central portion of this detector is a second Cerenkov light detector, C1, with a single module.

- PC chambers. These are 3 sets of four planes of proportional chambers lying just upstream of the aperture of the CCM. The wires in these chambers lie in the Y, Z, U and V directions.

- Time-of-flight counters. On either side of the Cerenkov detectors lies a plane of 38 vertically oriented long, thin scintillators used to measure the time-of-flight of wide angle particles. The start counter for this system

is downstream of the first beam station. Calibration is done with a laser system split equally to each scintillator.

- PTA chambers. This is a plane of proportional chambers made of aluminum (like the ones described below for Muon Detection) that lies directly behind each TOF plane but at a slightly different angle.

2.2.7 Forward Tracking Chambers

The CCM is the momentum analyzing magnet for forward going particles and therefore contains a large number of tracking chambers to provide good momentum resolution. Located in the gap of the CCM are five sets of three chambers called the PCF chambers. Their wires are oriented in the Z, U and V directions.

Downstream of the CCM are several sets of very large aperture drift chambers. First comes 8 planes of 4 meter wide chambers. After the RICH counter, described next, comes another 8 planes of 6 meter wide chambers. Wires lie in the Z, U and V directions.

2.2.8 RICH

For the data collected in the 1988 portion of this run, an additional particle identifying Ring-Imaging Cerenkov counter was online. This detector consists of a large aluminum box approximately 6 meters long in the beam direction 5 meters wide at its downstream end and about 3 meters high, situated between the two sets of drift chambers. It was filled with 1 atmosphere of Argon gas,

which is about 6–8% of a radiation length. The cone of light produced by high momentum particles is focussed on to a photon conversion plane by a series of spherical mirrors located on the back wall of the RICH. The radius of the ring of light detected at the chamber plane gives a value for the velocity of the particle. Taken in conjunction with the momentum measurement from the spectrometer magnet, this yields a value for the mass of the particle.

2.2.9 Muon Detection

After the calorimeter position, there exists a very massive steel absorber wall, used to selectively filter out all particles except for muons. The absorber is 3 meters thick, 7 meters wide and 5 meters tall. After this steel wall is the first of four sets of muon detectors. It consists of two planes of proportional tube counters, called the PTM's, deadened in the beam region, one large plane of thick scintillators with a hole in the beam region (the SPM counters), and finally a small thin set of scintillators to cover this hole region (the SMS's). The PTM wire chambers are identical in design to the PTA planes noted above and each plane really consists of two planes of wires offset by half of the wire spacing. There is a vertical and horizontal set of these planes in each of the four divisions.

2.2.10 Triggering

For this experiment, a set of seven triggers was developed. All except for HALO used some form of beam defining trigger component. This consisted of a hit from each of the seven scintillator beam stations in coincidence with a

strobe from the phase locked accelerator RF pulse and in anti-coincidence with the Veto Wall. If a muon is in the preceeding or subsequent RF bucket, the beam definition is vetoed. For the SAT, a restricted set of the beam counters was used to define the direction of the beam more precisely. The triggers are as follows:

1. LAT: (Large Angle Trigger) requires an LAT beam in coincidence with 3 out of 4 SPM planes having a hit and in anti-coincidence with the small SMS counters in the first and last planes. This trigger was expected to give large Q^2 triggers (> 3 $(GeV/c)^2$). It comprised approximately 30% of all triggers.

2. SAT: (Small Angle Trigger) requires an SAT beam in anti-coincidence with specific hits in the SMS counters. A hardware look-up table was used to determine where an unscattered SAT beam should hit and, if there were SMS hits at those locations, a veto was declared. This trigger was designed to work down to $Q^2 \approx .5\,(GeV/c)^2$. It comprised approximately 30% of all triggers.

3. RBEAM: (Random LAT Beam Trigger) requires an LAT beam in coincidence with a pre-scaled RF-triggered random number generator. This trigger was used to study reconstruction and normalization efficiencies in the data and comprised approximately 5% of all triggers.

4. RSAT: (Random SAT Beam Trigger) requires an SAT beam in coincidence

with another pre-scaled random number generator, also triggered by the RF. This trigger was also approximately 5% of all triggers.

5. HALO: (Halo Muon Trigger) requires a hit in the veto wall in coincidence with 3 out of 4 SPM planes firing. This trigger was designed to study muon response throughout the detector and comprised approximately 10% of triggers.

6. FCAL: (Calorimeter Energy Trigger) was used to provide a form of triggering independent of the muon walls. This trigger requires an approximately 60 GeV signal in the calorimeter outside a 32 cm. cross centered on the beam. The beam definition was a subset of the LAT beam and the trigger is vetoed if there was another muon in any of the 15 preceeding RF buckets (due to the long memory time of the calorimeter chambers).

7. SC(PC): (PC multiplicity trigger for Streamer Chamber) was the signal used to fire the streamer chamber high voltage and subsequent picture taking. Because of the limited rate of triggering for the streamer chamber, not only did this trigger use prescaled LAT and SAT triggers, but also an additional wire chamber multiplicity trigger. Two hits were required in each of the three Z planes of the PC, excluding a vertical stripe centered on the beam.

Figure 11 shows the 50% and 99% acceptance regions in the $Q^2 - \nu$ plane for the ostensible physics triggers LAT and SAT, determined by Monte Carlo

studies.

2.2.10.1 **Triggering Rates, Efficiencies and Problems**

Table 3 gives a list of the three 'physics' triggers LAT, SAT and SC, with values for the total number of tapes, triggers and expected true deep inelastic triggers for each. As one can see, the efficiencies of our triggers during this run were very low, giving up to 95% false triggers in the LAT case. The main reasons for false triggers in the LAT were muon scattering in the steel absorber (taking the muon out of the veto region), inefficiencies in the veto system and electromagnetic scatters in the target (such as muon bremsstrahlung and muon-electron scattering). The last type of event is allowed in our trigger even though the Q^2 and θ_μ of the scatter are low because the target lies completely inside the CVM spectrometer magnet. Then, for events occuring in the last part of the target, some of the magnetic focusing is lost and the scattered muon is swept into the triggering region. These events can be characterized by their large y value.

Filtering out these false triggers and managing such a resultant large tape volume were problems that our software had to deal with and are discussed below in the Software section.

2.3 Physical Description of the Calorimeter

2.3.1 Introduction

The electromagnetic calorimeter for experiment E665 at Fermilab was built
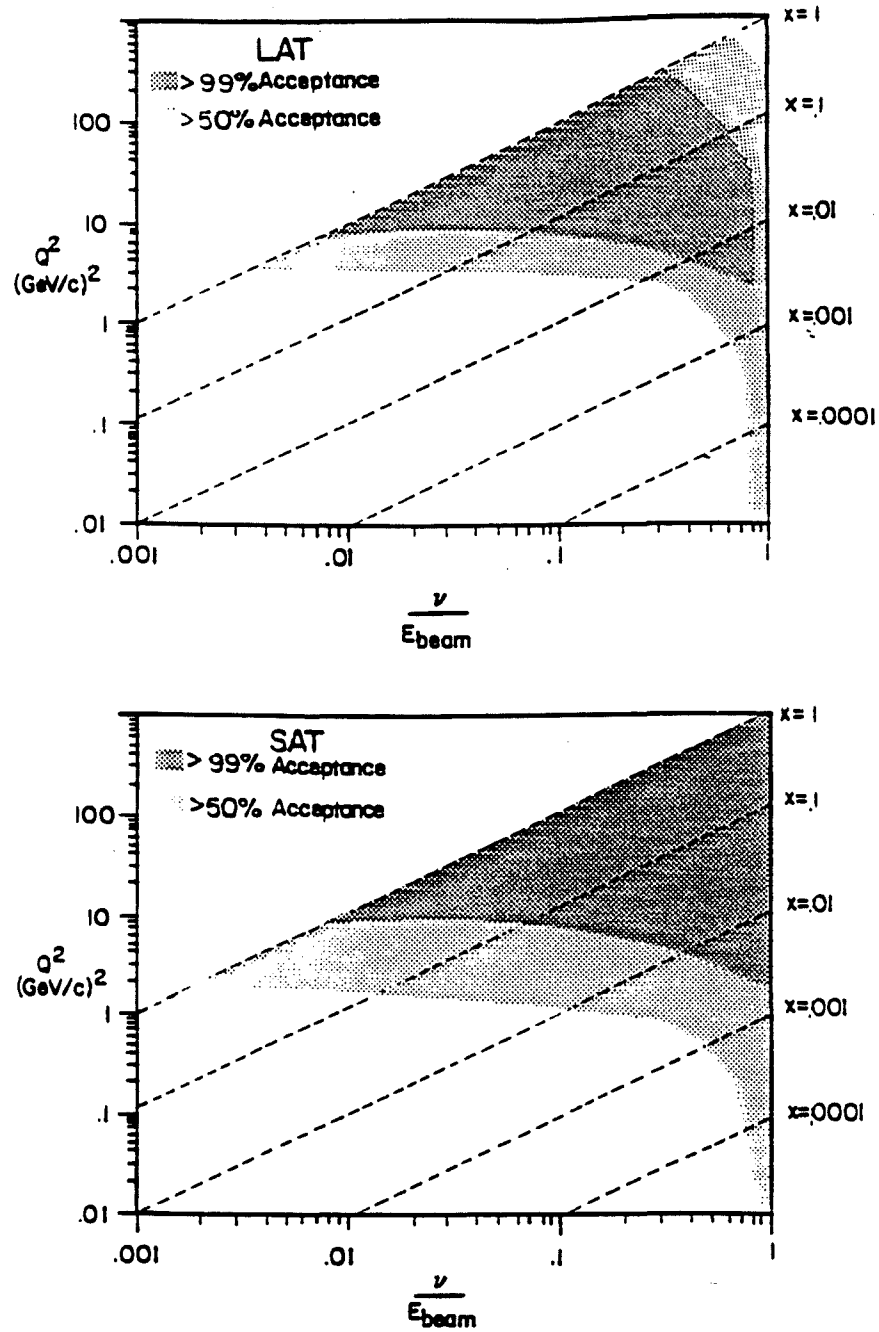
Figure 11. Triggering Acceptance from Monte Carlo. This figure shows acceptance regions for the LAT and SAT triggers. This data was obtained from the Monte Carlo.

Table 3. Data Summary This table gives an approximate accounting
of the number of triggers and tapes associated with each target .

TARGET	NUMBER OF TAPES	TRIGGER	NUMBER OF TRIGS. $(\times 10^3)$	EXPECTED NUM. OF EVTS. $(\times 10^3)$
D_2 500 GeV	1001	LAT	4826	450
		SAT	3282	300
		SC	195	73
H_2 500 GeV	633	LAT	2819	200
		SAT	2390	100
		SC	113	15
Xe 500 GeV	597	LAT	3337	150
		SAT	2653	125
		SC	143	50
D_2 100 GeV	297	LAT	≈ 2600	83
		SAT	≈ 1200	60
		SC	≈ 16	5
Xe 100 GeV	383	LAT	3772	55
		SAT	1613	35
		SC	43	16

by a collaboration of Maryland and Harvard HEP groups. * It was designed

to be a highly-segmented calorimeter with both longitudinal and lateral shower

information and to have a large energy range. Because of its large size, 3 m by 3

m, the cost-effective approach of using Iarocci proportional counters sandwiched

---

* Much of this description can be found in Ref. 19.

between lead sheets was used. To obtain information on the lateral size and position of showers in this calorimeter, the signal from capacitively-coupled pads attached to the proportional tubes was read out. Longitudinal information was obtained by reading out all wires in groups of 16 anode wires in each plane. In addition to this, the four planes about shower maximum (planes 4 through 7) had each wire read out separately. From Monte Carlo studies and prototype tests, an energy resolution of $30\%/E^{\frac{1}{2}}$ was expected, with spatial resolution of 2 mm for isolated showers. Since one of the goals for the electromagnetic calorimeter was that it be able to distinguish single photon showers from high energy pi zero decays, it was designed to separate clusters as little as 5 cm apart. Figure 12 shows a schematic view of the calorimeter.

2.3.2 Calorimetry Theory

Before describing the calorimeter used in this experiment, I think it is useful to briefly discuss the theory of how a calorimeter works. An electromagnetic calorimeter is based on the principle that when a charged particle travels through a high–Z material it radiates bremsstrahlung photons, which subsequently pair-produce an electron and positron. The distance over which an energetic electron loses $\frac{e-1}{e}$ of its energy is termed the 'radiation length' and is described by:

$$X_0 \left[g/cm^2 \right] \simeq 180 \frac{A}{Z^2} \, (for \ Z > 13) = 5.5 \, g/cm^2 \simeq .5 \, cm \ for \ Pb \qquad (30)$$

wires are oriented
in Y and Z in alternate
planes

16cm sq. pads

8cm sq. pads

4cm sq.
pads

Wires are read in
groups of 16 (18
signals/plane)

[There are 20 planes, only
planes 1-10 are shown
for clarity]

The wires are read either
individually or in pairs
in planes 4-7, at shower
maximum (192 signals/plane)

Cathode pads are summed over
all 20 planes in x
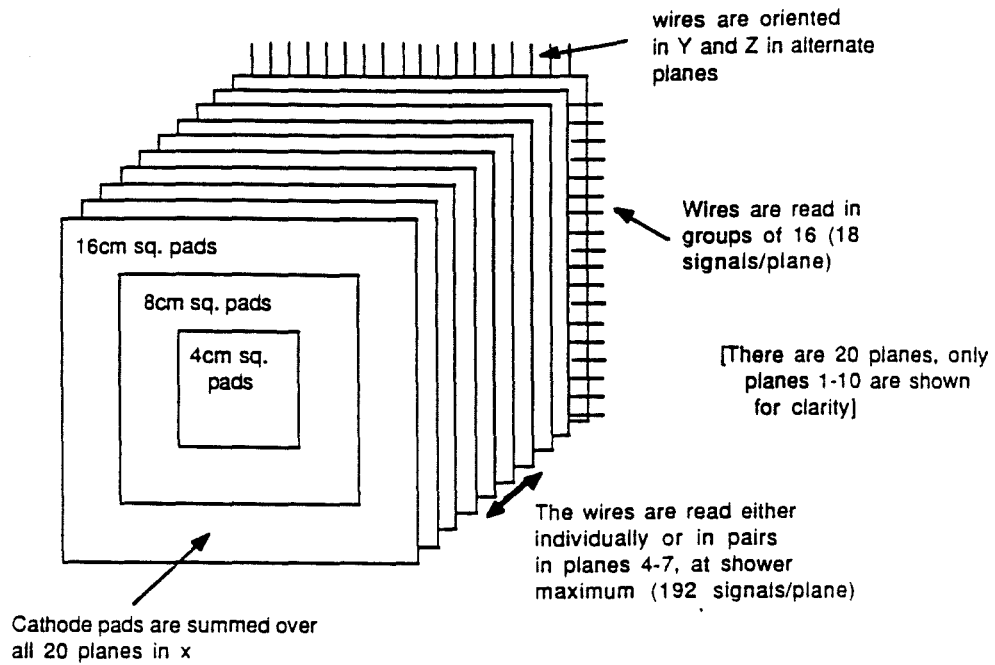
Figure 12.   Schematic View of Calorimeter.

The mean distance that a photon travels before converting to an electron-positron pair is $\frac{9}{7}X_0$ [20] . Both the original parent particle and these 'daughter' particles repeat this process until they lose energy past the point where the dominant energy loss is ionization, not bremsstrahlung. This point is termed the 'critical energy' point and can be calculated approximately as:

$$\varepsilon \simeq 550\,Z^{-1} = 6.7\ (Mev)\ for\ Pb \tag{31}$$

Below the critical energy point, each particle loses energy by ionization in the medium and the generated shower is gradually absorbed. The number of particles as a function of depth in the medium thus increases as a power and then exponentially dies away:

$$N(t) = N_0 t^\alpha e^{-\beta t} \tag{32}$$

and the energy as a function of depth can be parameterized similarly as:

$$\frac{dE}{dt} = E_0 \frac{\beta^{\alpha+1}}{\Gamma(\alpha+1)} t^\alpha e^{-\beta t} \tag{33}$$

where t is the distance along the medium in units of radiation length and E_0 is the incident energy. α and β are parameters that are a function of the medium and logarithmically dependent on E_0. (These parameters were obtained for our calorimeter by using a detailed software simulation of the apparatus which is described in the Software section below. These results were then compared with data.) The Gamma function normalizes the energy deposition properly. The total equivalent number of 'particle crossings' (i.e. total length of gas traversed by all charged particles) produced in the shower has been parametrized using various theories and models as:

$$\int_0^\infty N dl = 5.51 \ E \ \sqrt{Z} \simeq 50 \cdot E \ (equivalent \ crossings) \ for \ Pb \qquad (34)$$

[21] . It should be noted that this is usually a low approximation to the true value due to the increase in the path length from Coulomb multiple scattering.

This showering process occurs very rapidly for an incident high-energy electron or photon. Higher mass particles have a much longer radiation length (Eqn. 30) and therefore infrequently leave a detectable shower in the calorimeter. Thus one way of distinguishing electrons from other charged particles is their showering properties in the calorimeter. (However, nuclear interactions, generating showers of pions and nuclear particles, can occur for incident hadron. These showers can mimic an electromagnetic shower if they start early enough and contain pi zeros.) Photons can be identified by early showering with no reconstructed track pointing to the cluster. The background signal for photons is primarily unreconstructed charged tracks and those neutral hadrons that shower early in the calorimeter.

Figure 13 shows Monte Carlo simulations of electromagnetic showers occuring in our calorimeter. (Results from the calorimeter simulation program will be discussed periodically in the sections below. A discussion of the program itself is contained in the Software section.) As can be seen, if every gas layer

is sensitive to charged particle ionization, then one can build up a reasonably accurate picture of the longitudinal energy flow.

The mean lateral width of the shower is given in terms of the Moliere radius:

$$\rho_M = 21\frac{X_0}{\epsilon} \approx \frac{7A}{Z} = 17.7\,gm/cm^2 = 1.6\,cm\ for\ Pb \tag{35}$$

About 95% of the shower is contained within two Moliere radii [22] . In our calorimeter, as in most lead/proportional-gas calorimeters, the lateral distribution of showers is obtained by attaching capacitively coupled pads to the wire chambers and summing up all layers to form a single 'tower'.

The energy resolution is limited by the statistical nature of the showering process. The limit on energy resolution is given by the fluctuation in the number of particles in the shower:

$$\frac{\sigma(E)}{E} = \frac{1}{\sqrt{N_x}} \approx .032[\frac{\Delta E(Mev)}{E(GeV)}]^{\frac{1}{2}} \tag{36}$$

where N_x is the number of times charged particles cross an active element and ΔE is the energy loss per crossing . This limit is increased when taking into account fluctuations in ΔE ('Landau' fluctuations) and in the amount of active material a charged particle crosses (multiple scattering, large production angles, etc.). For a lead/MWPC detector, the sampling limit for energy resolution of
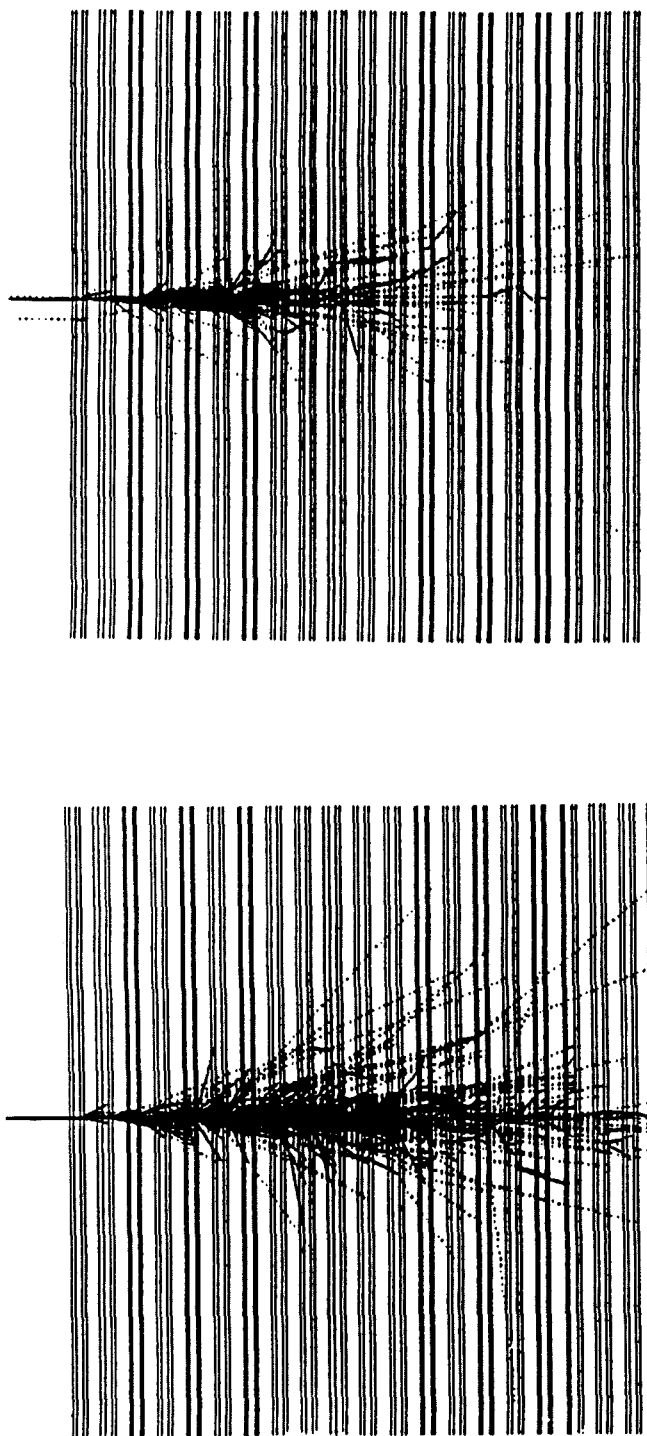
Figure 13. GEANT Simulation of Electron Showers in the Calorimeter. a) Longitudinal shower profile for 5 GeV incident electron. b) 10 GeV incident electron. Solid lines are charged particles and dotted lines are low energy photons. (Not to scale)

a 1 GeV incoming electron obtained from Eqn. 36 is around 7% but a realistic value, allowing for these sources of error, is more on the order of 25%.

2.3.3 Principles of Proportional Tube Counters

Because our apparatus was constructed of proportional counters, as described below, I include a brief section on the theory of how these devices work.

Essentially, a proportional counter is a gas filled small tube with a wire running down the center of it. This wire sits at a high voltage potential difference with respect to the walls around it. It is usually between 5 and 100 microns in diameter. When a charged particle passes through the tube, it ionizes the gas, leaving free electrons and heavy positively charged ions behind it. The electrons drift toward the positive potential anode wire very quickly and accelerate considerably near the high electric fields near the wire. These accelerated electrons can themselves ionize the gas and thus an 'avalanche' of ionization occurs near the wire. The liberated electrons from this avalanche quickly collect on the anode wire, while the positive ions left behind drift slowly toward the cathode walls. This slow positive charge defines the length and shape of the signal. In our case, the signal is on the order of 200-400 ns long. A figurative description of this process is shown in Fig. 14 [23] . The multiplication of the signal due to the avalanche is highly dependent on the voltage and there exists a plateau, the 'Geiger-Muller' point, where the signal is very large and the tube stays active for a very long time. The high voltage region between this point and the pro-

portional mode of operation exhibits a behavior partaking of both modes and is termed the 'limited streamer' mode. It is usually more useful to stay in the proportional mode as we did.
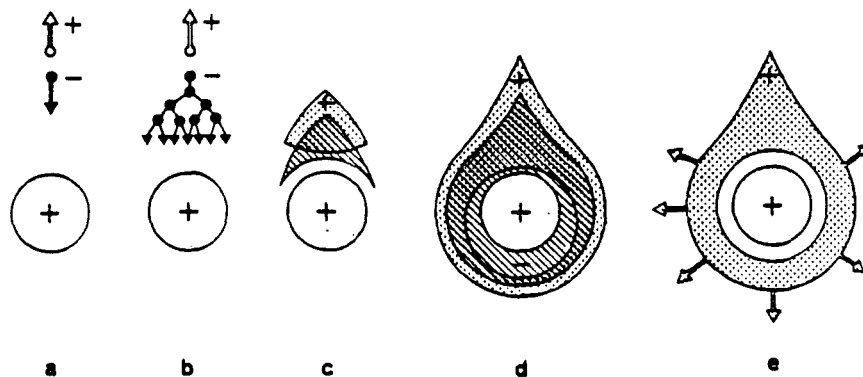
Figure 14. Development of a Proportional Wire Chamber Signal. a) primary ionization b) electron creates avalanche near wire c) electrons from the avalanche separate from the ions d) electrons collect onto the wire e) positive ions drift away from the wire to the walls

2.3.4 Construction

The calorimeter is composed of twenty planes of lead, one radiation length thick each, alternating with twenty planes of aluminum boxes containing the Iarocci proportional tubes (discussed below). The calorimeter begins with a lead sheet. A cross section of one set of these planes is shown in Fig. 15 .

The lead sheet is .56 cm thick and 3 m by 3 m and was built by gluing three identical sheets of lead, 1 m by 3 m, between two sheets of aluminum for support and stability. These aluminum sheets are .0285 radiation lengths in thickness. These lead planes were hung from steel hangers on rails above the calorimeter.
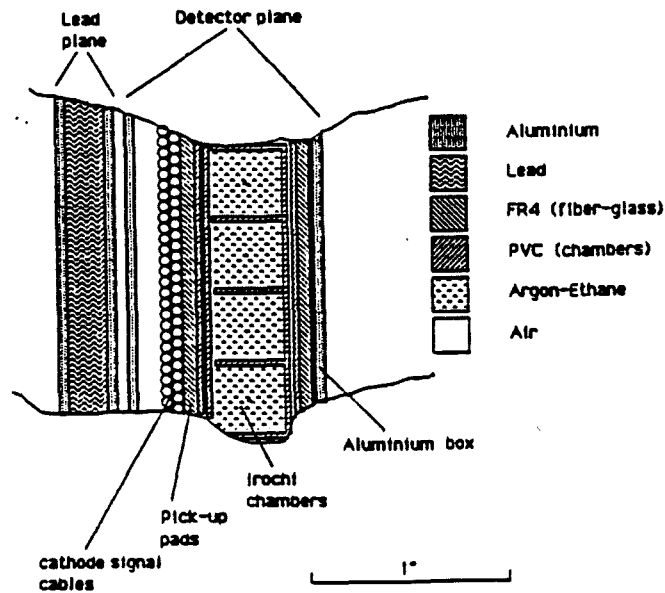
Figure 15. Cross Section of Calorimeter Plane. The lead sheet and set of proportional tubes making up one set of the 20 planes in the electromagnetic calorimeter.

Interspersed between the lead sheets are airtight aluminum boxes 4 m by 3.3 m by 2.5 cm in size. The aluminum faces of these boxes are also .0285 radiation lengths thick. The function of these boxes is to support proportional tubes, to help shield the electronics attached to the tubes and to act as a secondary gas seal should leaks develop. The proportional tubes lie in the direction of the long axis of these boxes and this axis alternates between a horizontal and a vertical orientation. The first proportional tube plane is oriented horizontally. The aluminum boxes are also suspended from rails above the calorimeter. Both the lead and the aluminum boxes are removed from above, while access in situ can be made by moving the planes along the rails in the beam direction.

The 3 m Iarocci tubes are made of plastic and consist of an outer envelope 16 cm wide divided into two equal regions of 8 cm each. Two 3 m extruded plastic inserts, each containing eight 1 cm wide cells and closed off with a plastic cover sheet, are then slid into this envelope (see Fig. 16). This proportional tube unit of 16 cells will be referred to hereafter as a 'bitube', while each of the 8 cm wide inserts will be called a 'profile'. There are 18 bitubes, and thus 288 wires, in each plane, making a 3 m by 3 m active area.
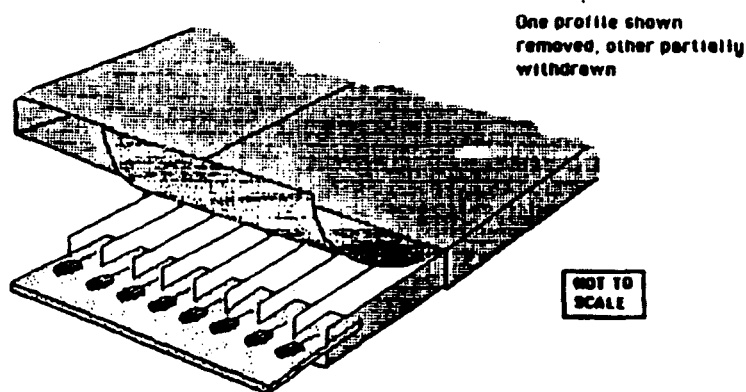
Figure 16.   Iarocci Proportional Tube.   The outer plastic envelope of a 'bitube' and the two 'profiles' that slide into it. This unit has 16 one-cm. cells.

The interior of the profiles is coated with graphite to form a resistive cathode. The anode wires, either 50 microns or 63 microns in diameter, are held in place in the center of each cell by small plastic wire bridges spaced approximately every 50 cm along the bitube. An equal mixture of Argon and Ethane is

circulated down one profile and then up the adjacent one and, thereafter, daisy-chained to the next bitube. The gas comes from a large buffer tank, ten times the volume of the calorimeter, This ensures that the mixing ratio changes no faster than 1% per day. The voltage difference between the wire and the graphite was chosen to be 2.0 kV for the 50 micron wires and 2.15 kV for the 63 micron wires.

Copper-coated FR4 boards with the cathode pad pattern etched on them were placed on both of the outside faces of the bitubes. They were held in place by tape and by wires connecting the pad on one side with the pad on the other. The cathode pads were etched on the side of the board facing the bitube, while the other side of the board is a continuous copper ground plane. Including these two boards, each sensitive plane of the calorimeter is .048 radiation lengths thick. The breakdown of this total is shown in Table 4 . The pattern of pad readout, optimized for pi-zero separation and cost-effectiveness, is to have 4 cm by 4 cm cathode pads in the central 1 m square of the calorimeter. For the 50 cm bordering the outside of this central square, 8 cm by 8 cm pads are used and, finally, on the outside 50 cm border of the calorimeter, 16 cm by 16 cm pads are used.

2.3.5 Dead Regions

The calorimeter is not active across its entire face. There are several 'dead' areas in the calorimeter.

Table 4. Cross Section of each Calorimeter Wire Plane. This table gives the breakdown of the cross sectional widths of the components of each wire plane in the electromagnetic calorimeter.

Thicknesses in one plane	
item	thickness (X_o)
chamber	.0067
aluminum	.0285
FR4	.009
signal wires	.004
Total	.0482

- Geometry of E665: Due to the fact that the CCM magnet has a small dipole separation (1 m), not all trajectories from the target can reach the calorimeter. Projecting a straight line from the downstream edge of the target to the downstream edge of the CCM indicates that the upper and lower 45 cm of the calorimeter can't 'see' the interaction. Effectively these regions are dead, although due to scattering or photon conversion these areas may contain clusters.

- Wire Supports: Since the wires in each bitube are strung along a length of 3 meters and are very fragile, small plastic wire supports were placed every 50 cm along the bitube. It is possible that these wire supports might affect the data if they lined up behind each other in every other plane. It is not known if this is the case or not.

Figure 17 shows an early test made with a radioactive source. Large drops in the counting rate are seen every 50 cm, but this is a highly discriminated signal and the effect on the average pulse height is unknown. No correction is made for this effect.
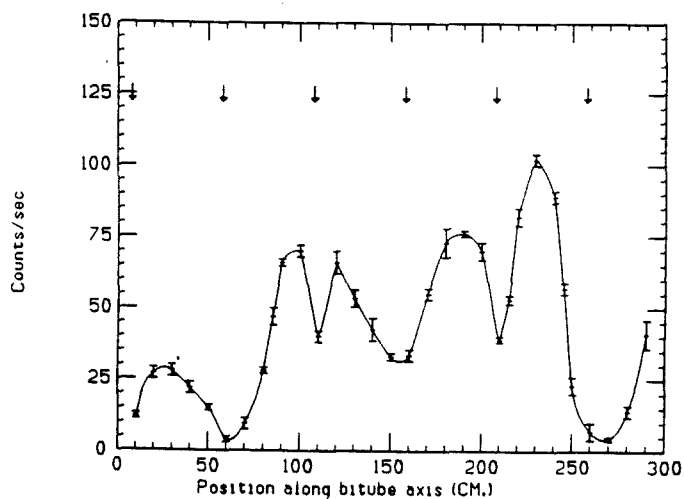
Figure 17. Effect of Wire Supports. The count rate of a radioactive source is shown as a function of position along a bitube. The arrows are spaced every 50 cm.

- Holes between profiles and bitubes: Finally, it is known that all the plastic walls in each bitube in every other plane do line up identically. At the boundary between two bitubes, with both the profile and bitube walls adjoining, there is approximately .25 cm of plastic and this may make for a decreased response like the one mentioned in the last item. All told, these dead spaces account for about 6% of the face of the calorimeter. At this stage of the analysis, however, no correction was made for this effect.

2.3.6 Prototype Tests

Prototype calorimeters were built for testing at BNL and FNAL and one Iarocci chamber was tested for space charge effects at the Harvard University cyclotron. From these tests, it was decided that the proportional mode of the chambers should be used, with 50 micron wires at 2.0 kV with a 50/50 Argon-Ethane gas mixture. From the tests it was determined that these conditions should give a signal size of $Q = 5$ pC per GeV of incoming electromagnetic energy. These tests showed that the calorimeter should be linear up to at least 100 GeV.

The test in the Harvard cyclotron was conducted with a 70 Mev proton beam. The signal at the beginning of the 200 microsecond spill was compared to that at the end. Figure 18 shows how the pulse height varies with incoming flux. The chambers at the center of our 1 MHz beam will therefore show a somewhat lower response.

2.3.7 Data Read-Out

One advantage of the E665 calorimeter in event reconstruction lies in the large amount of data available for each event. The cathode pads described previously are aligned such that 1188 'pad towers' are formed, 20 planes of identically placed pads forming each tower. The signals from the pads are fed through the edges of the aluminum boxes with 100 ohm ribbon cable and actively summed to form the pad tower signals in external electronics cards.
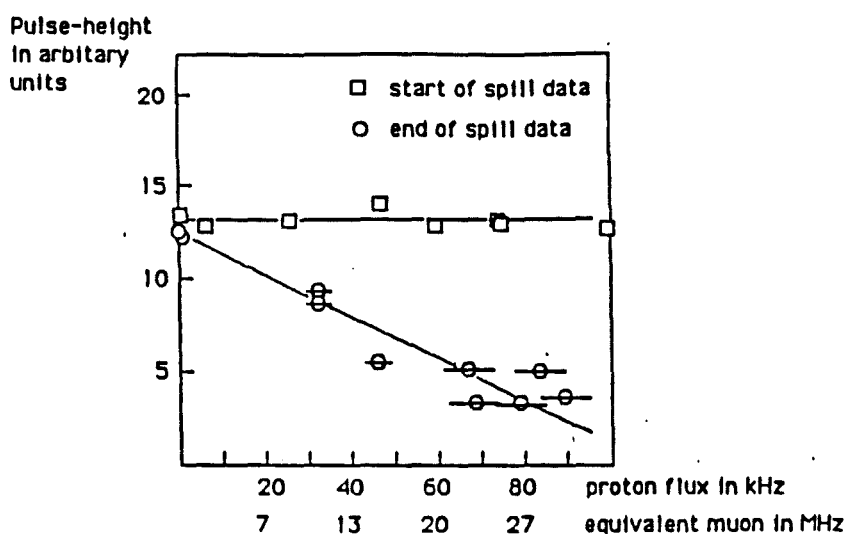
Figure 18. Space Charge Effects on Bitube Signal Size. The difference between the signal at the beginning of a proton spill and the end shows how space charge affects signal readout.

The signals from the anode wires are, in contrast, summed inside the aluminum boxes immediately after leaving the bitube chamber. Each bitube has the signals from its 16 cells summed actively and fed through the edges of the aluminum box with 50 ohm coaxial cable. Thus there are a total of 360 'summed anode' signals. These signals lead into external electronics cards that rearrange their order. In addition, these electronics form the sum of the ten bitubes that have the same position in every other plane (an 'anode tower') and exports that sum to the trigger electronics to form a fast trigger. (See the Triggering section for details on this FCAL trigger.)

The third component of the calorimeter read out is the signal from individual anode wires in planes 4 through 7. Electronics internal to the aluminum boxes read out each wire of each bitube in these planes. These signals are fed

through special connectors in the edge of the aluminum boxes and go by 50 ohm coaxial cable to external electronics boards. Due to monetary considerations, only the central 1 m (or six bitubes) have every wire monitored on these boards. In the outer meter on each side of the center, the signals from adjacent wires are summed.

Besides these data, various calibration data were read out during every interspill period. These included readings of temperature monitors spaced throughout the calorimeter, the voltage from each high voltage supply and CAMAC crate, the temperature, pressure, voltage and spectrum from the gas gain monitors and results from the calibration tasks that monitored the pedestals and gains for each ADC channel. This monitoring hardware is described in the next section.

2.3.8 Data Flow

The event-by-event data from the calorimeter, which includes the signal from the pads, the summed bitubes and the individual wires, all lead into LeCroy FASTBUS 1885 ADC's. These 12 bit ADC's have an automated dual range, such that the gain of the ADC decreases by a factor of 8 once the input signal comes close to saturating the lower range. This change occurs at a different point for each channel, but usually occurs around 3500-3900 ADC channels. Thus, each ADC has an effective range of 32K channels with decreased resolution in the higher range. This dual range means that two sets of pedestals must be

measured-one for each range.

The two crates of FASTBUS ADC's are themselves connected to a third FASTBUS crate that contains four LeCroy 1892 memory modules, each one storing several events worth of calorimeter data. To be consistent with the rest of the experiment, this final FASTBUS crate acts like an independent front-end computer and is read by the MicroVax event processing computer along with the three PDP front-end computers (which reads out data from the rest of the experiment). Data from all four sources is concatenated and written to magnetic tape by this MicroVax.

During the interspill period, the calorimeter calibration and monitoring data is read out by one of the PDP's. It is possible to read out the FASTBUS monitoring data this way because there exists a FASTBUS to CAMAC interface. Figure 19 is a simplified description of the data flow for the electromagnetic calorimeter.

2.3.9 Calorimeter Monitoring

The calorimeter is located in an environment that is not stable with respect to voltage supply, temperature, pressure and gas composition. Because a calorimeter's function is highly dependent on these parameters, it is necessary to continuously monitor them. In E665, this is done by independent software tasks in the PDP front end computer every interspill period. The monitoring hardware for the calorimeter included the following:

Calorimeter
Data Flow

PDP-11

PDP-11

MicroVax

PDP-11

1892
Memory

CAMAC

ADC

Calibration

Pad
Signals

Pad
Signals

Calorimeter Planes

1885
ADC's

1885
ADC's

Pad,Wire
&Bitube
Signals

Pad,Wire
&Bitube
Signals

To PDP-11's

FCAL trigger
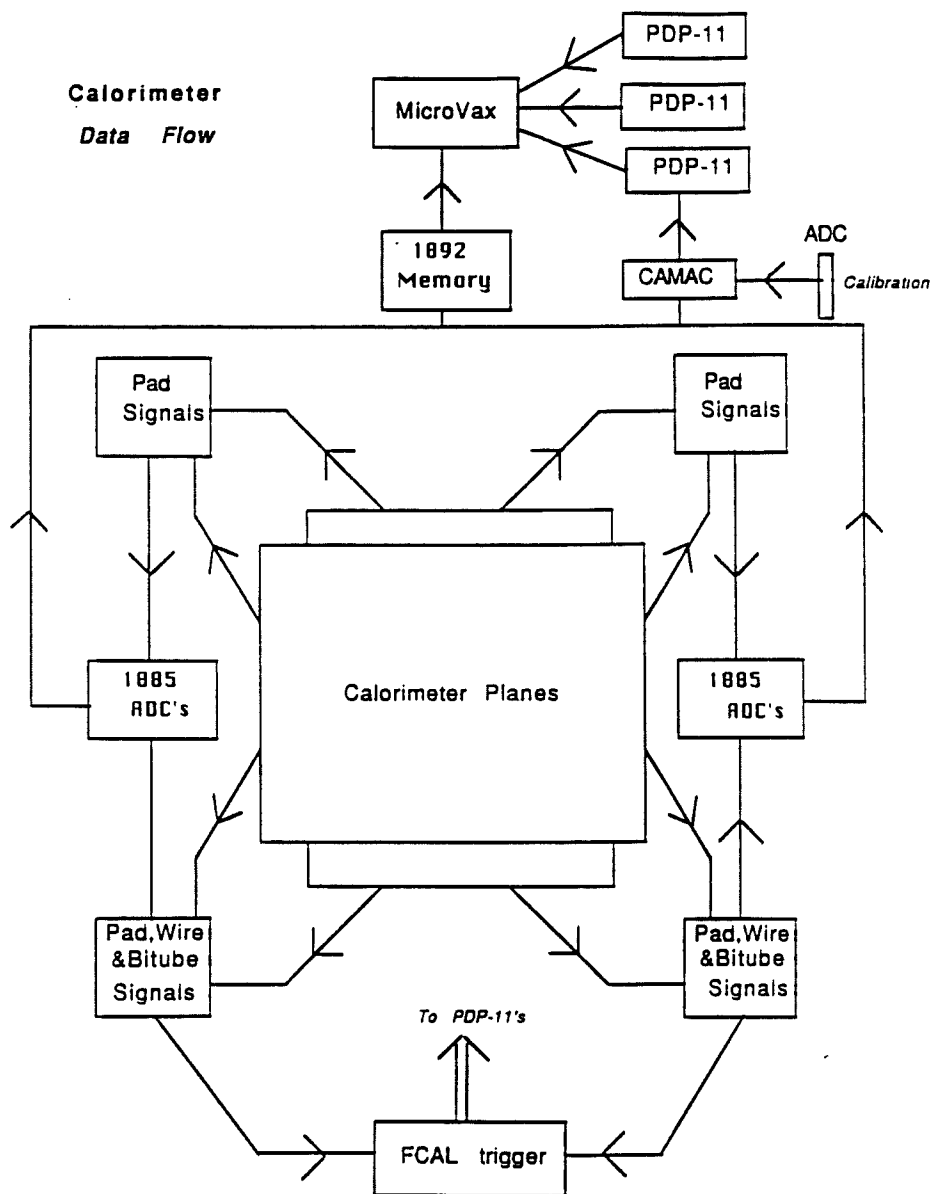
Figure 19. Calorimeter Data Flow.

1. 24 temperature monitors were placed throughout the calorimeter. Two
of the monitors are located in the two gas gain devices and one is lo-
cated externally to the calorimeter to measure the temperature of the air.

CAMAC ADC's read the output voltage levels.

2. These ADC's also monitor the voltage output of the 'Droege' high-voltage supplies as well as the D.C. voltages coming from every CAMAC and FASTBUS crate used.

3. Pressure in the input and output gas lines are measured by two pressure transducers whose output is fed into the same ADC's.

4. Two gas gain devices were constructed. One was placed on the gas input line and the other was placed on the output line. These devices are proportional tubes with 25 micron wires held at high voltage. They have precisely placed Fe-55 sources next to windows in the tubes. The spectrum of pulses from these monitors is measured during the interspill period by a peak sensing LeCroy 2259 ADC. The mean of this spectrum, calculated in a limited area around the peak, was calibrated with respect to temperature, pressure and voltage. After correcting the output from the gas gain monitors for these parameters it was found that the mean was extremely constant throughout the run. This indicates that the gas composition did not change significantly. The spectra of pulses from the gas gain monitors were slow in collecting and the temperature and pressure in the gas gain monitors were not neccesarily indicative of the temperature and pressure in the calorimeter. Because of these problems the gas gain obtained from the monitors do not give as good a profile of the gain changes as the

raw pressure and temperature readings. Because of the constancy of the gas composition, the gas gain could be computed from temperature and pressure readings only.

5. To ensure that the pedestals and gains of the FASTBUS ADC's did not change during the experiment, an interspill task gathered information on these as well. A custom CAMAC controllable pulser was used to inject a series of voltage pulse to the pad tower electronics. To obtain pedestals, the value of this output pulse was set to zero. It was not possible to monitor every pad channel with this method. Instead, 8 or 9 channels were pulsed at one time. For the bitubes and wires, each channel had its own pulse generator on the electronic amplifier boards located within the plane.

2.3.10 Calorimeter Performance

2.3.10.1 Cathode-Anode comparison

During the 1987-88 data taking period the electromagnetic calorimeter was essentially fully working.

Figure 20 shows the ratio between the two independent energy measurements that the calorimeter produces-the energy in the anodes (bitubes) and the energy in the cathodes (pads). The 9% width shown in the data agrees reasonably well with the expectation from electronics limitations, such as pedestal width and noise. This figure also contains the energy dependence of this ratio.

As can be seen, only at energies below 10 GeV, where these limitations are pro-
portionally more important, do the two energy measurements differ significantly.
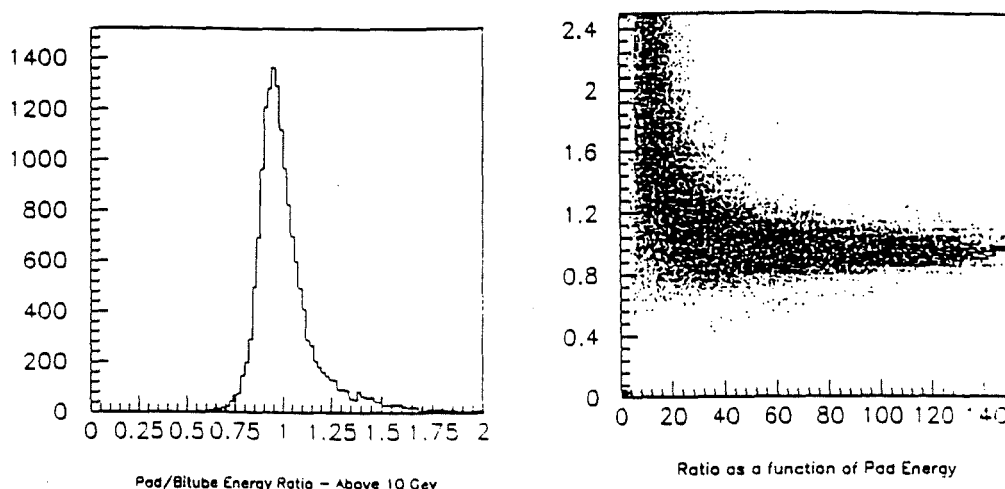
Figure 20. Cathode Energy-Anode Energy Ratio. a) The ratio
between the two energy measurements for energies greater than 10
GeV. b) The energy dependence of this ratio.

2.3.10.2 Dead channels

For the entire data taking period there were several completely dead chan-
nels, amounting to about 1-2% of the possible data channels. These deaths were
due to conduction problems in the bitubes (necessitating turning off the high
voltage to that profile) and broken electronic connections. Figure 21 shows the
location of these dead channels. It was possible to correct for these channels
and this is discussed in the Data Analysis section below.

Besides the dead channels shown in Fig. 21, it soon became obvious that
there were problems with gas flow in other bitubes, mainly in plane 4. Because

CALORIMETER DEAD SPOTS

- DEAD PROFILE
- DEAD BITUBE (ELECTRONICS)
- DEAD PAD (ELECTRONICS)
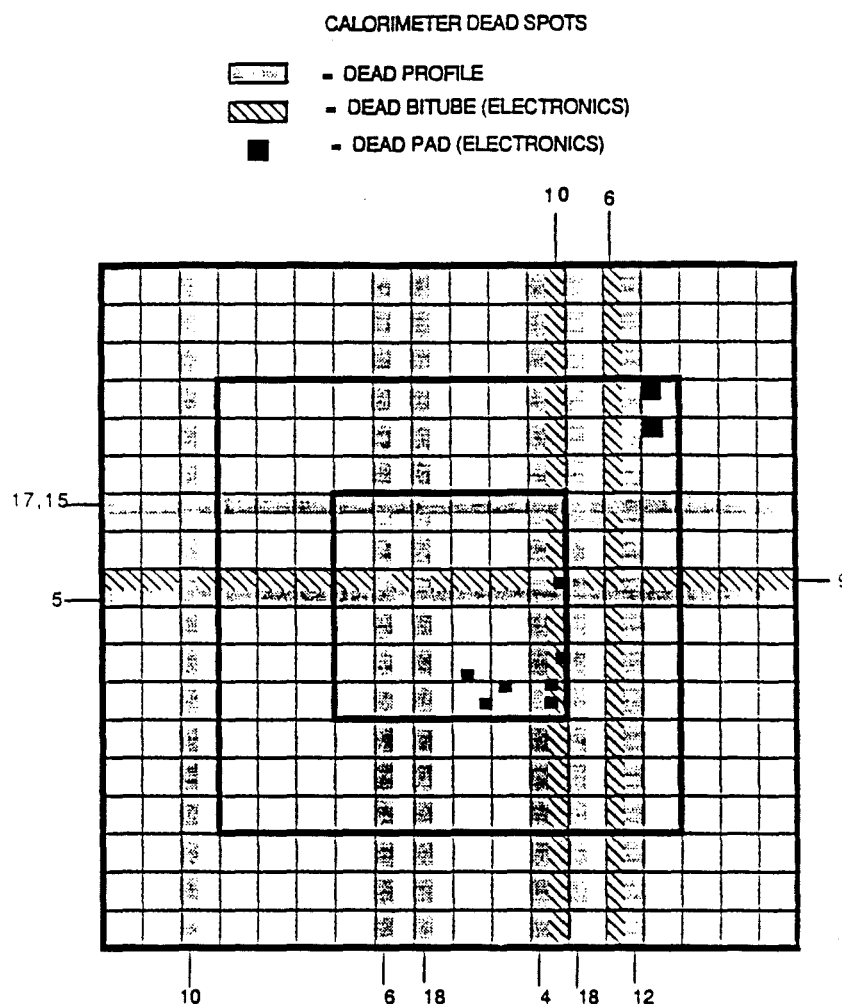
Figure 21. Calorimeter Dead Channels. This plot shows the location of non-active channels in the calorimeter. The numbers on the sides of the figure refer to the plane in which the dead bitube or profile is located in.

those planes contain much of the developing part of a shower, these effectively dead bitubes decreased the response of the calorimeter greatly and produced nonuniformity across the face of the calorimeter. In the Software section below, I discuss how these dead bitubes were accounted for.

2.3.10.3 Monitoring performance

• Stability of pedestals and slopes. The change in the low range pedestals over a two month period is shown in Figure 22 . As can be seen, on the average the pedestals did not change more than 10 channels.
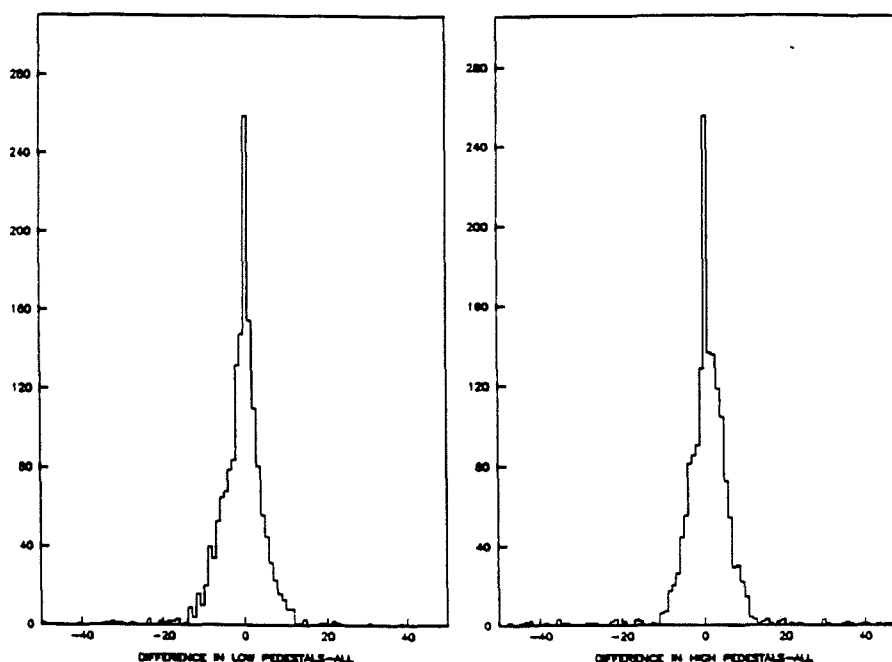
Figure 22. Change in Pedestal Values. The difference in Fast-bus ADC pedestal values between September and November of 1987 is shown. a) is for the low range pedestals and b) is for the high range.

• Stability of voltages. The high voltages on the wires were extremely constant throughout the run and varied by less than 2 volts.

• Stability of gas gain. Figure 23 shows the variation in calculated gas gain during the hydrogen run. The values for the calibration parameters used were
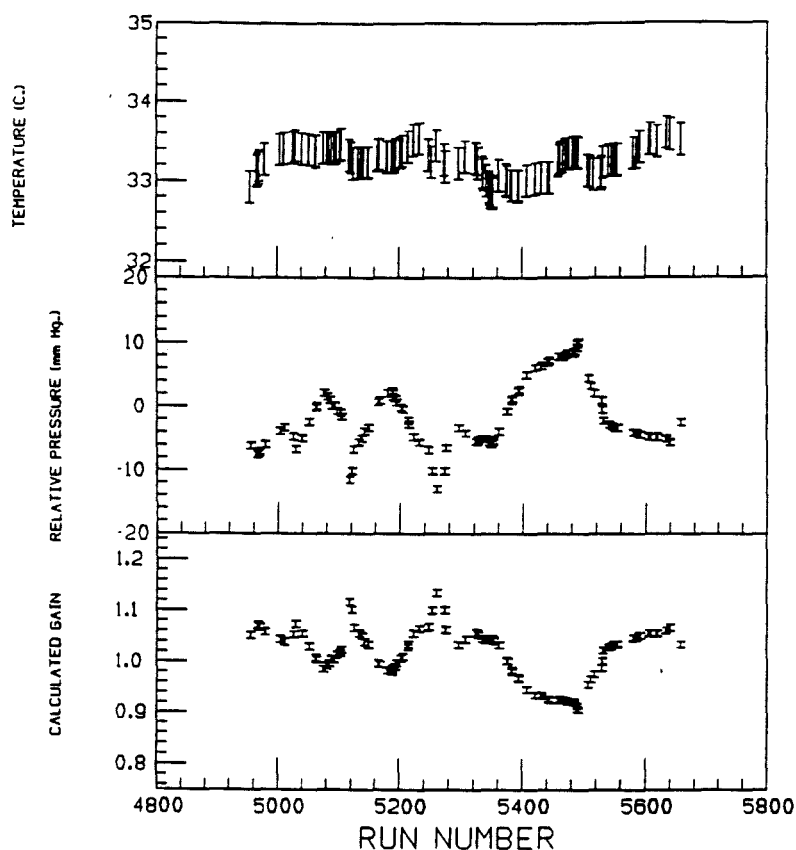
Figure 23.   Temperature, Pressure and Gas Gain for the Hydrogen Data.   a) Temperature as a function of run number b) Pressure as a function of run number and c) Gas gain computed from these two values.

$$\frac{dG}{dT} = .029\,(deg.\,C.)^{-1} \tag{37}$$

and

$$\frac{dG}{dP} = -.0098\,(mbar)^{-1} \tag{38}$$

These parameters were obtained by comparing the mean of the gas gain

monitor output to fluctuations in temperature or pressure and making a simultaneous fit to the functional form:

$$Gain = (1 + \frac{dG}{dP}(P - P_0)) \cdot (1 + \frac{dG}{dT}(T - T_0)) \qquad (39)$$

where $P_0 = 1000\, mbar$ and $T_0 = 32.3\, deg.\, C..$

The mean of the gas gain spectrum for a sample time period, after correcting for the pressure and temperature readings in the fashion above, is shown in Fig. 24
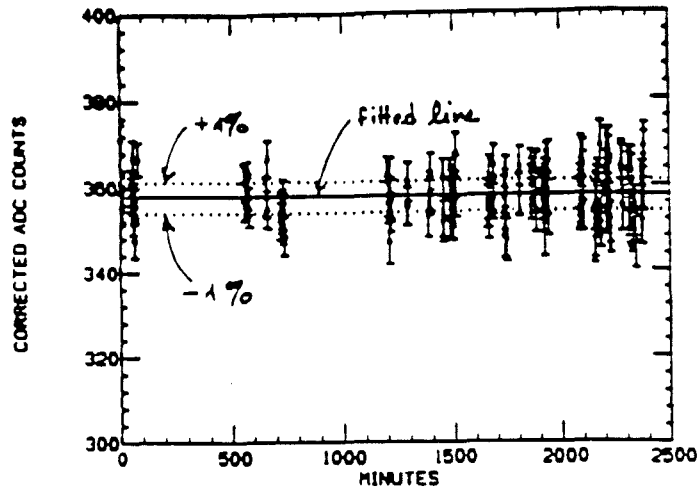
Figure 24. Corrected Mean of the Gas Gain Spectrum. This figure shows the mean of the gas gain monitor spectrum, after correcting for temperature and pressure, for a sample period.

2.3.11 Calorimeter Calibration

Since the calorimeter's purpose is to measure an absolute value of energy,

it is critical to have knowledge of the absolute scale of the device. The other purpose of calibration is to have a good estimate of the uncertainty in the energy measurement. This 'energy resolution' is not constant, but instead varies inversely as the square root of the energy, as explained in the Calorimetry Theory section above. Calibration has been done in several ways and cross-checked against each other. Each of the sub-sections below describes a different calibration. The determination of the behavior of the energy resolution was accomplished with electron beam data and bremsstrahlung data from the 100 GeV SAT Xenon target data.

2.3.11.1 **Electron calibration**

As was mentioned in the Apparatus section, for a short period of time the beamline was converted into one that delivered electrons to the experimental hall. The energy of the electrons nominally varied from 5 to 150 GeV. However, as we shall see, due to pion contamination of the calibration beam at high energies, much of this data was unusable. Another major limitation of the data sample is that it covers only the central 1 m. vertical section of the calorimeter because of shadowing of the electron beam by the veto wall. The data sample was reduced to events having a reconstructable forward track pointing to a single major cluster in the calorimeter. The energy of the pad cluster plotted against the reconstructed track momentum is shown in Fig. 25 . Because there was a very large hadron contamination in the beam, the result is not a thin line

but a wedge, showing the random start of showering in the calorimeter of the

penetrating hadrons. This is especially true for tracks above 40 GeV in energy.

To separate out the electrons and thus determine the linearity and resolution of

our calorimeter a final cut is made on the data sample based on the longitudinal

shape of the shower. The following set of cuts were applied:

Cluster Energy vs Track Energy (Gev)
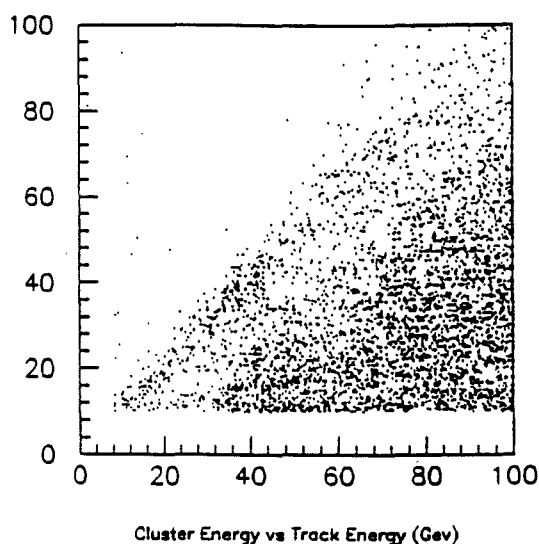
Figure 25. Calorimeter Response vs. Electron Energy for Calibration
Data. This figure shows a portion of the data.

1. Longitudinal center of gravity of shower < .4 meters

2. Starting point of shower (where 10% of shower has occured) < plane 5

3. (Energy in back 10 planes)/(Energy in front 10 planes) < 1.0

These cuts bias the data to showers that start early in the calorimeter, or show-

ers that are electromagnetic in character. After these cuts were applied there

remained approximately 5250 electron calibration events.

- Linearity:

Figure 26 shows the average calorimeter energy vs the incoming energy. The slope of the line is slightly lower than 1.0 because of the residual hadron contamination of the beam. (Note: in this plot, as in all plots in this section, the data has been corrected for dead channels, bitubes with deadened response from gas flow problems, and corrected for gas gain. The comparisons of the calorimeter responses before and after these corrections are shown in the Calorimeter Data Analysis section below.) As one can see, the calorimeter is highly linear across the range of energies shown. The ratio between ADC channels and incident energy obtained from this calibration, after correcting for gas gain, is

```
 90
 80
 70
 60
 50
 40
 30
 20
 10
  0
    0   20   40   60   80  100

      CALORIMETER RESPONSE - ALL
```
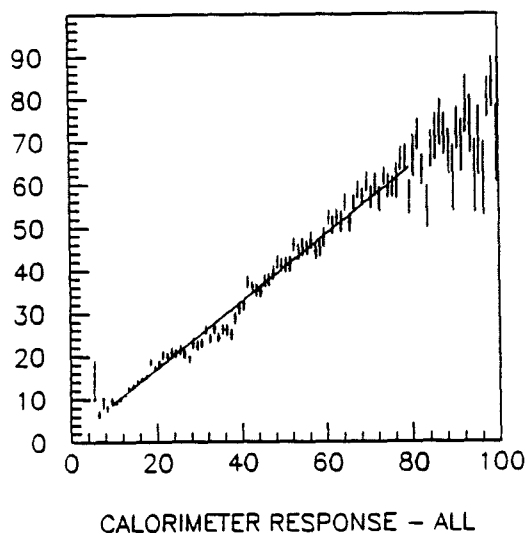
Figure 26. Linearity of Calorimeter Response. Average response of calorimeter vs. incoming electron energy obtained from track fitting.

$$Pad\,Tower\,Electronics\,Gain\ = 132\ ADC\ counts/GeV \tag{40}$$

$$Bitube\,Electronics\,Gain\ = 407\ ADC\ counts/GeV \tag{41}$$

The pad and bitube channel energy thresholds used during the calibration are the same as those used for data analysis and are discussed below in the Calorimeter Data Analysis section.

- Energy Resolution:

Figure 27 shows the energy resolution of the calorimeter response as a function of the inverse square root of the energy. It is plotted in this fashion because the sampling error in a shower calorimeter goes as $\frac{1}{\sqrt{N_x}}$ and this is proportional to $\frac{1}{\sqrt{E}}$ (see Eqn. 36). The plotted points were obtained by binning the electron data in 5 GeV bins and the bremsstrahlung data in 10 GeV bins. The cluster energy for each event was divided by the track energy (whose value is assumed here to have little error in comparison to the calorimeter energy). A histogram was made of this sample and fitted with a Gaussian form. The fitted Gaussian width divided by the fitted mean is then plotted versus the inverse square root of the center of the energy bin. The final result for the energy resolution of the electromagnetic calorimeter obtained from this plot is:
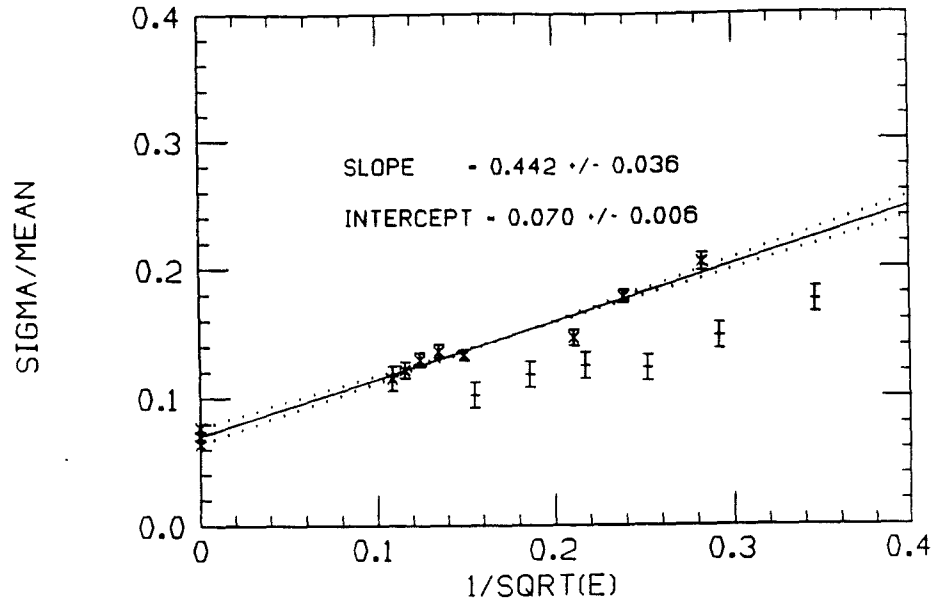
Figure 27.   Calorimeter Resolution as a Function of Energy.   "x" -
Values obtained from electron calibration data. "+" - Values obtained
from GEANT data. Slope and intercept are from linear least squares
fit to data.

$$\frac{\sigma}{Mean} = \frac{.44}{\sqrt{E_{inc}}} + .07 \tag{42}$$

Also shown in the figure are Monte Carlo results from a similar analysis of

approximately 3000 clusters, showing that there is an extra source of error in our

physical device that is not included in the Monte Carlo simulation amounting to

approximately a constant 5%. The source of this error could be the dead spaces

mentioned above and gas flow problems not accounted for. Other sources can

include temperature and pressure fluctuations throughout the device or small

high voltage fluctuations. Using the resolution results in Eqn. 42, one can make

a plot giving the error in energy measurement as a function of incoming energy.

This is shown in Fig. 28 . Note that for low energies (< 4 GeV) the precision

in measurement is very poor, worse than 25%. This is one reason for making a

minimum energy cut for clusters at this point.
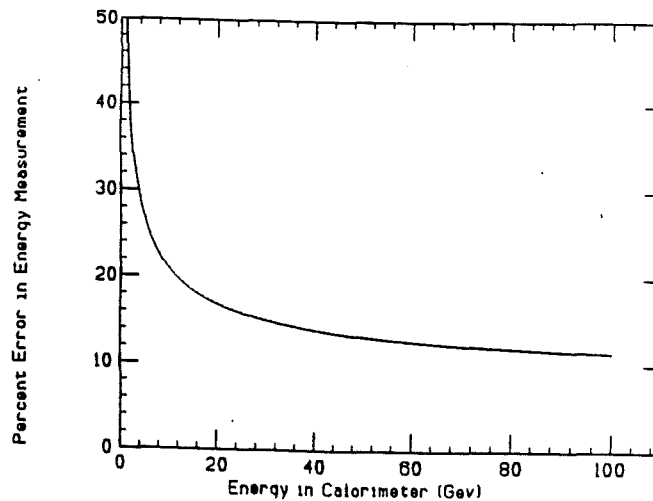
Figure 28. Error in Calorimeter Energy Measurement as a Function
of Energy.

● **Position Resolution:**

The electron data is also crucial in determining the alignment and position

resolution of clustering in the calorimeter. Figure 29 shows the residuals of the

cluster position obtained from pad clustering vs the fitted track position at the

calorimeter. The mean of these distributions give:
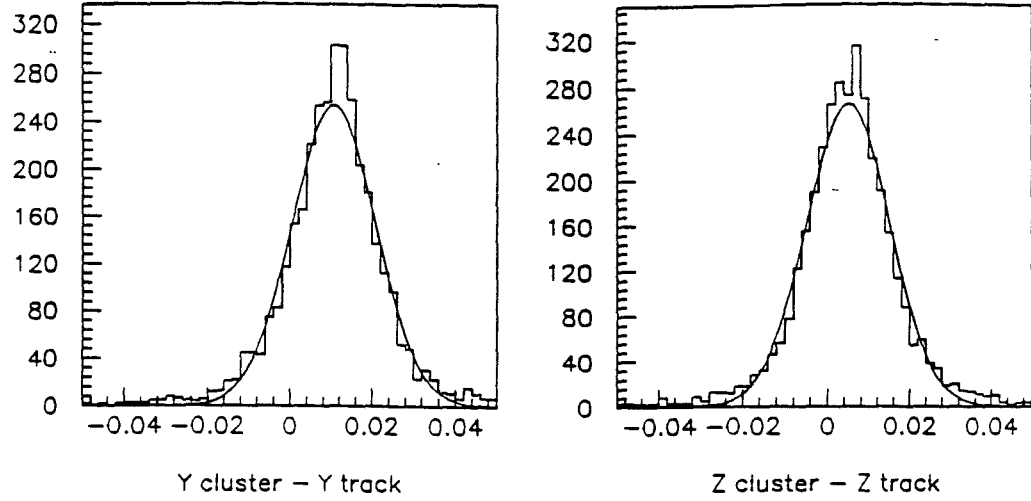
Figure 29. Calorimeter Position Resolution. a) Residual between calculated cluster Y position and track position (cm). Cluster energy is greater than 10 GeV and calorimeter response>.8 b) Residual for Z position of cluster.

$$Calorimeter\ Y\ Offset\ =\ 1.06\,cm. \tag{43}$$

$$Calorimeter\ Z\ Offset\ =\ 0.52\,cm. \tag{44}$$

$$Calorimeter\ Position\ Resolution\ =\ 1.03\,cm. \tag{45}$$

This offset from zero arises from the initial uncertainty in placement of the calorimeter with respect to the final beam position.

2.3.11.2 Bremsstrahlung Events

In the 100 GeV SAT event sample for Xenon were many bremsstrahlung events, as was expected for such a high Z target. These events were useful for determining the calibration and resolution of the calorimeter at high energies. (For the 500 GeV muon data, bremsstrahlung events had on the order of 200-400 GeV photons, which are too energetic for calibration purposes. The calorimeter pads saturate around 32K ADC counts, or about 300 GeV, and large non-linear saturation effects were expected to occur earlier due to effects such as non-containment of the shower within the calorimeter.) The calorimeter response for these events is included in Fig. 26 and Fig. 27 and these events were used in determining the calibration given in Eqn. 40 and Eqn. 41 and the resolution quoted in Eqn. 42. All of the data above 40 GeV is this Bremsstrahlung sample, accounting for approximately 1250 calibration events.

2.3.11.3 Muon minimum ionization

It was believed during the construction phase that the calorimeter would be able to detect the signal from a minimum ionizing, non showering particle as it passed through a pad tower. In fact, it turns out that this signal lies barely above the pedestal position in all the pad towers where there is enough statistical sampling to see it.

Figure 30 shows this signal along with a comparison to the simulation made by GEANT. This simulation was made with a Landau distribution of ionization

for each step, and then the total energy was converted to an ADC count with the gain factor obtained from the simulation of electron showers in the model calorimeter. Then this count was randomly smeared by 10 channels, corresponding to the width of the pad tower pedestals. As can be seen, the two distributions are virtually identical, except for the long tail of higher energy deposition in the data. This is probably due to the contribution of knock-on electrons and delta-ray production in the data that is not taken into account by the simulation.
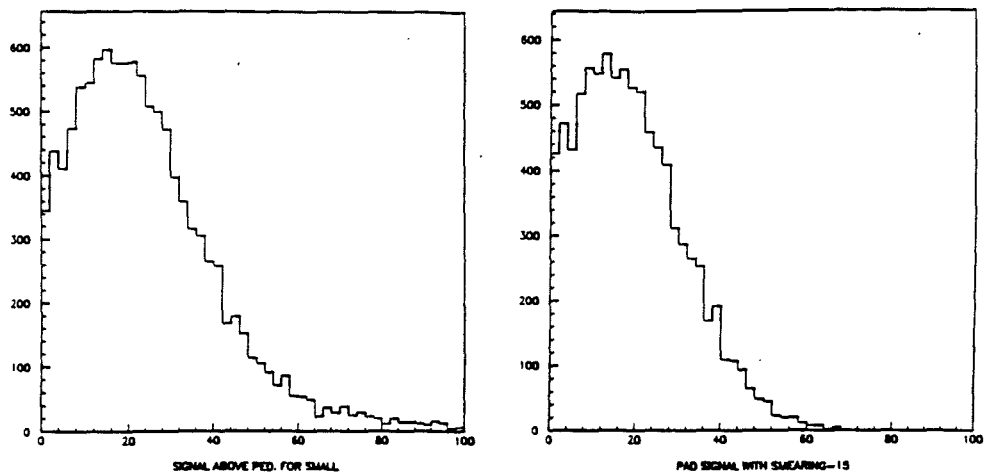
Figure 30. Muon Signal in Pad Towers. a) Number of ADC channels above mean pedestal position when a halo muon passes through the small pad towers. (11000 events) b) GEANT simulation of halo muon signal in pad towers with 15 channel Gaussian smearing. (11000 events)

The average of the halo muon signal in the small pads was used to check

the absolute calibration of the gas gain monitor. As was shown in Fig. 23, the

gas gain varies as a function of the temperature and pressure. To check the scale

of the resulting gas gain changes, a comparison was made to the average halo

muon signal for several sets of approximately 5000 track-fitted HALO triggers.

As shown in Fig. 31 , the signal tracks very well with the calculated gas gain .
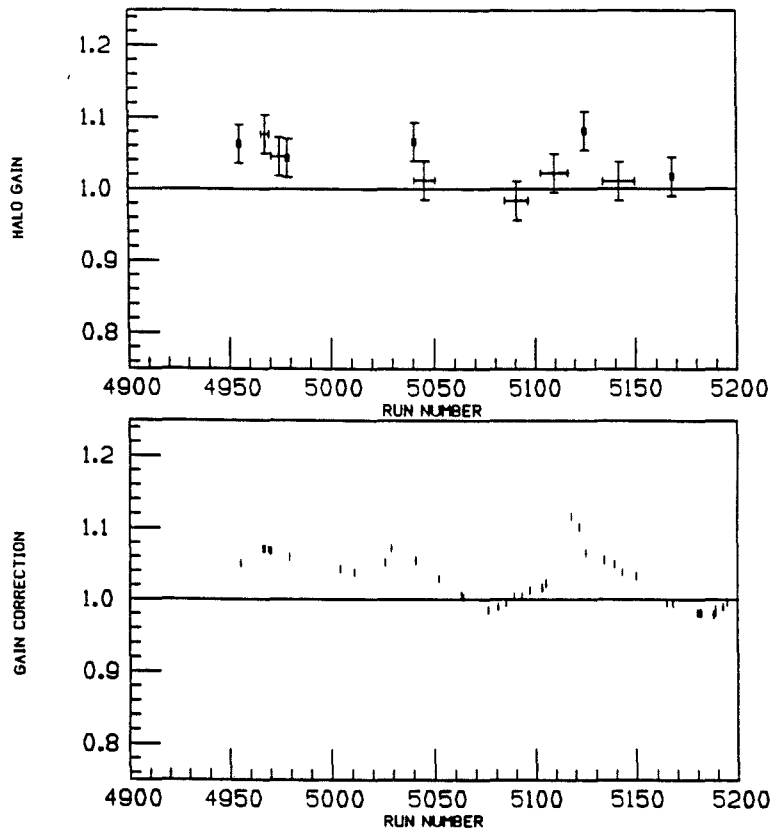
Figure 31. Halo Muon Gain vs Gas Gain Monitor. a) The average of
the halo signal in all small pads as a function of run number. b) Gas
gain calculated using pressure and temperature and parameters given
in Monitoring Performance section.

2.3.11.4 Pi zero measurements

One final check on the response of the calorimeter, and one obviously necessary for this thesis, is to see if the data shows a pi zero signal, given the electronics gain in Eqn. 40 and Eqn. 41. As will be shown below in the Results section, the invariant mass spectrum for pairs of neutral clusters shows a distinct peak at the pi zero mass, 135 Mev. The width of the peak, after subtracting a background spectrum, is consistent with the resolution given in Eqn. 42.

3. The Software Chain

The software used in this experiment was, of necessity, contributed to by a host of hard-working individuals. The main components of the software analysis chain are the Monte Carlo simulation of scattering events in our detector and then the track-finding and particle identification used on both this simulated data and the experimental results. Comparison of results from the experimental data to the simulated data will tell us if the model we use for sub-nuclear reactions is realistic or not.

Figure 32 shows how the data is analyzed. The shaded area in this figure indicates where the analysis of the streamer chamber photographs is done. No streamer chamber information was used for the analysis in this thesis. The same chain is essentially used on Monte Carlo data.

In the following sections I will describe somewhat briefly the main software packages and, instead, concentrate on those sections relevant to the detection and simulation of pi zero and photon interactions in the calorimeter.

3.1 The Monte Carlo

3.1.1 The Lund Model for Event Generation

The Lund model for nucleon fragmentation has been developed over the course of a decade. [24-26] It has been applied to electron-positron annihilation experiments as well as leptoproduction and has passed many detailed experimental tests.

E665 Data Analysis Flow
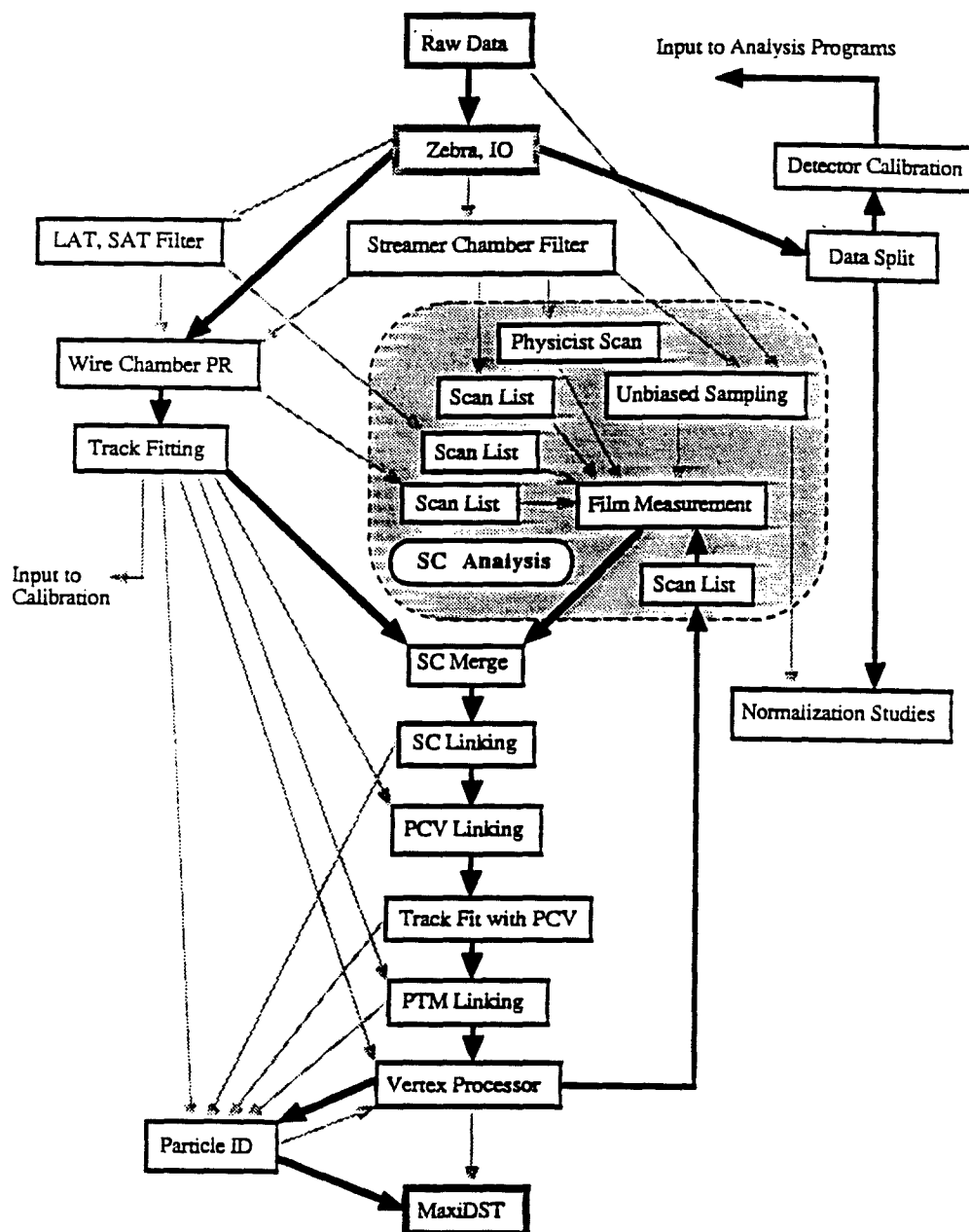
Figure 32.   Flowchart for the Data Analysis.

The fragmentation process in the Lund model contains three parts:

1. The hard primary interaction, whose details depend on the initial process (e^+e^- interactions vs lepto- or photoproduction, for example).

2. The separation of partons and emission of soft gluons and the application of the confinement forces.

3. The decay of the primary hadrons generated

The first step is described by QED processes and scattering theory as outlined in the Theory section. The details of the last step are dictated by experimental values for lifetimes and branching ratios. It is the second step where the Lund model attempts to mimic all that is known about QCD and nucleon fragmentation.

The model assumes a potential between separating quarks that rises linearly with separation and with the 'string tension' or color field energy density between them of $\kappa = 1 \ GeV/fm$. It then assumes that the string breaks into parts, proceeding along its length in the frame of reference where one endpoint is at rest. Each meson formed by the breaking of the color field will take a random fraction of the remaining available energy.

The Lund model, which evolved gradually from the simpler Field-Feynman explanation of fragmentation [27] , describes this process with many parameters. Some of these parameters and their default values are given in Table 5 [26]. Besides these, there are some 30 to 40 others used to limit certain types of fragmentation,

artificially suppress certain channels and make cuts on kinematical variables. (Many are superfluous and have zero default values.)

Table 5. Lund Parameters. A few default values for standard Lund parameters.

Some Lund parameters		
PARAMETER	DEFAULT VALUE	EXPLANATION
$\frac{P(qq)}{P(q)}$	.075	prob. of diquark vs. quark production
$\frac{P(s)}{P(u)}$	.3	prob. of strange vs up quark production
P(spin 1 meson)	.5	probability spin 1 meson is produced
σ_{pt}	.44 (GeV/c)	width of intrinsic p_t distribution

The output from a call to the Lund model is a set of particles resulting from the model interaction: hadrons, the virtual photon, jets, and the scattered muon.

3.1.2 Tracking simulation - 1st Stage M.C.

After generation of the event and its fragmentation according to the Lund model, these particles are then tracked through our experimental apparatus by the E665 stage 1 Monte Carlo program, or 'MC1'. The measured values for the magnetic fields are used to determine particle trajectories. The position and momenta of all charged particles are recorded only at certain planes of the simulated detector. These 'key' planes usually correspond to the front face of a physical detector. The information of particle trajectories at these key planes is

then stored onto a file which is used as input for the next stage.

3.1.3 Detector simulation - 2nd Stage M.C.

An important detail to include in Monte Carlo simulations is the efficiency of how each physical detector responds to a given particle with a given momentum and track location (namely the output from the MC1 program). This is taken care of during the second stage program, termed 'MC2'. Using results from studies of the data, a wire-by-wire efficiency data base was obtained. These efficiency numbers determine what fraction of the time a wire detector will respond with a signal for an incoming charged particle at a given Y-Z spatial location. MC2 then uses this information to simulate the response of wire chambers. The simulation of non-wire chambers, such as the Cerenkov detectors or the calorimeter, is done on an individual detector basis. For the Monte Carlo results given in this thesis, no Cerenkov detector simulation was made, and the simulation of showering in the calorimeter was accomplishedby using the simulation program called GEANT.

3.1.4 GEANT Calorimeter Simulation

The main problem in the study of calorimeter response, given an incoming particle at some known energy, is not predicting how the calorimeter will do on the average. This is usually determined very well by the theory given in the previous chapter. Instead, the real difficulty lies in predicting how widely the calorimeter response can fluctuate from this average. Usually small details of

the calorimeter construction will have a big effect on how large these fluctuations can be. Therefore, it is very useful to develop a reasonably sophisticated Monte Carlo mockup of the specific device you are using. GEANT is a software package produced at CERN, the European based accelerator laboratory, to provide an easy way to setup simulation of a high-energy physics apparatus. (The GEANT code is too complex to be detailed here. See Ref. 28 for further information.)

I wrote a large package of routines to simulate all of E665 using GEANT. The calorimeter simulation was simply 20 planes of lead interspersed with 20 planes of an Argon/Ethane gas mixture. No attempt was made to simulate the details of the Iarocci chamber walls because of the large amount of computer CPU time needed to tranport the generated shower particles through multiple volumes.

To simulate the output from the calorimeter, a running total was kept of all ionization occuring in the gas portion of the calorimeter simulation. This data was divided up into physical regions corresponding to the bitubes and to the pad towers. After each event, each channel's total ionization was multiplied by a gain factor to obtain ADC counts. This was determined by using simulated electron showers (much like the physical detector was calibrated). This value was then smeared by a random Gaussian fluctuation corresponding to the width of the pedestal seen in the data: 10 counts for the pads and 5 counts for the bitubes. This data was then put into a format that was identical to the format

used for the real data. In this way, the same analysis routine could be used on the data and on the Monte Carlo, with extra information stored in the Monte Carlo events corresponding to the known generated values.

Besides the calorimeter, a best attempt was made to simulate all the physical volumes in E665, including metal walls and posts and volumes containing heavy gases such as Argon.

The output from these GEANT routines is equivalent to the 1st stage Monte Carlo output mentioned above, except for the addition of calorimeter information. The output from GEANT was then used as input to the 2nd stage Monte Carlo as described above.

GEANT was compared to EGS, the previous standard code for simulating shower tracks, and was shown to be equivalent in its results to the order of 1%.[29]

3.2 Data Analysis

There were essentially six stages in data analysis:

1. Data split by trigger type

2. Filtering of LAT and SAT events

3. Pattern Recognition

4. Track Fitting

5. Vertex Reconstruction

6. Particle Identification (including calorimetry)

Steps 3 through 6 were performed exactly the same way on data and output from the 2nd stage Monte Carlo. Each of these stages is discussed below.

3.2.1 Data Split

Since the data on tape was a random combination of the triggers mentioned before, it was decided that a more useful format would be to have all triggers of a given type to be separated onto individual tapes. This was accomplished by a simple tape to multiple tape copy job.

3.2.2 Filtering

Because of the inefficiencies in our main triggers (see the Triggering section) it was decided that the filtering out of the non-deep inelastic scattering events would save considerable time in the analysis steps below. This filtering step included a simultaneous tagging of probable high Q^2 events. The steps taken in filtering of the LAT data included:

1. 7 out of 7 of the SBT scintillators must have included a hit.

2. After pattern recognition, there must be only on line segment in the beam stations.

3. This beam must correspond to the specific SBT hodoscopes that fired. Then, if the event passed these criteria, a check was made to see if this event was consistent with a simple beam muon that passed through the forward apparatus. If so, then that event was discarded, otherwise the

event was kept for further analysis. This check for a non-interacting beam included the following:

1. There is at least 3 hits in the PSA detector.

2. There is only one forward spectrometer line segment after pattern recognition.

3. The forward spectrometer line segment, when traced back through the magnetic field of the CVM magnet, matches the beam line segment traced forward, to within tolerances for this procedure.

Filtering of the small angle trigger data was very similar except an extra check was made to see if the event corresponded to a bremsstrahlung or muon-electron scatter. This check was on the energy in the calorimeter. If the energy in the central 1 meter zone of the calorimeter exceeded 100 GeV and there was less than 10 GeV outside of this region, then this event was tagged as coming from an electromagnetic type of event, not a deep inelastic scatter. This event was subsequently filtered out.

3.2.3 Pattern Recognition

The software for finding the track a particle followed in the forward spectrometer was developed by a very large number of people. Essentially, each detector system has separate software (developed usually by members of the institutions that built the hardware) to find sets of hit points that belong to the same physical track. This is done usually by one of two methods: finding space

points or projections. Space points are locations in space that definitely belong to a physical track. They are obtained by finding the intersection of hit wires in planes very close together. These wires must be at angles to each other and, if they are too far apart, then the x position of the space point is not determined accurately and this method cannot be used. The alternative is to find projections of tracks. This is done by looking for straight lines (in the non-bending view or in areas where there is no magnetic field) that connect three or more hit wires in a given detector. If the projections are obtained independently in two views, then the equation of the line for the physical track can be obtained. Obviously, the majority of computer time is spent in determining which space points belong to the same track or which projections belong to each other. The output from this stage is a set of hit points that are associated with a line segment and relationships between these line segments.

3.2.4 Track Fitting

The next stage of data analysis is to take the information obtained in pattern recognition, essentially all the reasonable line fits to hit points in the detector, and associate them into physically reasonable tracks. First a cubic spline fit is made to the second derivative of the associated line segments obtained from the pattern recognition, assuming a trajectory that follows the Lorentz equations of motion in magnetic fields. This equation was integrated twice to obtain a quintic spline fit. This fit was compared to the data and the χ^2 was minimized.

The momentum of the track is one free variable as well as one physical point. These values are obtained from the minimization. Known sources of error such as multiple scattering are included in the fit. A probability is formed from this χ^2 value and cuts can be made on this probability.

3.2.5 Vertex Reconstruction

Once the track fitting stage of data analysis is complete, the search for the location of all vertices in the event takes place. Vertices are obtained by finding the closest point of approach of a set of tracks. First the primary vertex is searched for with the largest set of tracks available. Once this vertex is established, if some tracks approach no closer than a set maximum limit, then they are declared available for a second round of vertex fitting. This procedure repeats until no more vertices can be found. A hierarchical procedure is used to resolve any ambiguities there may be in determining the vertex a given track belongs to.

It was found that the majority of events that pass the filtering and track and vertex reconstruction stages are still in the high ν, low Q^2 region, as shown in Fig. 33 . Most of these events are electromagnetic in nature (i.e. muon bremsstrahlung or muon electron scatters) and only exist in the data because of the defocussing condition of having the target inside the first spectrometer magnet. These events were cut from my final data sample by event cuts that I made. (See Results section below.)
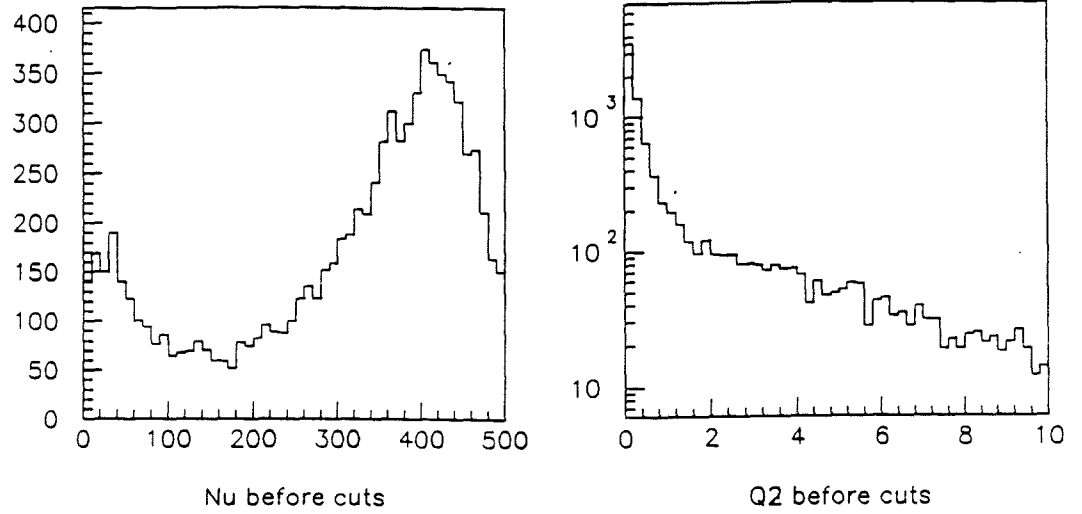
Figure 33. Event Kinematics after filtering and event reconstruction.
a) ν in GeV, b) Q^2 in $(GeV/c)^2$

3.2.6 Calorimeter Data Analysis

After all track fitting and reconstruction has been accomplished, the tracks

that have been found in the spectrometer can then be identified in some cases as

to particle type. The Cerenkov detectors can analyze lower momentum particles

and the RICH can identify particles in the dozens of GeV range. The calorimeter,

of course, is used to detect neutral photons that don't show up in the previous

stages.

Analyzing the data that comes from the electromagnetic calorimeter during

each event is a straightforward sequence of steps. However, at each step choices

had to be made about cut values and parameter options. What follows is a detailed list of these steps and a short discussion about the way in which we made decisions on these choices.

1. Subtract pedestals. The raw data from the Fastbus ADC's must have their zero point offsets, or 'pedestals', subtracted. These pedestals have been obtained by pulsing the ADC's in the interspill period. This data was available for every run and exists as a data base on the computer. However, the pedestal values obtained during the interspill period are not as accurate as would be desired, having been calculated from only 5 pulses. A better set of pedestal values was obtained by histogramming the ADC values during RBEAM triggers, since the muon is a minimimum ionizing particle and should leave very little energy . For the high range of the FASTBUS ADC's, we used pedestals obtained by linearly extrapolating pulsed data obtained after the run was over. During this period we fixed the ADC into its high range mode instead of leaving it in the automatic range finding mode as it was during the run. For the deuterium data taken in October of 1987, we had to use high range pedestal values obtained during the interspill period because several ADC's were changed during that time and no fixed high range pulsing was done.

2. Fix bitube oscillations. There were several periods, notably during the data taking period in 1987, when the signals from the summed anode

wires had a high-level oscillation imposed on them due to electronics prob-
lems. However, since this oscillation was uniform and in phase across the
calorimeter, it was possible to correct for this noise on an event-by-event
basis. Taking into account the phase differences, an average amplitude
was calculated and then this value was subtracted from the bitube signals
that were known to oscillate. Figure 34 shows the total energy in the pad
towers plotted against the total energy in the wires before and after the
above corrections were made for a representative sample of LAT data. The
improvement in the correlation between the two energy measurements is
remarkable.
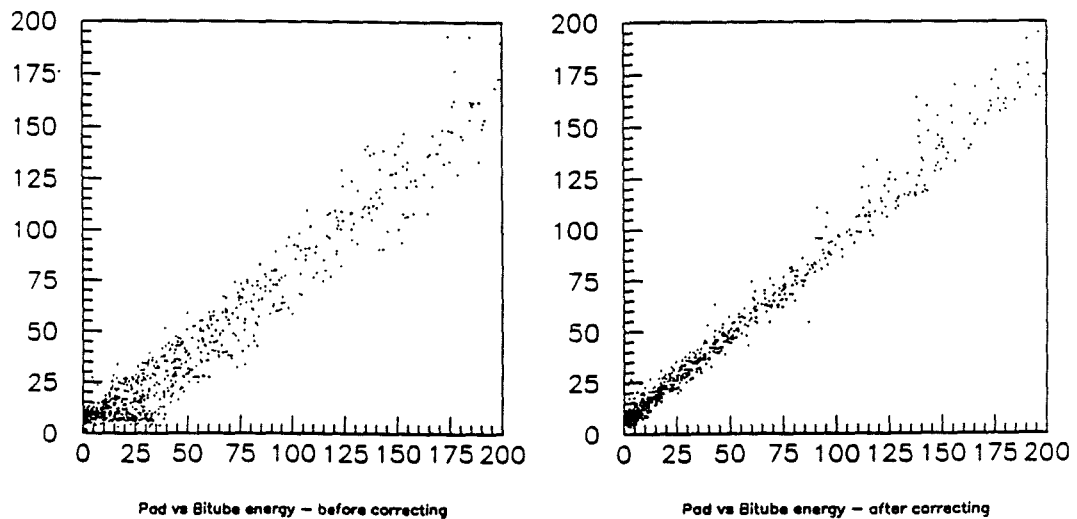
Figure 34.   Cathode vs. Anode Energy Correlation.   a) is before
correcting and b) is after correcting for the oscillating signals in the
bitubes.

3.   Discard channels below threshold. If a channel had a less than zero re-

sponse after pedestal subtraction, then it was automatically discarded. To limit the amount of non-zero data channels in each event it was decided that there should be an ADC count threshold for each data channel. These thresholds were:

$$Pad\,Pedestal\,Threshold\ = 25\ ADC\ counts \tag{46}$$

$$Bitube\,Pedestal\,Threshold\ = 20\ ADC\ counts \tag{47}$$

If a channel had less than the threshold values given in Eqn. 46 and Eqn. 47, then it was not included in the following translation and pattern recognition steps. Besides using the electron calibration data to determine these thresholds, many other somewhat subjective tests were made. These tests included a sharp pi zero signal in the data, a good cathode to anode ratio and not an overabundance of non-zero pad towers. Figure 35 shows how the pad threshold affects the response of the calorimeter, obtained from bremsstrahlung data by Michael Schmitt of Harvard University. As is shown, the fraction of energy found in the cluster does not change rapidly with choice of pad threshold. However, the amount of energy across the whole calorimeter, as well as the number of pads above threshold rises rapidly below 25 channels. It is not known if the calorimeter response, at some fixed threshold value, changes as a function of the incoming energy.

Number of Pads per Cluster

Cluster Energy / Momentum Loss : MEAN
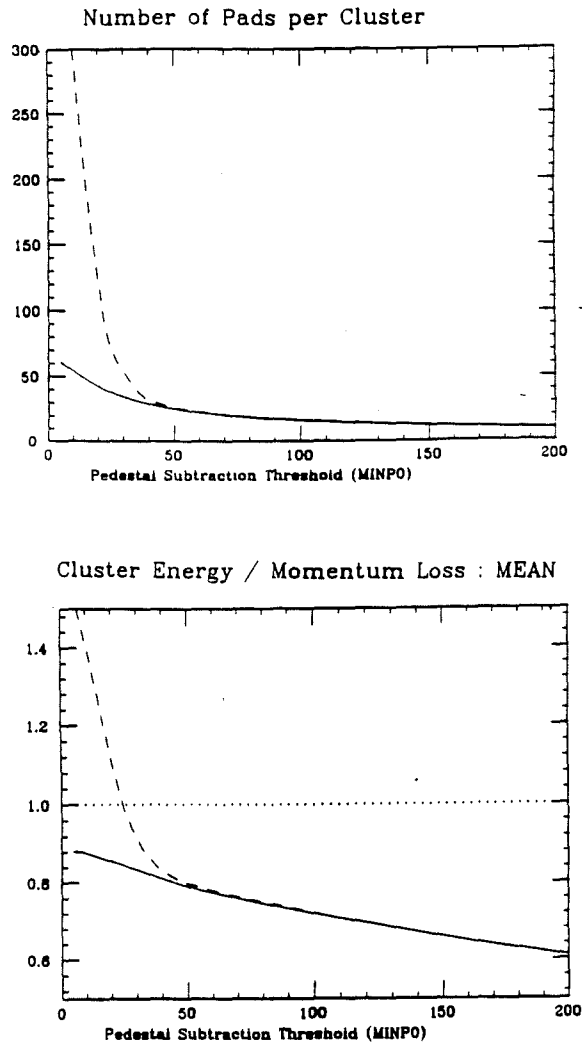
Figure 35.   Calorimeter Energy Response vs Pad Threshold.   a) Percent of shower seen in pads as a function of pad threshold, in ADC counts. b) Number of pads passing pad threshold as a function of pad threshold. The solid line in each case is for the found cluster while the dashed line is the response for the entire calorimeter.

4. Convert to energy. Using the calibration pararameters obtained as de-

    scribed in the calibration section, we could then translate each remaining

    data channel into an energy value by simple division by the gain factor

given in Eqn. 40 and Eqn. 41.

5. Correct for dead pads. Figure 21 showed the channels with zero response in the calorimeter. The electronically dead pad channels were corrected for by simply averaging over neighboring channels; the energy in all neighboring pad towers were summed and then the result was divided by the number of neighbors. The bitubes (and pads that lie above them) that were dead due to gas flow or electronic problems were corrected for in a more complicated fashion.

6. Correct for dead bitubes. As was mentioned in the calibration section above, using the electron data it was determined that many bitubes, mostly in planes 4 and 6, had gas flow problems, resulting in a much lower response in those bitubes and the pads attached to them. In Fig. 36 we can see that bitubes 8, 10 and 12 through 16 in plane 4 have a noticeably lower average fraction of the electron track energy than their neighbors. From analyzing graphs such as these, a single number was obtained describing this lowered response for each bitube that was dead for any reason, gas flow or electronics. In Table 6 I give a listing of these dead bitubes and the fractional shower energy missing due to them. After correcting for dead pad channels, we could then determine if any pads lay above one of these bitubes. If so, then the energy in that pad channel was divided by $(1 - \sum f_i)$ where f_i are the fractions given in Table 6 for

the bitubes under the given pad. A running total is kept of how much energy in each dead bitube is added to pads. At the end of looping over all non-zero pad channels, this total is then added to that bitubes energy (or created, if that bitube registered zero energy in this event).

PLANE 4/ETRAK VS YTRAK
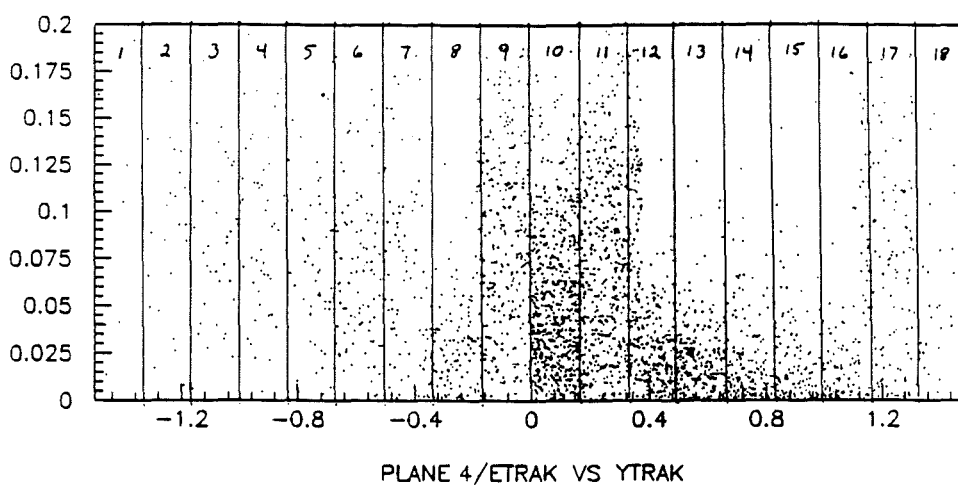
Figure 36.   Dead Bitubes in Plane 4.   This diagram shows the fraction of an electron's energy showing up in plane 4 as a function of Y position. Vertical lines represent bitube divisions.

7.   Correct for gas gain. The interspill monitoring data contained tempera-ture and pressure values at both the input and output gas gain monitors. The signals from these monitors was also read out and averaged. The gas gain monitors were calibrated to find the change in gas gain with respect to temperature and pressure and the best values for those parameters are given in the Monitoring section. This run dependent temperature and

Table 6. Dead Bitubes

Dead Bitubes		
Plane	Bitube	Fraction of shower missing
4	2	.06
	4	.06
	6	.06
	8	.06
	10	.06
	12	.06
	13	.06
	14	.06
	15	.06
	16	.06
5	10	.12
6	5	.12
	10	.10
	11	.05
	15	.05
9	10	.07
10	7	.07
	10	.03
	15	.05
12	5	.05
15	12	.02
17	12	.01
18	6	.01

pressure information exists as a data set on the computer and was read in on a run-by-run basis. Gas gain was computed as shown in Eqn. 39. All energy values for pad towers and bitubes were divided by this gain factor. Figure 37 shows how the pizero signal improves by becoming narrower after taking this gas gain correction into account.
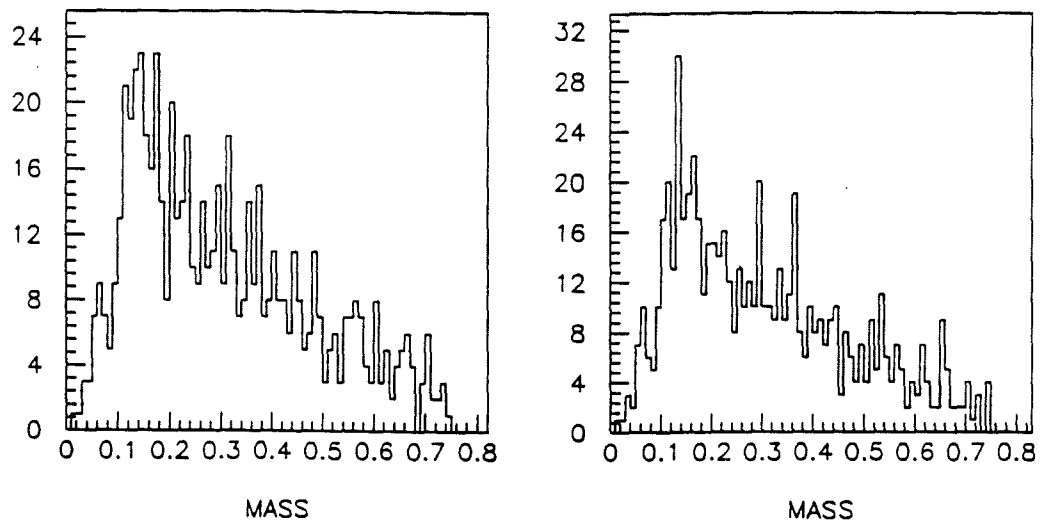
Figure 37. Change in Pi Zero Peak after Gas Gain Correction. a) is the invariant mass spectrum before gas gain corrections and b) is the same data after correcting. (Note change in scale)

8. Associate pad towers into clusters. This crucial phase of the calorimeter data analysis could be done with one of two possible clustering algorithms. The first is a routine that I wrote that uses a simple local clustering algorithm developed by Youssef, et.al. [30] . It associates pads to their highest energy neighbor, keeping track of the connections to form clusters. The second was developed by R. Nickerson of Harvard University and finds

local maximum points and searches radially outward for associated pads. This algorithm assumes a lateral shape for the shower. A comparison was made between these two algorithms and the differences are shown in Fig. 38 . This data shows that the results for multi cluster events show little difference except in the number of clusters. The difference in the latter is due to the different way the two algorithms deal with very low energy clusters. For this thesis I chose to use the clustering routine I wrote. The energy of the cluster is the sum of the energy of all pad towers associated with that cluster. The Y and Z position of the cluster is determined by finding the energy weighted mean of the Y and Z positions of all pads in the cluster. The offsets given in Eqn. 43 and Eqn. 44 were then subtracted from these values. A cluster was rejected for any further analysis for any of the following reasons: the cluster had an energy less than 4.0 GeV, the cluster was less than 10 cm from the edge of the calorimeter, or if the cluster consisted of only a single small size pad.

9. Associate anode signals with pad clusters. For all pad towers in a cluster, the bitubes that lay under that tower were considered to be associated with the cluster. In this way, a longitudinal profile could be built up for each cluster. The starting point for a cluster could be estimated by finding the plane after which 10% of the total shower has been developed. Another
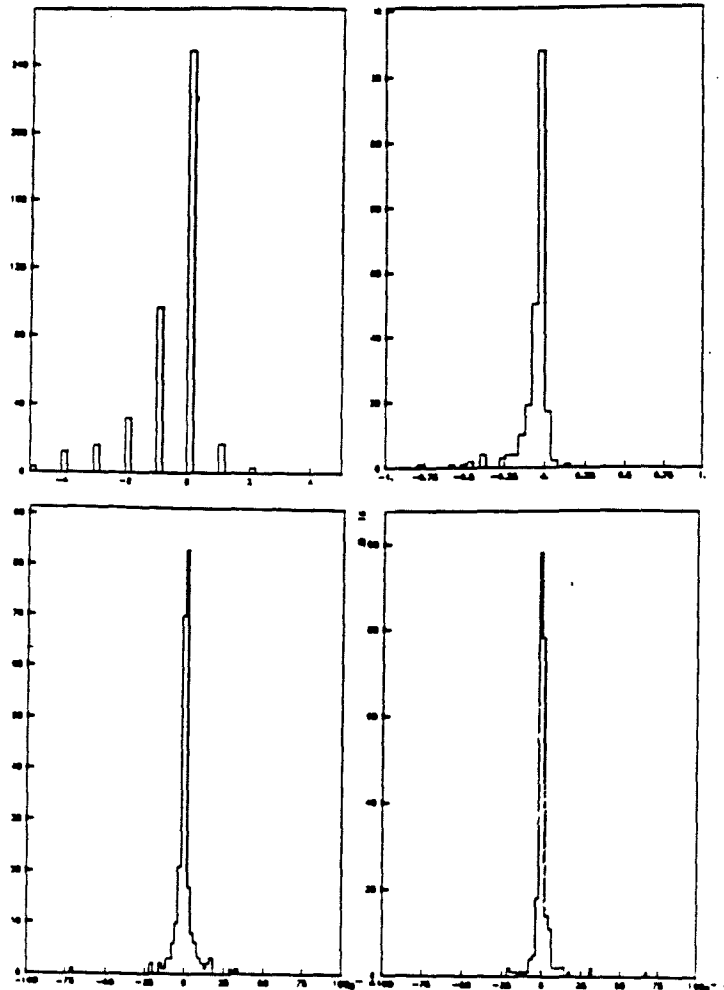
Figure 38. Comparison of two Clustering Algorithms. a) The difference in numbers of clusters found by the two clustering algorithms for those events with more than a single cluster. b) The fractional difference in energy of the largest cluster in those events c) The difference in Y position of the largest cluster. d) The difference in Z position.

useful parameter for each cluster obtained from the associated bitubes is

the energy in the back half of the calorimeter divided by the energy in the

front half. These two variables, as well as the mean longitudinal position

of the shower, were used to distinguish electrons from pions in the electron calibration data.

10. Find clusters associated with tracks in the forward spectrometer. After the track fitting stage of data analysis was performed, there exists a bank of data giving the hit positions and slopes of tracks up to the last set of drift chambers. Knowing the distance to the front of the calorimeter, these found tracks can then be extrapolated to there. A comparison was then made to each calorimeter cluster. Figure 39 shows the closest approach to cluster centers of charged tracks. There is a noticeable difference between the population distribution below 6 cm and above 6 cm. Thus this value was used to discriminate between clusters originating from charged particles and those coming from neutral particles. Approximately 12% of all clusters above 4 GeV are removed by this cut. Extrapolating the background distribution in Fig. 39 below 6 cm., one expects at most 5% of all neutral clusters to be discarded by this cut.

11. Find pairs of clusters that come from neutral pion decays. The algorithm used to find pi zeros for this thesis was a very simple one. First, all possible pairs of neutral clusters passing the cuts mentioned in the steps above were made. An invariant mass was formed for each pair of clusters using the expression:

$$m_{inv} = \sqrt{E_1 E_2} \frac{d_{12}}{R} \qquad (48)$$
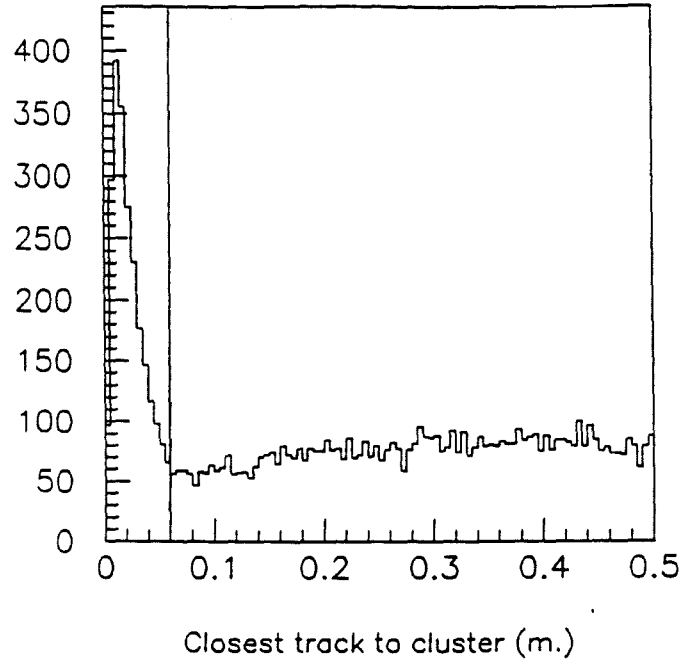
Figure 39. Closest Charged Track Hit to Cluster Center. The line is positioned at 6 cm.

where E_1 and E_2 are the energies of the two clusters, d_{12} is the separation of their centers and R is the distance from the face of the calorimeter to the interaction point in the target. Also, a χ^2-type of variable was formed for each pair by comparing the difference between this mass and the pi zero mass to the known sources of error in making the mass measurement. That is,

$$\chi^2 = \frac{(m_{inv} - m_{\pi^o})^2}{\sigma^2_{m_{inv}}} \qquad (49)$$

where

$$\sigma^2_{m_{inv}} = m^2_{inv} \cdot [\frac{1}{4}[(\frac{\sigma_{E_1}}{E_1})^2 + (\frac{\sigma_{E_1}}{E_1})^2] + (\frac{\sigma_{d_{12}}}{d_{12}})^2 + (\frac{\sigma_R}{R})^2] \qquad (50)$$

The errors in the energy measurement are known from Eqn. 42 and the error in the separation of the clusters is known from the positional resolution given in Eqn. 45. The error in the distance from the vertex, R , is arbitrarily set to be .5 meters. Now, this set of pairs of clusters, with a mass value and an associated χ^2 value, is sorted according to increasing χ^2. A cut on this variable is made such that a pair of clusters is not accepted as a pi zero candidate if its associated χ^2 is greater than 1. Finally, each pair in the list is declared as coming from the decay of a pi zero unless one of its clusters has been used in the list before it. The energy, momentum and kinematic variables associated with the parent pi zero are then easily determined from the energies and positions of the two clusters. One problem with this method (and any other method) is that the background distribution for the invariant mass spectrum of cluster pairs peaks in the pi zero region. Thus many false cluster assignments will be made. These misidentifications will depend directly on the signal-to-background ratio in the pi zero mass region In our case, I decided to add one extra requirement for pairs of clusters to be considered pi zero candidates. If a pair occurs later in the list that passes the χ^2 cut and uses one of the

same clusters as the current pair and their separation is lower than the current one, then the current candidate pair is not considered. This cut discriminates greater against the background than the true pi zero pairs. This was determined from a Monte Carlo study which estimated that the good identification to misidentification rose from a ratio of .73 to 1.08 with this cut with the loss in number of good identifications being 22%. (The details of the acceptance of this pi zero algorithm are discussed in the results chapter below.) To sum up simply, pi zeros are found from pairs of clusters by picking those pairs whose invariant mass is closest to the pi zero mass in accordance with the measurement errors. Cluster pairs are not considered if they are more than one measurement error sigma away from the pi zero mass. A candidate cluster pair is passed up if one of its clusters occurs in another good pair with smaller separation.

12. Find merged two-photon clusters. Since the mean angular separation of photons arising from pi zero decay varies inversely as a function of the pi zero energy ($\theta_{mean} = \frac{2M_{\pi^o}}{E_{\pi^o}}$), then very high energy pi zeros will tend to give clusters in the calorimeter that aren't distinguishable as being separate photons. This point begins to occur at around 60 GeV for our calorimeter (where clusters are distinguishable as separate when they are 10 cm or more apart). This energy value was obtained from a Monte Carlo study, whose results are shown in Fig. 40 . The simple step was

made of declaring all neutral clusters above 60 GeV that were not used in the previous step as merged photon pi zero decays. Besides pi zeros where one photon misses the calorimeter, the backgrounds for the production of neutral clusters at this energy and above are muon bremsstrahlung and direct photon production. Direct photon production occurs at a very low level. However, in our data, large muon bremsstrahlung events can pass our trigger. Most of these occur at high y values, .6 and up. An upper limit of 200 GeV was made for merged pi zeros.
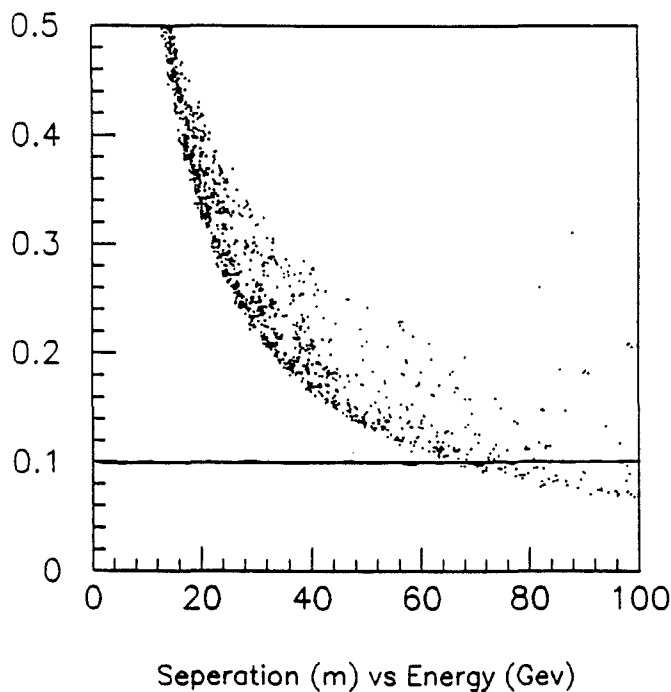

Seperation (m) vs Energy (Gev)

Figure 40. Pi zero photon separation as a function of energy The line shows the separation limit of the calorimeter, or 10 cm.

13. Identify single photons. All clusters that are not associated with charged

tracks and are not identified as coming from the decay of a pi zero (as outlined in the last two steps) are labelled as single photons. These photons arise from pi zero decays where one photon doesn't hit the calorimeter or from other processes such as bremsstrahlung.

For the results shown in this thesis, only those pi zeros found with separate clusters will be discussed. The merged pi zeros mentioned in the last step have a different efficiency of reconstruction than the separate ones and therefore contribute unevenly to physics distributions. The effective energy range for separated pi zeros is between 8 and 110 GeV.

The output from these steps of data analysis is a set of clusters with associated energy, Y and Z position and longitudinal properties, tagged either as a neutral cluster or charged, as well as a set of pairs of these clusters identified as coming from π^o decays (or, in some cases, only a single cluster). Properties of the pi zero such as the transverse momentum or z or Feynman x are determined with knowledge of the virtual photon direction in the lab frame obtained during the vertex reconstruction phase. The final output of my analysis is an accessible data set containing all event kinematics, knowledge of calorimeter properties (e.g. the number of clusters and energy in the cathodes and anodes), and, of course the kinematical variables associated with each identified pi zero or single photon cluster. The distribution of pi zero meson properties is discussed in the next chapter.

4. Results

(In the figures presented in this chapter, unless otherwise noted, data points are labelled with a solid cross or solid line while Monte Carlo comparisons are labelled with dashed crosses or lines.)

4.1 Event Sample

4.1.1 Accuracy and Bias of Event Reconstruction

An analysis was made to determine the accuracy and efficiency of the event reconstruction by comparing the output of the final vertex reconstruction phase to the known values for the event kinematics in Monte Carlo data. In Fig. 41 we see that the reconstructed event kinematics differ by less than 10% from the true values for most of the range in each variable and that the difference spectrum is centered on zero in all cases. The mean absolute percent error on the reconstructed variable W^2 is 6% while the value for the variable Q^2 is 5%.

Figure 42 shows the efficiency of reconstruction of kinematic variables, obtained by taking the ratio of the reconstructed distributions to the known Monte Carlo distributions. As can be seen, the efficiency is flat within statistical errors for most of the range of all variables and lies at approximately 60%. (The enhancement in the lowest bin is due to the failure of reconstruction, which gives a result of zero for each variable.)

4.1.2 Event Cuts

Using the information shown in Fig. 41 , Fig. 42 and Fig. 33 I decided that
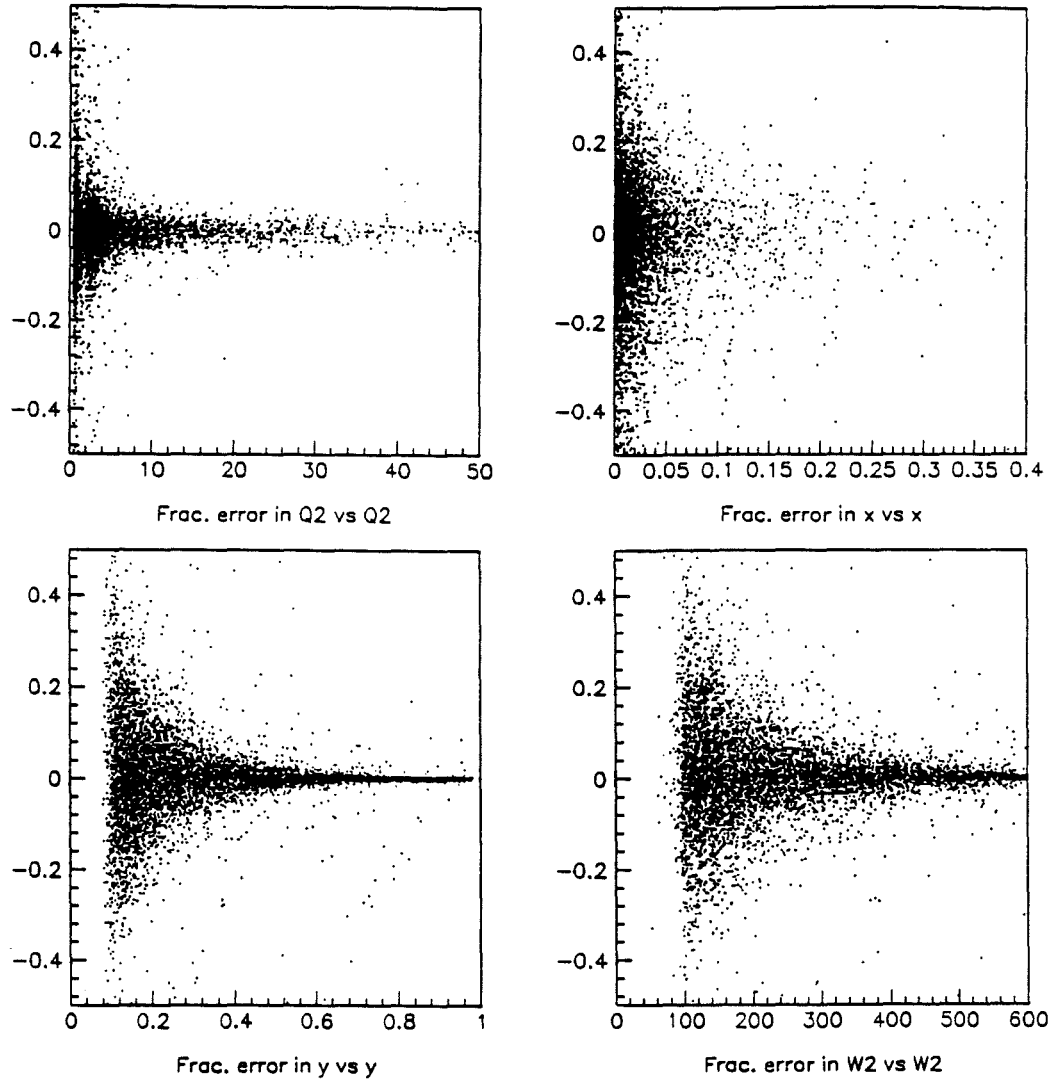
Figure 41. Error in Event Kinematics Reconstruction. Percent difference in reconstructed and known values vs. known values for a) Q^2 in $(GeV/c)^2$ b) x c) y and d) W^2 in GeV^2 .

the following set of event cuts would be used for this thesis:

$$100 < W^2 < 1000 \ GeV^2 \tag{51}$$
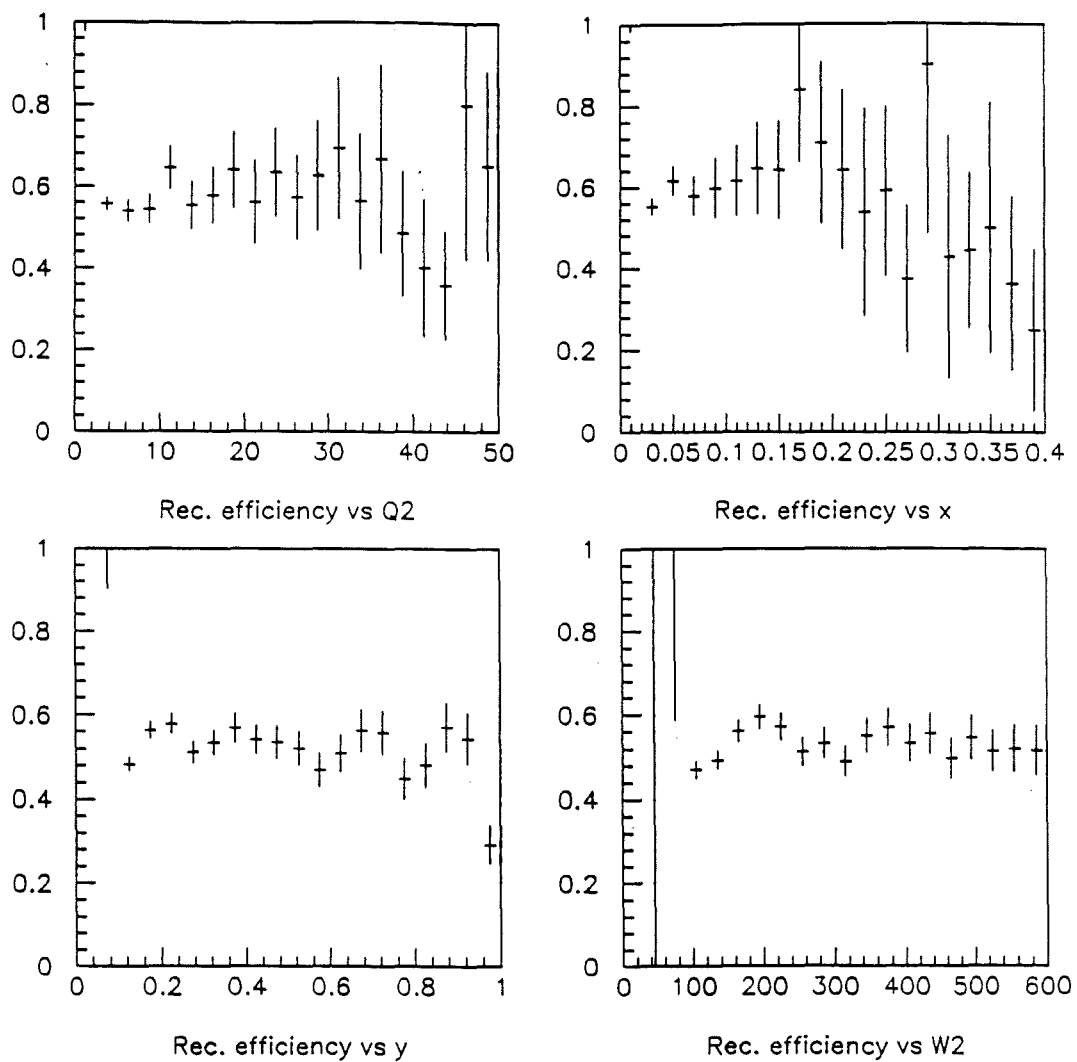
Figure 42. Efficiency in Event Kinematics Reconstruction. Efficiency of reconstruction as a function of known values for a) Q^2 in $(GeV/c)^2$ b) b) x c) y and d) W^2

$$50 < \nu < 500 \; GeV \qquad\qquad (52)$$

$$.1 < y < .6 \qquad\qquad (53)$$

$$Q^2 > 2.0 \ (GeV/c)^2 \qquad\qquad (54)$$

These cuts ensure that the data sample includes only those events where the acceptance of our trigger was not changing rapidly and the error on the measurement of the muon's momentum was small. The lower bound cuts on W^2, y and ν were chosen with some consistency in mind (i.e. W^2 can be approximated as $2M\nu$ which is about 100 GeV^2 for the lower ν cut; also a y value of .1 is around 50 GeV for the majority of the beam muons). Since a lower energy cut of 8 GeV is made for reconstructed pi zeros, the lower ν cut also enhances the probability that these higher energy pi zeros will be formed. The lower Q^2 and upper ν cuts ensure that the large amount of electromagnetic events in the data are not passed.

The two additional calorimeter cuts:

$$N_{neutral\,clus} \leq 8 \qquad\qquad (55)$$

$$E_{cal} > 10 \ GeV \ (pads \ and \ bitubes) \qquad\qquad (56)$$

are demanded. The first limits the number of possible background pairs in the search for pi zero candidates. The number of events with more than 8 neutral clusters is less than 1% of the total but the possible combinations of pairs of clusters in those events is large. The second calorimeter cut ensures that the calorimeter energy measurement is in a linear region and that the cathode and anode energy measurements will agree. This cut also is consistent with the lower bounds on y and ν. This cut does, however, bias the data towards events with a finite amount of neutral energy and may therefore give systematically higher values for neutral multiplicities.

The Monte Carlo events used as a comparison to the data were required to pass the above cuts. The GEANT simulation of showers in the calorimeter ensures that the cuts on calorimeter energy and cluster multiplicity are reasonably simulated.

After making these event cuts, it was found that the efficiency in reconstruction was still flat across the middle range of each kinematic variable. (See Figure 43 .) However, the efficiency of reconstruction drops quite drastically for the lowest Q^2 and x values. This is also true for the highest W^2 values.

The reason for low reconstruction efficiency at high W^2 is probably because of the higher particle multiplicity in those events, resulting in inefficient tracking and subsequent identification of the muon. The low efficiency for small x values
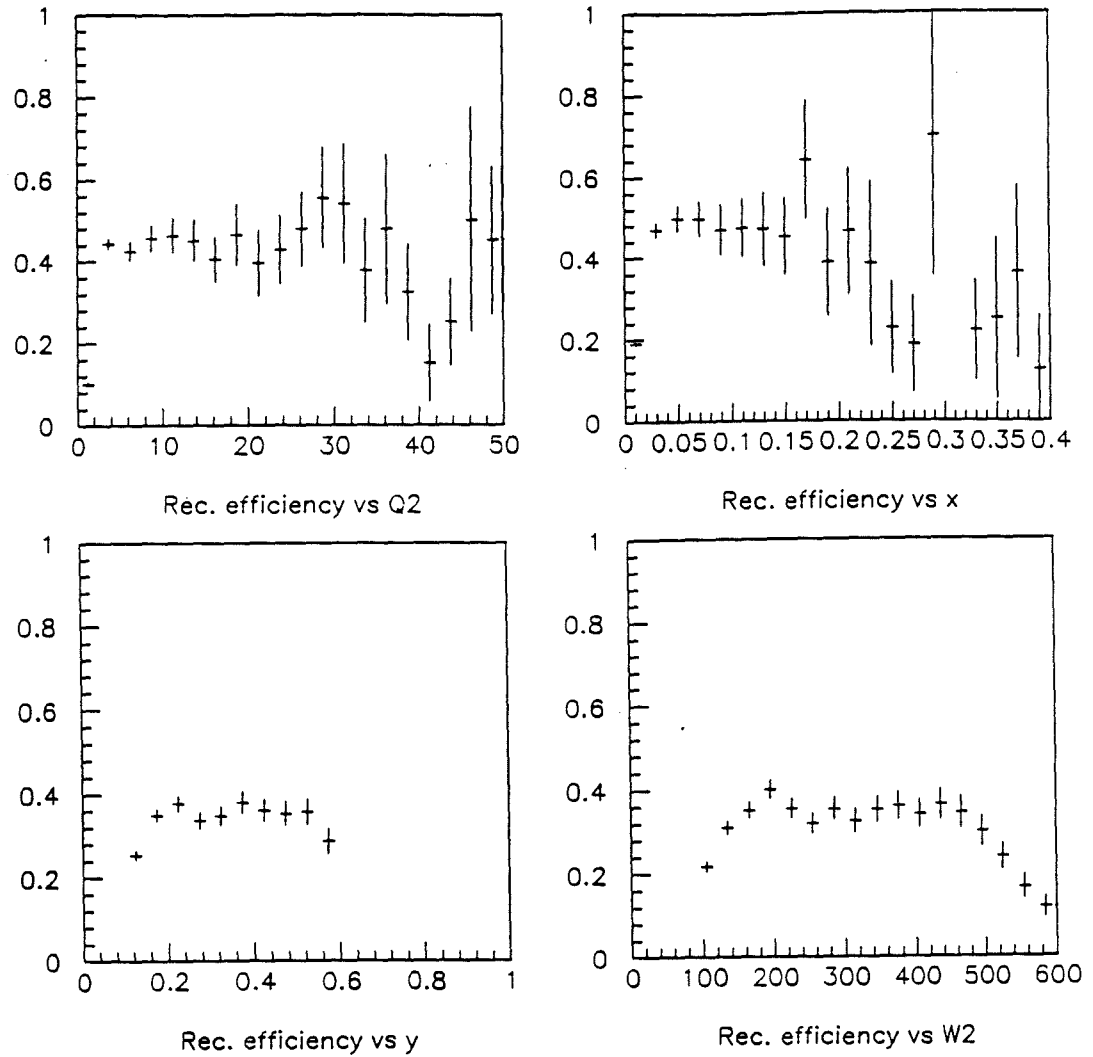
Figure 43. Reconstruction Efficency after Cuts. Efficiency of reconstruction as a function of known values after event cuts for a) Q^2 in $(GeV/c)^2$ b) x c) y and d) W^2 in GeV^2.

is a reflection of the low efficiency at small Q^2. The reason for this latter effect is probably due to the fact that for small Q^2, the scattering angle is small. When the muon is scattered at small angles it then passes through more dead areas, especially in the drift chambers. This results in a lowered probability of

reconstruction for that forward track, and thus for the event. This problem is enhanced by the added cut on ν and W^2, which ensure that the event will have a relatively high multiplicity.

4.1.3 Data Sets

The data sets shown in Table 7 were obtained. The number of events passing cuts were small for each data set. Most of the events cut are in the high ν, low Q^2 region that contains the electromagnetic events discussed earlier. (See Fig. 33.)

Table 7. Data Sets used for Analysis. This table shows the amount of data used from each data set.

Data Sets		
Target and Trigger	Num. of events	Num. passing cuts
Hydrogen LAT	109568	2122
Hydrogen SAT	110647	416
Deuterium LAT	114151	2776
Deuterium SAT	134687	816
Xenon LAT	120211	2121
Xenon SAT	89170	913
Total H2 and D2 LAT	223719	4898

A comparison was made between the pi zero properties in the Hydrogen and Deuterium data sets and the LAT and SAT data sets. No significant difference outside of statistical errors was seen. It was noted that because our trigger was

the logical OR of the individual triggers described in the Apparatus section, then some events were duplicated between the LAT and SAT sets of data (i.e. some events were split to both data sets.) Therefore I decided to combine all Hydrogen and Deuterium LAT data to obtain the largest data set possible. Unless otherwise noted, the figures in this chapter are for that set of events.

4.1.4 Data and Monte Carlo Kinematics Distributions

Figure 44 shows the event kinematics for the entire data sample. The results are normalized to the number of events passing the cuts. The comparison with Monte Carlo expectations is reasonable for most event variables. A somewhat harder Q^2 distribution is evident for the data. The largest difference occurs for the variable y. Less events occur in the data than in the Monte Carlo sample of events between y values of .1 and .2. An investigation was made on the effect of detailed trigger simulations on the Monte Carlo data set. These effects made the Q^2 distributions more similar but had little effect on the y distributions. This seems to indicate that the efficiency for reconstructing small y events is lower than accounted for by the simulation. The effect of differences in the Monte Carlo and data event distributions on results presented in this chapter is discussed in the systematic errors section below. The average of each variable for events passing the cuts are given in Table 8 .

4.2 Tracking Results

During the analysis of the data, the value was kept for the number of charged
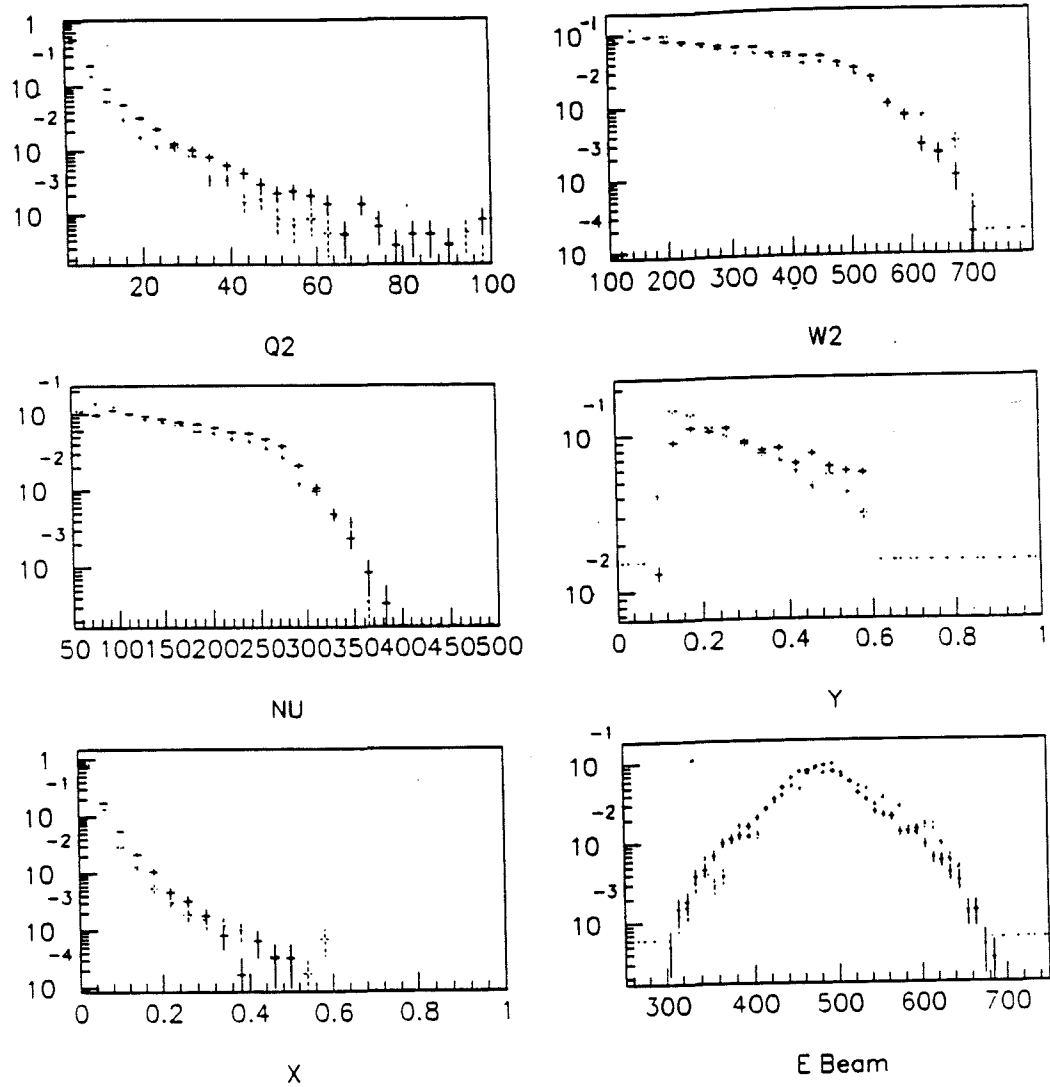
Figure 44. Event Kinematics for Data Passing Cuts. Distributions are for a) Q^2 in $(GeV/c)^2$ b) W^2 in GeV^2 c) ν in GeV d) y e) x_{Bj} and f) E_{beam} in GeV.

tracks that pass through the second set of drift chambers and that were found by the track finding code. Figure 45 shows the average number of these tracks as a function of the logarithm of W^2. For all particles created in the deep inelastic process, the expectation is that the average number should increase linearly with

Table 8. Average of Event Kinematics.

Event Variable	Average Value	Units
E_{beam}	481	GeV
Q^2	9.9	$(GeV/c)^2$
W^2	295	GeV^2
ν	162	GeV
x_{Bj}	.037	
y	.34	

respect to $ln(W^2)$. The slope of that dependence for all forward charged tracks has been measured by EMC and found to be .73, with the intercept consistent with zero. [31] The straight line fit shown in Fig. 45 is consistent with EMC's results. The intercept differs from the EMC value because the data shown is only for those charged tracks in the highly forward region, not all tracks in the forward hemisphere of the event. No study of the efficiency or systematic errors of track reconstruction was made. However, the effect of possible errors in tracking is discussed in the systematic errors section below.

4.3 Monte Carlo Results

4.3.1 Acceptances and Efficiencies

Before presenting results from the data it is useful to investigate the efficiency and acceptance of pi zero reconstruction using the calorimeter. This was accomplished by using the GEANT Monte Carlo simulation discussed above. The calorimeter analysis chain was used on each Monte Carlo event. Approxi-
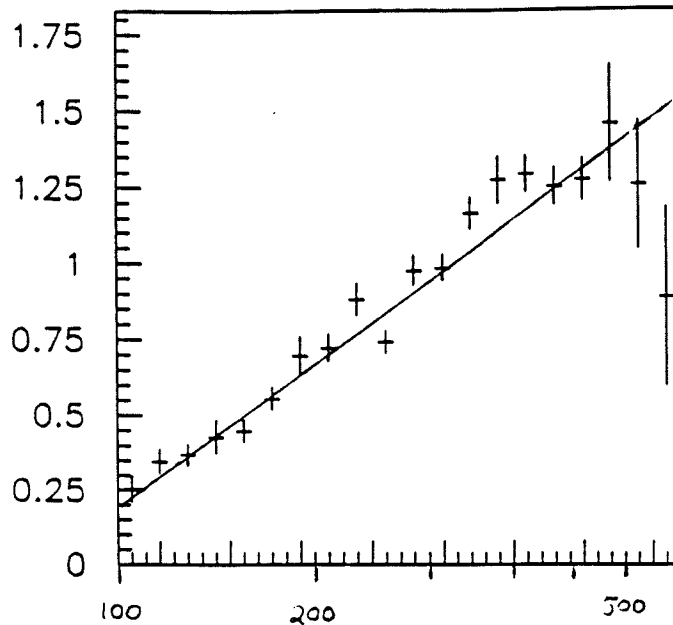
Figure 45. Average number of found charged tracks vs $ln(W^2)$ The average does not include the scattered muon. The slope of the fitted line shown is .70 ± .02 and the intercept is -3.0 ± .1.

mately 11 thousand fully reconstructed Monte Carlo events were generated that passed all the experimental cuts. (This number of events is about twice the number of data events. In graphs presented in this chapter where a comparison to Monte Carlo is made, no statistical error bars are given. They can be assumed to be on the same order of magnitude as for the data.)

Each identified pi zero candidate was compared to all possible pi zeros generated in the event. If the position of the clusters making up this pi zero differed by less than 10 cm in their position from where the actual photons

struck, then this pi zero was declared as being identified correctly. Otherwise, a misidentification was declared. For the case of 'merged' pi zeros, or those unpaired clusters above 60 GeV in energy, a misidentification was declared if either of the two photons hitting the calorimeter was more than 10 cm away from the position of the cluster found by my algorithm.

To understand what subset of pi zeros are able to be detected by the calorimeter, Fig. 46 shows what fraction of pi zeros generated in the set of Monte Carlo events can be detected by the pi zero finding algorithm discussed above. These acceptance functions were obtained by dividing the distribution of pi zeros whose clusters are greater than 4 GeV in energy, within 10 cm of the edge of the calorimeter and whose clusters are separated by more than 10 cm, by the distribution of all pi zeros. The geometrical acceptance increases rapidly with energy and is constant from 30 to 100 GeV. The acceptance increases rapidly at low Feynman x and z as well. The geometrical acceptance also increases steadily with respect to transverse momentum and becomes approximately constant after .3 GeV/c. Acceptance correction takes into account these effects by dividing by the acceptance functions shown in Fig. 46 .

Figure 47 shows what fraction of these detectable pi zeros are actually found by the analysis chain. Also shown is the fraction that are correctly identified. The difference between those two points is the fraction that is misidentified. These efficiency functions were obtained by taking the ratio of the distributions
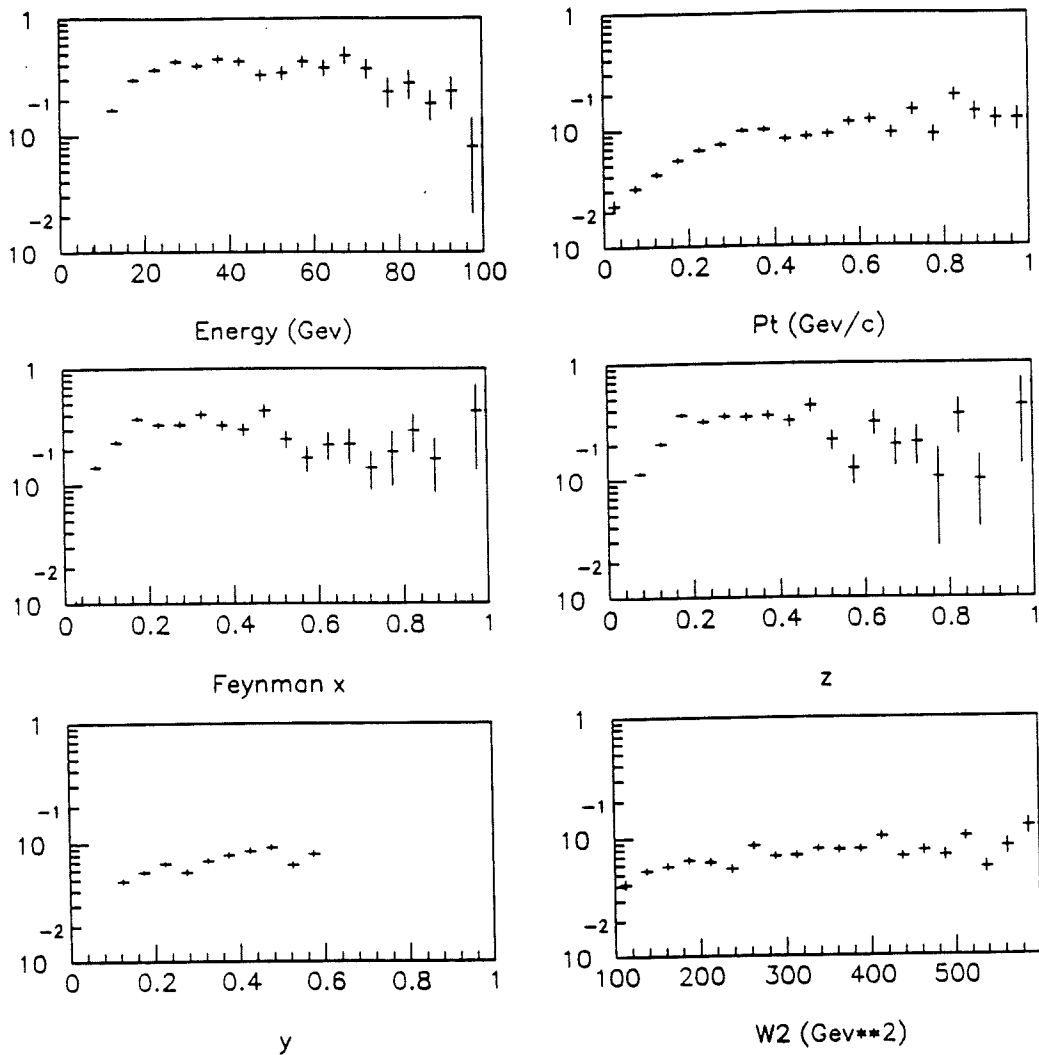
Figure 46. Geometrical Acceptance for Pi zeros. The fraction of pi zeros generated that hit the calorimeter with enough energy to be detected, as a function of a) E_{π^0} (in GeV) b) p_T (in $(GeV/c)^2$) c) Feynman x d) z e) y and f) W^2 (in GeV^2). These geometrical acceptances are for separated pi zeros only.

of pi zeros given by the output of the algorithm discussed previously to the distribution of known Monte Carlo values for those pi zeros both of whose photons hit the calorimeter with enough energy to be detected. (The efficiency is greater

than one in many cases because of the misidentifications made by the software.) Note that the efficiency as a function of event variables is constant. However, as shown, the efficiency as a function of energy increases steadily and then makes a large jump at the breakpoint between separate and merged clusters in my algorithm. This is a natural occurence due to the relaxing of requirements at this breakpoint. Since any large neutral cluster above the breakpoint energy is declared a pi zero, then more pi zeros will be identified at this stage than if it had to satisfy the strict cuts that pairs of clusters must pass. This point was also investigated in further detail. It was found that in most of the cases one of four possibilities occur. First is that the cluster identified as coming from a pi zero indeed does come from that decay, but the second cluster from the decay also exists and is further than 10 cm away. This means that this identified pi zero will not pass my criteria as being correctly identified, even though the majority of energy of the pi zero is in the found cluster. A second possibility for large energy clusters is that one of the photons from a pi zero decay interacts upstream of the calorimeter and produces an electron-positron shower. With the efficiency analysis program discussed above, these are labelled misidentified, even though the majority of the energy of the pi zero will be detected. Another possibility for large clusters is that it arises from the detection of one photon from a pi zero decay, with the other photon missing the geometrical acceptance of the calorimeter. One final possiblity that was noted in the simulation is that

large clusters may arise when the multiplicity of the event is very large and many clusters become merged into one. These last two possibilities are true misidentifications. The first three of these cases occur with approximately equal probability while the last happens infrequently.

Because the efficiency makes a large jump with respect to energy and is rapidly increasing for z and transverse momentum, I decided to use only separated pi zeros for the data discussed in this thesis. As shown in Figure 48 , the efficiency for these pi zeros does not show the large jump at higher energies and is much flatter in z and transverse momentum. There is still, however, an increase in efficiency as a function of pi zero energy. Given the energy dependent resolution of the calorimeter, this behavior is to be expected. There is also decreased efficiency for the highest values of z, as should be the case when the largest energy pi zeros are not counted.

Data from the pi zero reconstruction software can be corrected for the efficiency of this procedure as a function of any given variable by dividing by the appropriate efficiency function shown in Fig. 48 . This is noted when used.

Monte Carlo results presented in this section are either for those pi zeros that pass the acceptance criteria (i.e. with clusters above 4 GeV that hit the geometrical acceptance of the calorimeter) or for all pi zeros produced in the simulation. This distinction will be made when data is presented.
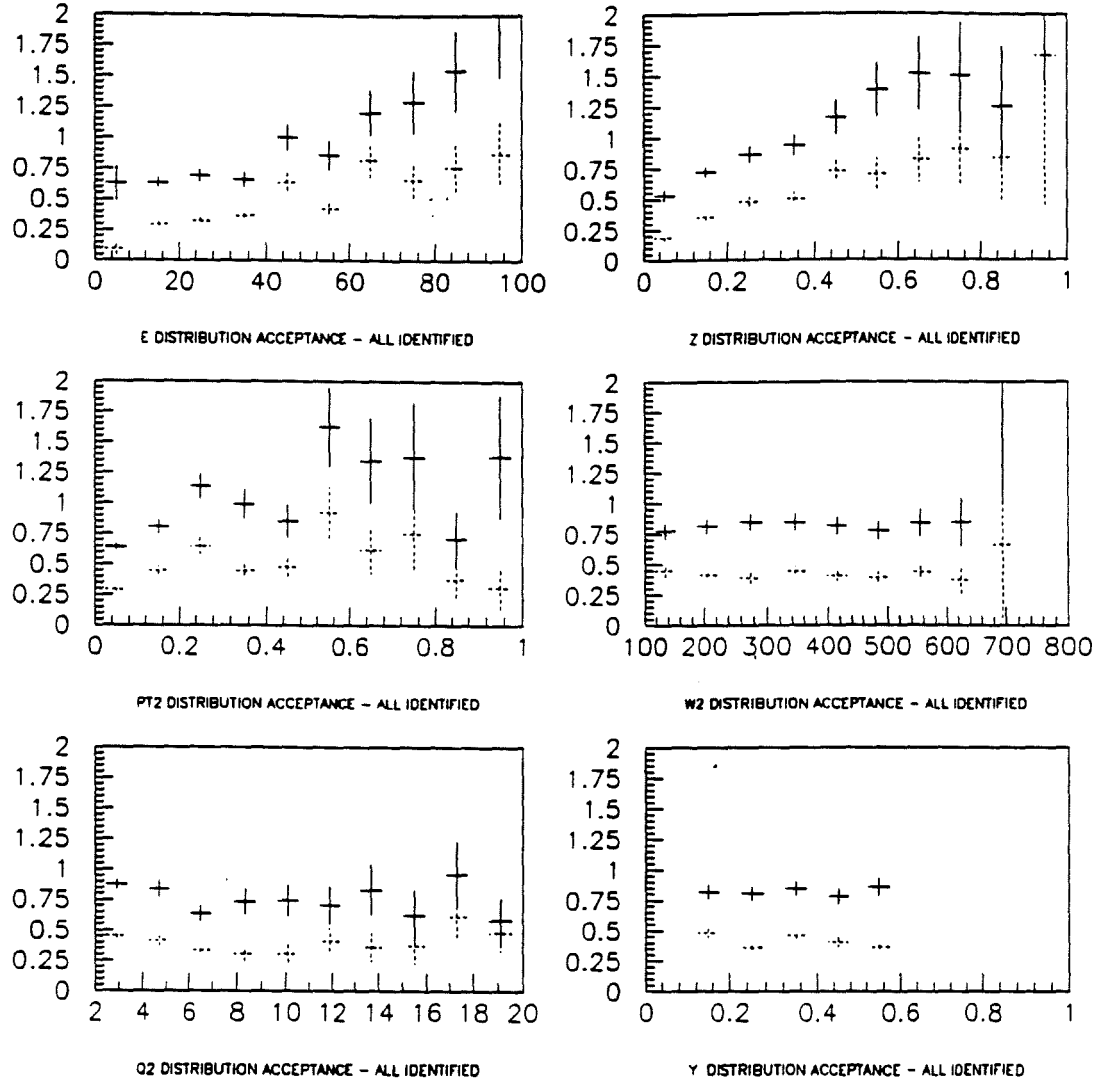
Figure 47. Fraction of All Pi Zeros found by algorithm. The fraction of detectable pi zeros found by the analysis chain as a function of a) E_{π^o} (in GeV) b) p_T (in $(GeV/c)^2$) c) Feynman x d) z e) y and f) W^2 (in GeV^2). The dashed points in each distribution are the fraction of pi zeros found that are correctly identified.

4.3.2 Errors in Cluster and Pi Zero Reconstruction

In Fig. 49 the fractional difference between reconstructed and true values for the various cluster and pi zero properties is given. The width of the error
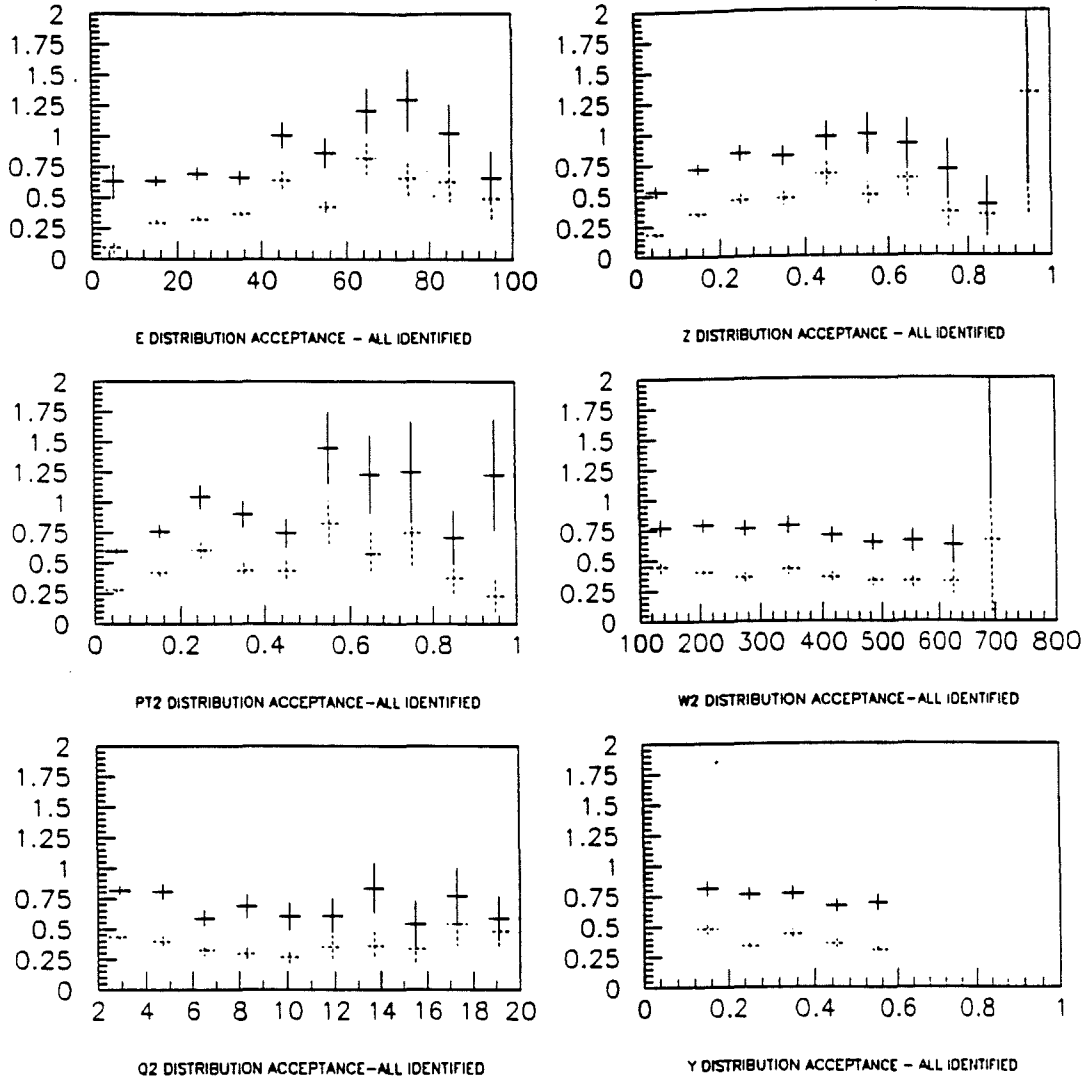
Figure 48.   Fraction of Separated Pi Zeros found by algorithm.   The
fraction of detectable pi zeros decaying into separated photons found by
the analysis chain as a function of a) E_{π^o} (in GeV) b) p_T (in $(GeV/c)^2$)
c) Feynman x d) z e) y and f) W^2 (in GeV^2). The dashed points in
each distribution are the fraction of pi zeros found that are correctly
identified.

distributions are 17, 9, 9 and 10 % respectively. These reconstruction error

estimates are better than for the physical calorimeter because the simulation

1400
1200
1000
800
600
400
200
0
−1−0.75−0.5−0.25 0 0.25 0.5 0.75 1

Rec. error for cluster energy

600
500
400
300
200
100
0
−1−0.75−0.5−0.25 0 0.25 0.5 0.75 1

Rec. error for sep. pi zero energy

600
500
400
300
200
100
0
−1−0.75−0.5−0.25 0 0.25 0.5 0.75 1

Rec. error for sep. pi zero XF

500
400
300
200
100
0
−1−0.75−0.5−0.25 0 0.25 0.5 0.75 1

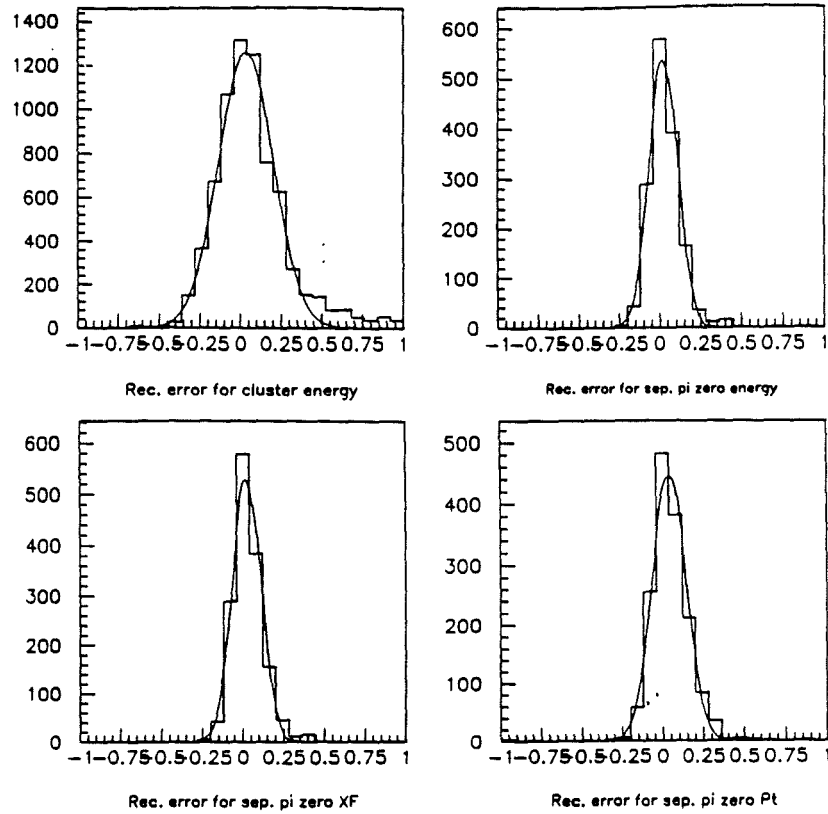Rec. error for sep. pi zero Pt

Figure 49. Reconstruction Error for Clusters and Pi Zeros. Fractional error in reconstructed a) energy of clusters b) energy of pi zeros c) Feynman x of pi zeros and d) p_T of pi zeros. These differences are for correctly identified pi zeros and clusters only.

could not account for all possible sources of error.

The effect of these errors on the results presented in this section is discussed below.

4.4 Calorimeter Results

4.4.1 Calorimeter Energy

Figure 50 shows the energy distribution in the calorimeter for the data with comparison to Monte Carlo. All distributions are reasonable in shape and match well with the results from the GEANT simulation. The average fraction

of available energy showing up in the calorimeter is 44% with an rms deviation of 21%. This distribution is peaked at approximately one-third, as would naively be expected if pions, positively negatively and neutrally charged, were generated equally. The average is above 33% because of showering in the calorimeter from charged hadrons as well as the neutral electromagnetic particles.

4.4.2 Neutral Cluster Properties

Various properties of clusters in the calorimeter are shown in Fig. 51 . All agree well with the GEANT simulation and are well behaved (symmetrical or monotonic).

Figure 52 shows the z distribution for all neutral clusters, normalized to the number of events. This data has been corrected for the geometrical acceptance of the calorimeter by an estimate obtained from a Monte Carlo study of neutral meson decays. (It was found that the correction factor for acceptance was negligible above a z value of about .1) The dashed line shows the Lund Monte Carlo z spectrum for photons arising from pi zero and eta decay only. The data is softer than the Monte Carlo distribution. This may arise from the absence of information on photons arising from other sources. However, another experiment has found that there may be an anomalous amount of soft photons in deep inelastic scattering. [32] The data shown here may confirm this result. This distribution was extrapolated to zero energy and the resultant z dependence was integrated to obtain the fraction of energy showing up as photons. (The exponential fit
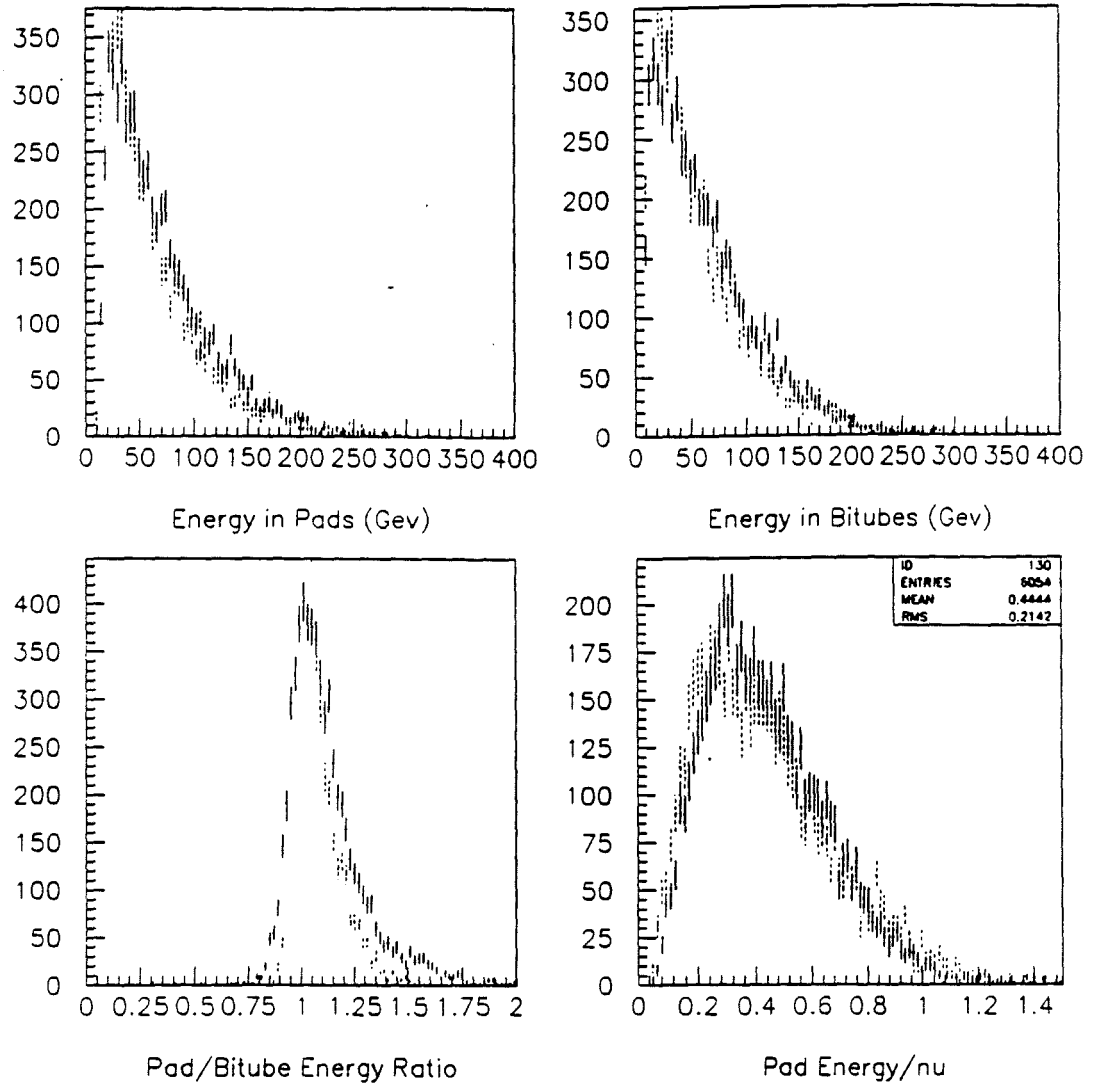
Figure 50. Energy in the Calorimeter. a) Total energy in the pad towers. b) Total energy in the bitubes. c) Ratio of pad energy to bitube energy and d) Total pad energy as a fraction of ν.

was made independently for the region below a z value of .3 and the region above that value. This breakpoint occurs because of the changing exponential slope of the data at that point. This behavior has been seen in electron-positron annihilation experiments.) The result is 27% ± 5%. The error was obtained by
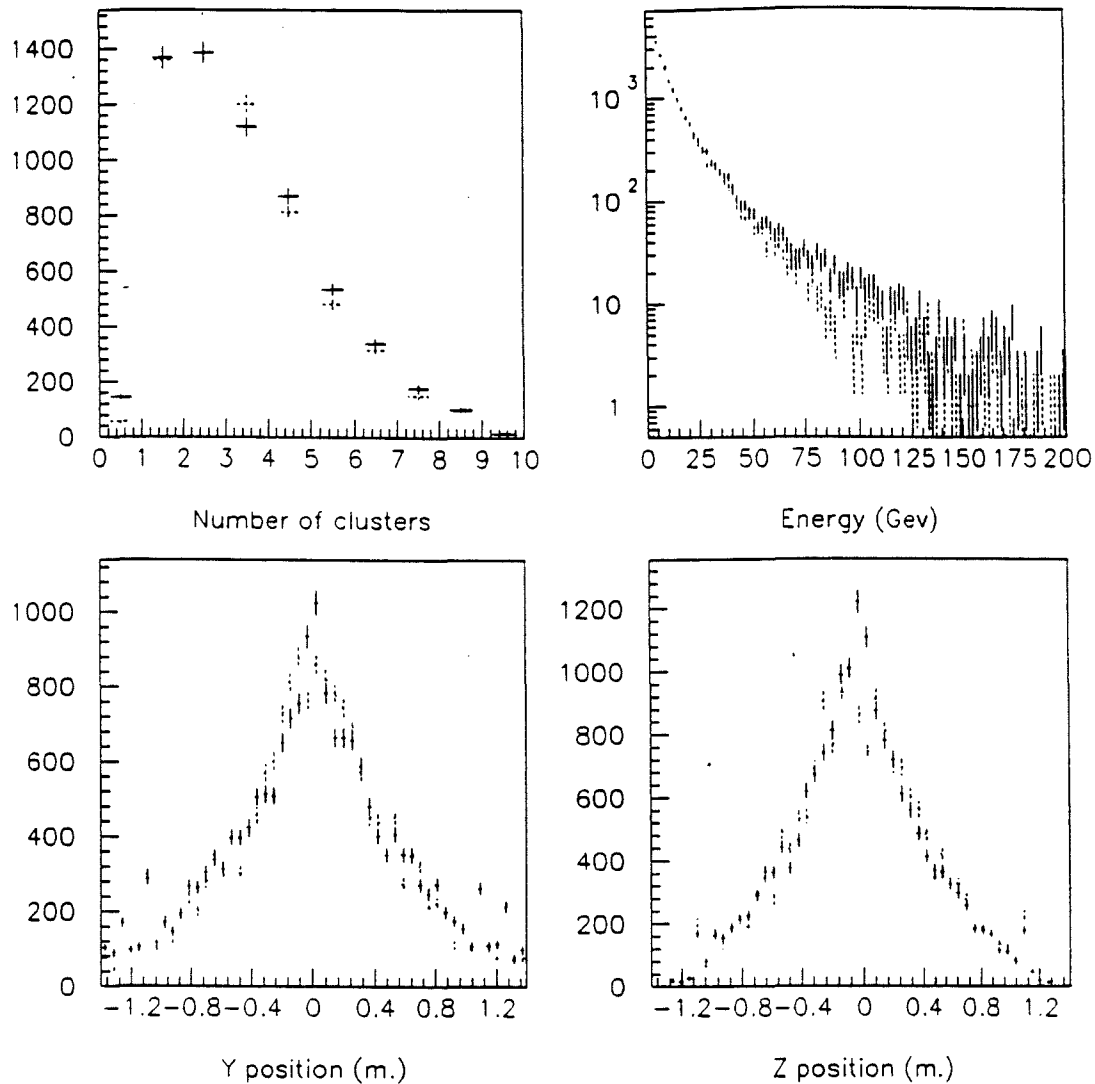
Figure 51. Electromagnetic Calorimeter Cluster Properties. a) Number of clusters per event, b) Energy of all clusters, c) Y position and d) Z position of all clusters. These figures include charged and neutral clusters. Monte Carlo results are normalized to the data.

changing the parameters of the integral, including the upper and lower limits, the number of bins and the values for the parametrization of the z dependence.

Figure 53 shows the invariant mass spectrum of all pairs of neutral clus-

1/N (dN/dz) for all neutral clusters
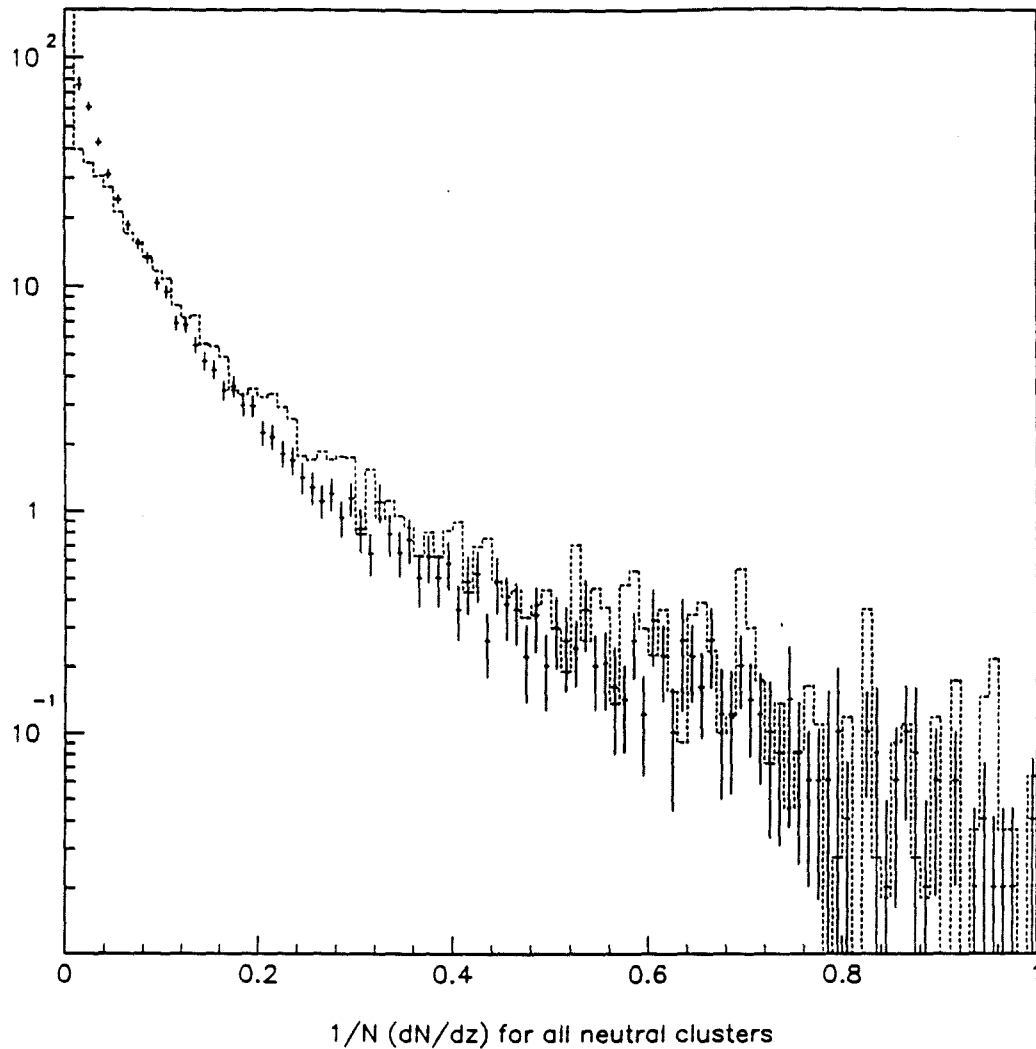
Figure 52. Z Distribution for Neutral Clusters. The data is normalized to the number of events and has been corrected for geometrical acceptance. Dashed line is Monte Carlo result for all photons arising from neutral meson decay only.

ters in all events passing cuts. A sharp peak at the pi zero mass is evident far above the background level. The estimate for background comes from combining random pairs of neutral clusters from different events, thus ensuring that no

correlation from pi zero decay occurs. If a background spectrum obtained from Monte Carlo simulation events is used, no perceptible difference is seen. The background subtracted spectrum is centered on the pi zero mass, thus verifying the calibration parameters obtained from electron and bremsstrahlung calibration. Note that since the normalization between the number of pairs in the background spectrum and the event spectrum is one-to-one, then the background is larger than the event spectrum, especially at higher values of mass. However, it was found that this normalization is the best estimate for background levels in the lower mass region. The Gaussian width of the peak shown is 40-45 Mev. The natural width of the pi zero is 7.6 ev and therefore the width shown is completely due to the resolution of the calorimeter. Using the resolution quoted in Eqn. 42, and assuming a pi zero decay into two 5 GeV clusters, then an estimate for what should be expected can be made: $\sigma_{mass} \approx (\frac{.44}{\sqrt{5}} + .07) \cdot m_{\pi^o} \ Mev = 37$ Mev. This width is consistent with that found in the data.

Note that at least half of the neutral cluster pairs in the pi zero mass region can be attributed to background pairs. This is the reason for the low signal/background ratio of the pi zero finding software discussed above. This situation can be improved in one of two ways: increasing the minimum energy cluster requirement, thus shifting the peak of the background to a higher mass, or by making a more stringent cut on the number of clusters in an event, thus giving fewer background combinations. However, the cuts made in this fashion
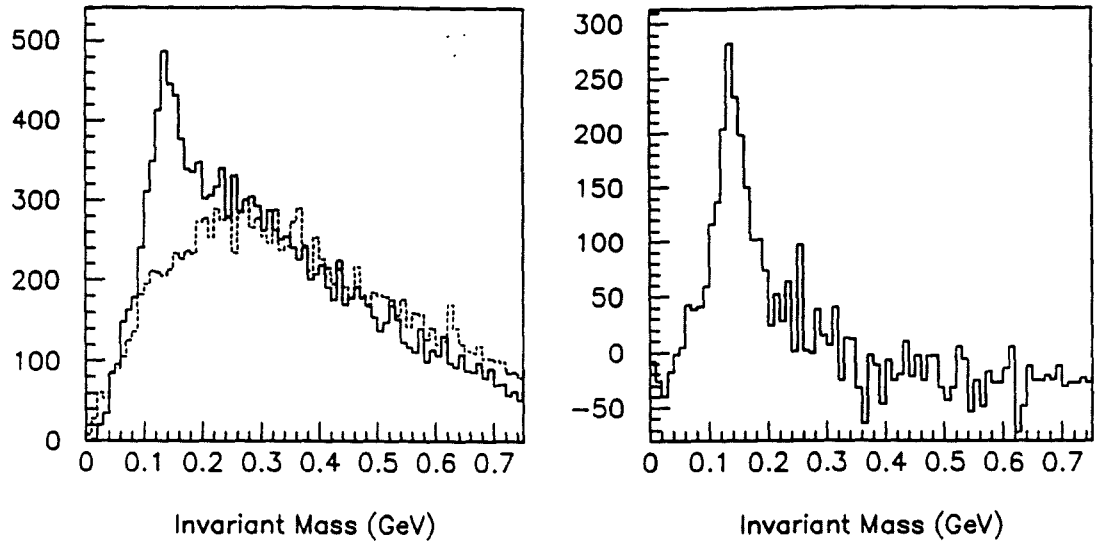
Figure 53. Invariant Mass for all Events. a) The invariant mass of all pairs of neutral clusters above 4 GeV. The dashed line is a background estimate obtained from data. b) Background subtracted mass spectrum.

affect the pi zero and event variables quite dramatically and I decided to continue with the cuts discussed. (As will be discussed below, to observe the eta signal I had to make the strictest cut possible in the number of clusters per event.)

4.4.3 π^o Production

4.4.3.1 Multiplicities

To determine the multiplicity of forward pi zeros in our data sample I relied on the simple procedure of counting the number of pairs of clusters in the invariant mass spectrum after subtracting an estimate for the background

obtained from random combinations in the data. This method does not rely on Monte Carlo estimations for the efficiency of the pi zero finding algorithm and is therefore a more reliable method of counting. The invariant mass is binned in 30 bins between 0 and 500 Mev and the counting is limited to between 33 and 233 Mev. The total number of pairs above background is divided by the number of events and an average forward pi zero multiplicity is obtained. This procedure is repeated for various ranges in W^2, Q^2 and Bjorken x.

For the entire data sample, there were 1953 ± 45 π^o's identified by using the invariant mass spectrum, which averages to .40 ± .01 detectable pi zeros per event. The Lund model Monte Carlo sample of events contained .34 ± .01 detectable pi zeros per event. As discussed below, the systematic error in this counting procedure is 30% and therefore the result is within experimental uncertainty of the Lund value. An investigation into this procedure for counting pi zeros using the GEANT simulated events determined that this procedure gives consistently higher results than the true number of pi zeros hitting the calorimeter. The data is consistent with this finding.

Figure 54 demonstrates how the pi zero multiplicity can be obtained in this fashion for different ranges in the variable W^2. Figure 55 shows the average number of pi zeros as a function of the logarithm of W^2. The average rises linearly with the logarithm of W^2 as expected from theory. If one assumes all pions are generated with an equal probability, given isospin invariance, then

the average multiplicity should approach half that for all charged pions at the highest W values. The value of $(.24 \pm .02)$ for the slope is lower than half that found for charged tracks, $(.70 \pm .02)$. However, systematic studies of the charged track reconstruction efficiency were not made for this thesis. The comparison to Monte Carlo results is good, with the consistently higher values of pi zero multiplicity due to the error in the counting procedure. No significant differences in the overall W^2 dependence are seen.

Figure 56 shows how correcting for the geometrical acceptance of the calorimeter increases the pi zero yield. The correction is made using the Monte Carlo events, seperately for each W^2 region. No comparison exists for pi zero multiplicity at these values of W^2. However, an extrapolation of pi zero multiplicity from a lower region of W in neutrino inelastic scattering shows no significant difference beyond the errors in the extrapolation.

Table 9 gives the data shown in Fig. 55 and Fig. 56 .

In Figure 57 we see that the average multiplicity of pi zeros formed in the deep inelastic process does not depend on Q^2, as expected from scaling considerations. Instead it lies at a constant value of $.4 \pm .04$ detected π^o's per event. The last data point, at a value of $Q^2 = 28.2\,(GeV/c)^2$, shows a slight increase from lower Q^2. This is consistent with the level of scaling violations to be expected but this increase may also be purely statistical in nature. The data shown has been averaged over all values of W^2. The data agrees very well
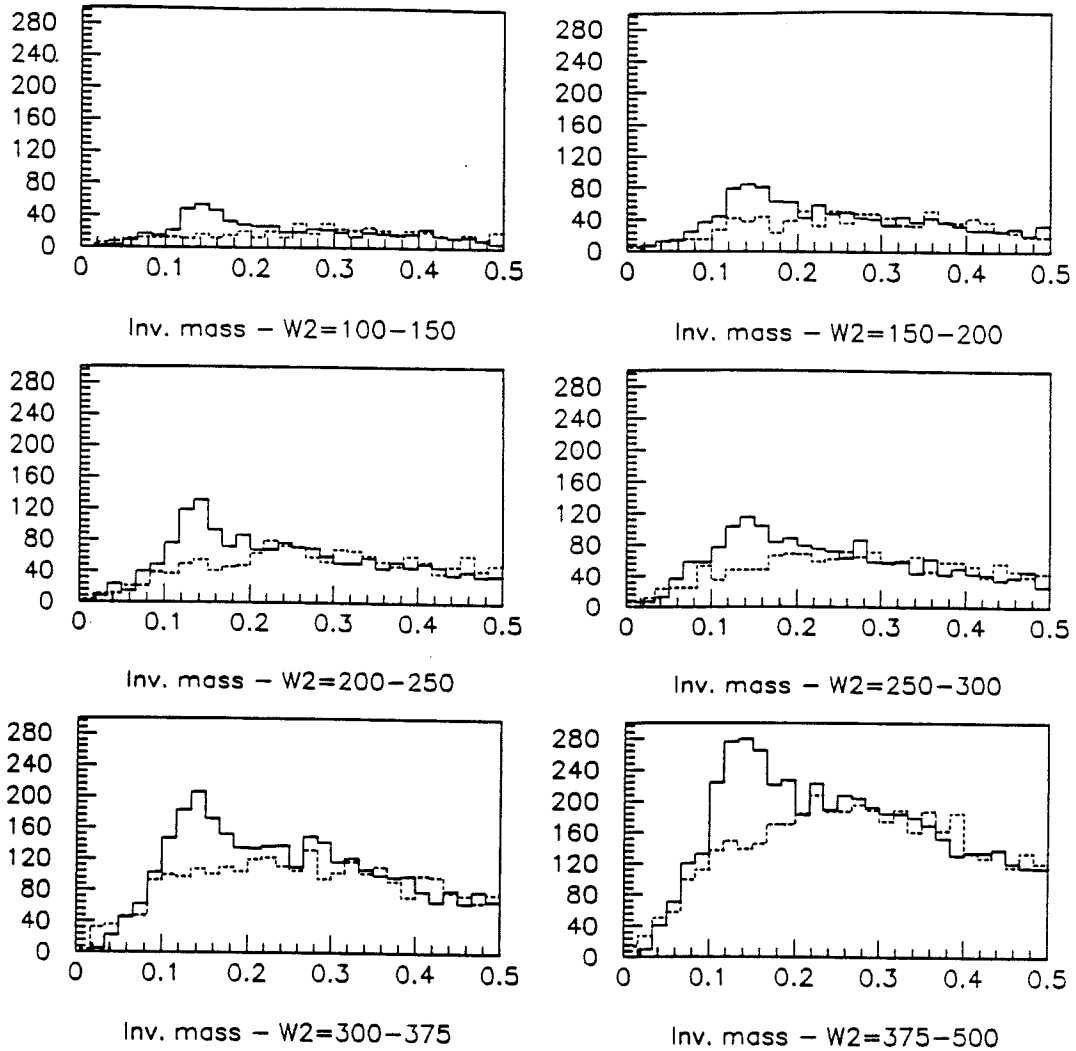
Figure 54. Invariant Mass Distributions for different W Ranges. The dashed line is an estimate for background obtained from the data.

with Monte Carlo values. No significant dependence on Q^2 outside of statistical fluctuations is seen after correcting for geometrical acceptance. The geometrical acceptance correction factor for data averaged over Q^2 and W^2 is 14.7 ± .3, which gives a neutral pion multiplicity for the entire data set calculated in this

Figure 55.   Average number of pi zeros vs logarithm of W^2.   This data has not been corrected for geometrical acceptance. The slope of the straight line fit to this data is .24 ± .02 and the intercept is -.94 ± .11 . The dashed line is a Monte Carlo comparison for detectable pi zeros.

manner of 5.7 ± .6 particles per event. This is one statistical error deviation away from the Lund Monte Carlo value of 5.1 π^o's per event.

Table 10 gives the data shown in Fig. 57.

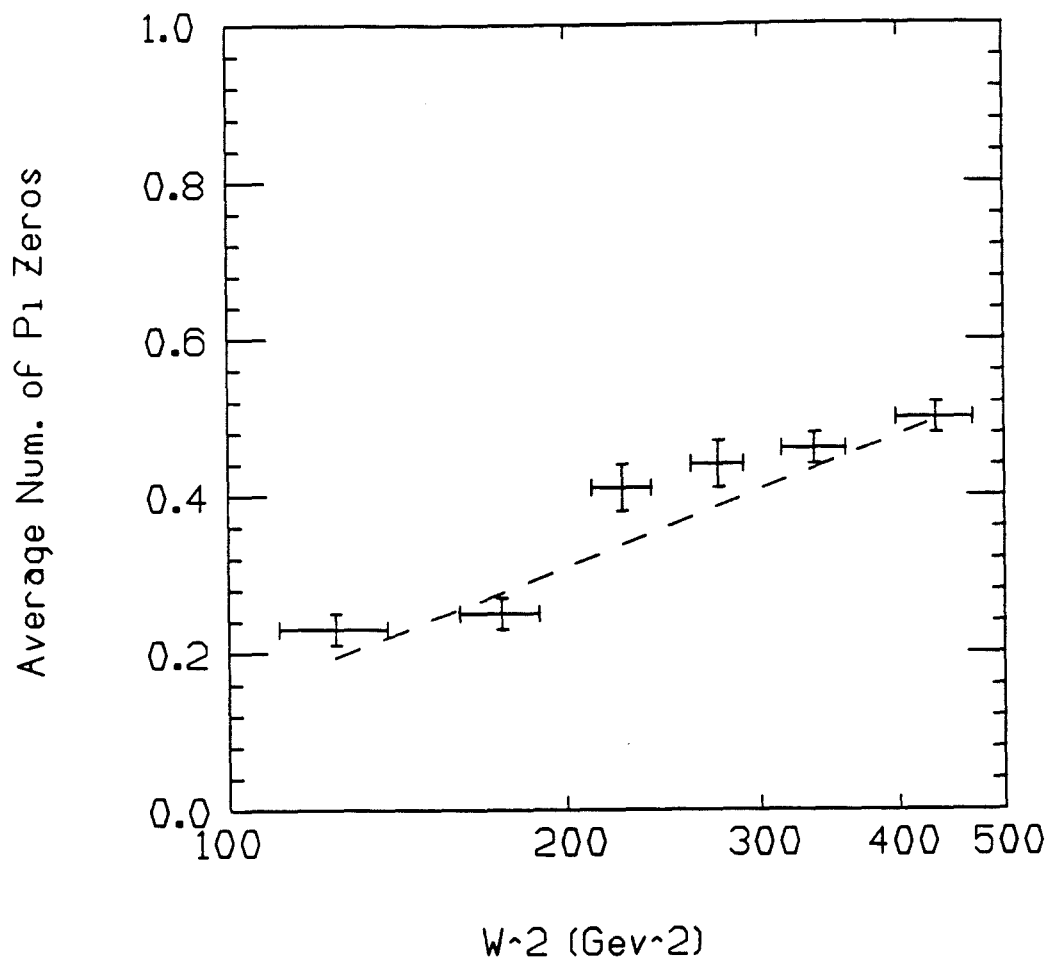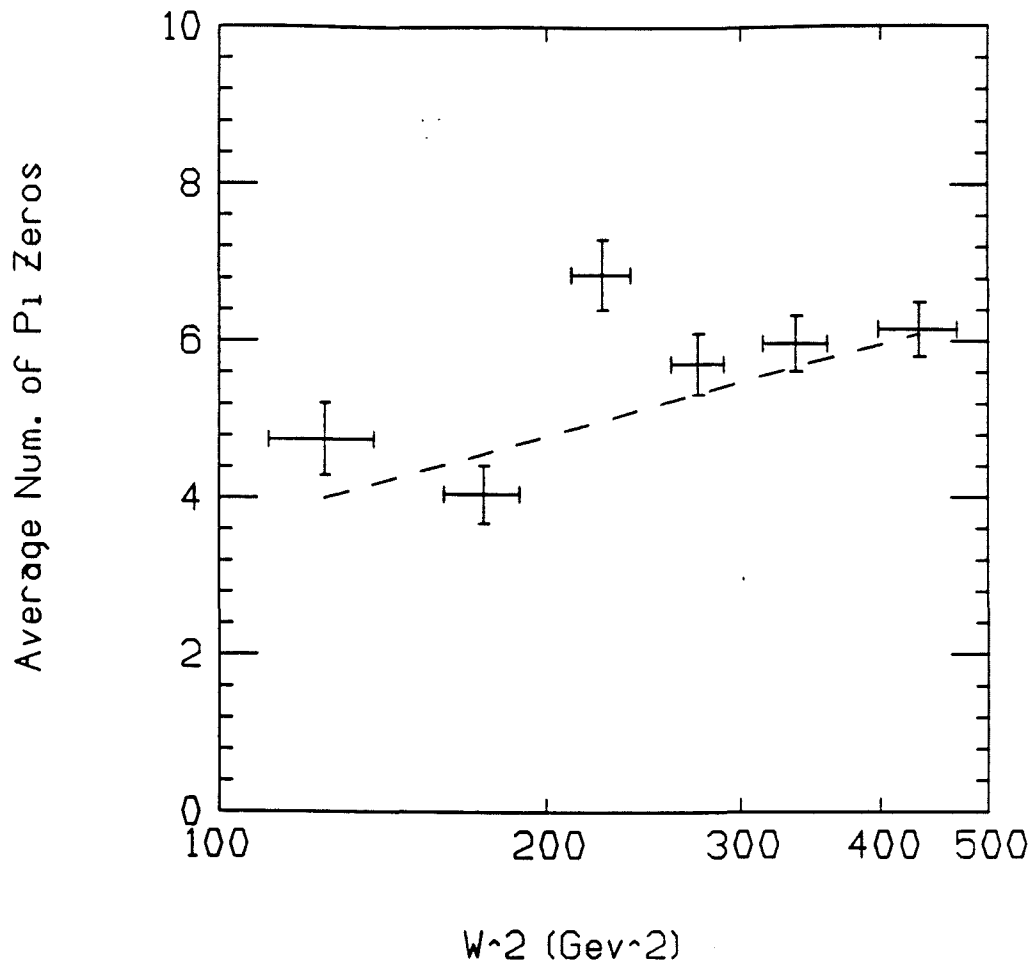Figure 56.   Corrected Average number of pi zeros vs logarithm of W^2. This data has been corrected for geometrical acceptance. The slope of the straight line fit is 1.49 ± .39 and the intercept is -2.67 ± 2.19 . The dashed line is a Monte Carlo comparison for all generated pi zeros.

It is useful to see if the multiplicity of neutral pions depends on Q^2 for fixed ranges of the variable W, since it has been shown that the multiplicity depends strongly on this latter variable.   In Fig. 58 we can see a difference

Table 9. Multiplicity of Pi Zeros as a function of W^2.

W^2 Range	$\langle W^2 \rangle$	σ_{W^2}	N_{evts}	N_{π^o}	$\langle N_{\pi^o} \rangle$	$\sigma_{N_{\pi^o}}$	Acceptance Correction
100-150	125	14	670	156	.23	.02	20.6 ± 1.0
150-200	175	14	786	197	.25	.02	16.2 ± 0.7
200-250	225	14	657	272	.41	.03	16.8 ± 0.8
250-300	275	15	615	269	.44	.03	13.0 ± 0.6
300-375	336	22	788	365	.46	.02	13.0 ± 0.5
375-500	433	35	1008	503	.50	.02	12.3 ± 0.5

between the Lund Monte Carlo and the data for all W ranges. An increase in

pi zero multiplicity is seen when a decrease is expected for the W=12-15 GeV

and W=15-18 GeV. The statistics are low for the highest points, however. A

decrease in pi zero multiplicity is seen at the highest W range. However, the

difference from Monte Carlo expectations is statistically uncertain to a high

degree. Table 11 gives the data shown in Fig. 58.

Finally, the behavior of pi zero multiplicity vs Bjorken x is shown in Fig-

ure 59 . The data shown is restricted to the three ranges of W used previously.

Again, for the lowest W range studied, an increase in π^o multiplicity is seen

for increasing Bjorken x (and thus increasing Q^2 by way of the relation shown

in Eqn. 1). This verifies, with more statistical weight, the conclusion that the

multiplicity of pi zeros differs significantly from the Lund Monte Carlo at large

values of Q^2. The average W^2 in the Bjorken x ranges studied cannot explain
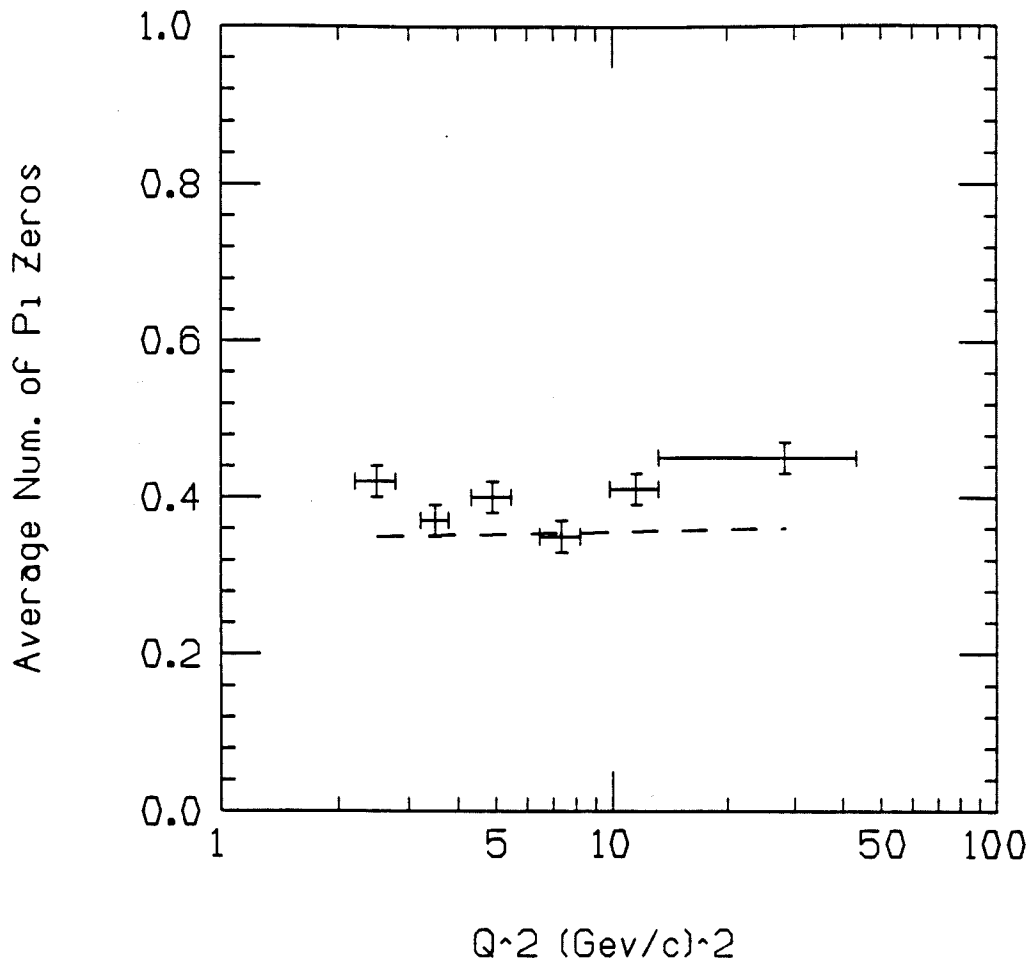
Figure 57. Average Number of Identified Pi Zeros vs the logarithm of Q^2. Dashed line is Monte Carlo results for detectable pi zeros.

the increase in pi zero multiplicity as a function of x. (In fact, as one increases Bjorken x for a fixed W range, the average W^2 is decreasing, which alone should give a lowered pi zero multiplicity, not a higher one.) No change in the average number of calorimeter clusters was evident for each range of W. The data shows

Table 10. Multiplicity of Pi Zeros as a function of Q^2.

Q^2 Range	$\langle Q^2 \rangle$	σ_{Q^2}	N_{evts}	N_{π^o}	$\langle N_{\pi^o} \rangle$	$\sigma_{N_{\pi^o}}$
2-3	2.49	.29	716	303	.42	.02
3-4	3.50	.29	707	262	.37	.02
4-6	4.90	.58	1060	420	.40	.02
6-9	7.34	.86	899	319	.35	.02
9-15	11.47	1.72	731	298	.41	.02
15-100	28.16	14.99	769	349	.45	.02

an unexpected decrease in multiplicity with respect to x_{Bj} at the highest W range with a reasonably high degree of statistical confidence. Table 12 gives the data shown in Fig. 59.

This behavior with Q^2 and Bjorken x has been been observed in EMC for charged pions and was attributed to scale breaking due to increased gluon emission at the higher Q^2 values. No explanation has been made for the dependence on W of this behavior. [33] This previous result is shown in Fig. 60 .

The data was checked to determine if this effect occurs for both the hydrogen and deuterium data, but due to lack of statistical information, no definite conclusion could be made.

4.4.3.2 π^o Properties

To determine the properties of identified pi zeros, the search software must be used. The results from the pi zero finding algorithm described in the last

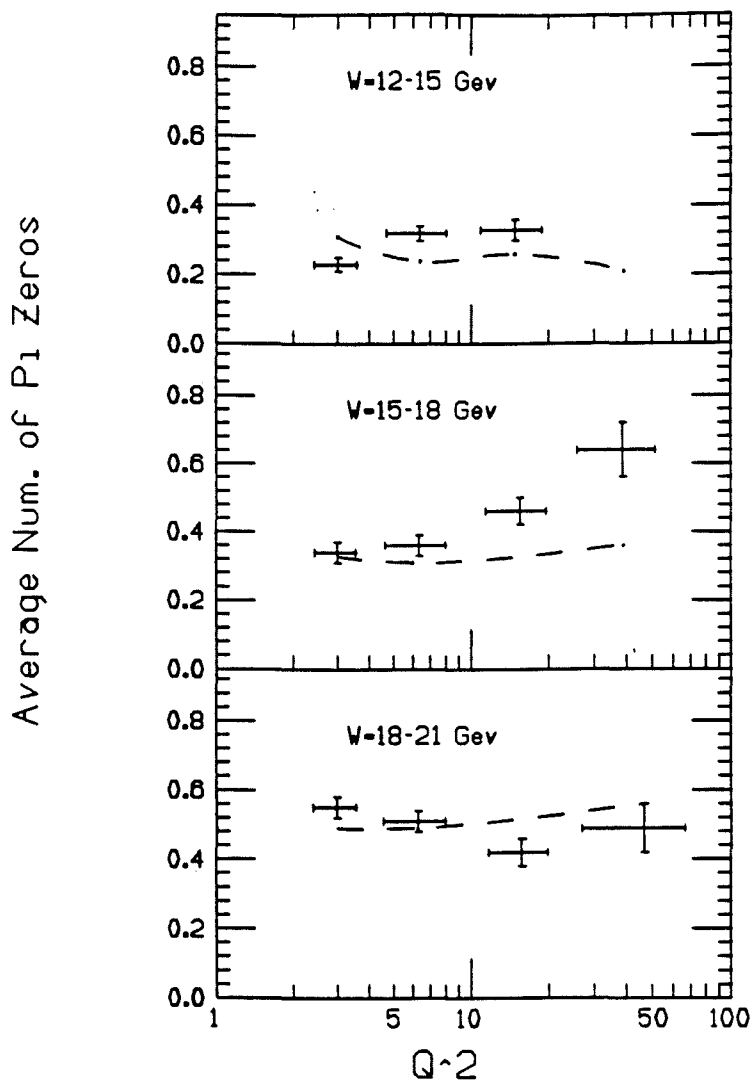Figure 58. Q^2 Dependence of Multiplicity for Fixed Ranges of W. Three ranges of W are shown. The dashed line is a Monte Carlo comparison for detectable pi zeros. No correction for geometrical acceptance has been made.

chapter are presented here. Figure 61 shows the acceptance corrected mean transverse momentum spectrum for identified pi zeros. The comparison to Monte Carlo expectations is excellent.

Table 11. Multiplicity of Pi Zeros vs. Q^2 at fixed W.

W range	Q^2 Range	$\langle Q^2 \rangle$	σ_{Q^2}	N_{evts}	N_{π^o}	$\langle N_{\pi^o} \rangle$	$\sigma_{N_{\pi^o}}$
12-15	2-4	3.01	.59	318	73	.22	.03
	4-10	6.38	1.68	533	169	.30	.02
	10-25	14.8	4.0	256	85	.34	.04
15-18	2-4	2.99	.56	320	109	.34	.03
	4-10	6.34	1.68	528	189	.36	.02
	10-25	15.5	4.1	258	119	.46	.04
	25-100	38.6	12.8	98	63	.64	.08
18-22	2-4	2.98	.58	480	265	.55	.03
	4-10	6.27	1.70	603	308	.51	.03
	10-25	15.8	4.2	257	109	.42	.04
	25-100	46.6	19.8	96	47	.49	.08

Figure 62 shows the acceptance and efficiency corrected mean z spectrum for identified pi zeros. One can see that the comparison to Monte Carlo values shows that the data has a softer z spectrum than expected after correcting for acceptance and efficiency of the software. This spectrum has been extrapolated to lower energies and the exponential fit was used to obtain the mean fraction of energy occuring as neutral pions. The fit was made separately for the region below a z value of .1 and the region above because of the rapidly changing nature of the spectrum near this point. The result is 25% ± 7% where the error was obtained by varying the parameters of the integration. Note that this value is very consistent with the value found for all photons, or 27% ± 5%.
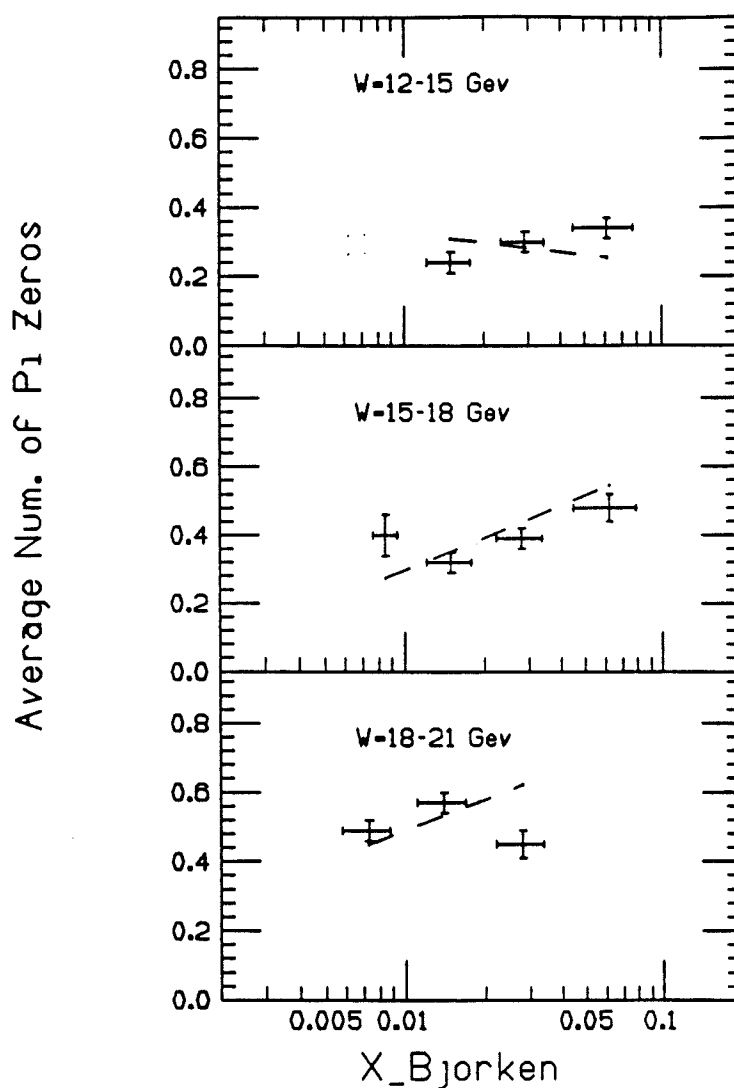
Figure 59.   Average number of identified pi zeros vs the logarithm
of x_{Bj}.   Three ranges of the variable W are shown. No correction is
made for geometrical acceptance. The dashed lines are Monte Carlo
results for detectable pi zeros.

Note that the lowest few bins in these data plots have the largest corrections

for acceptance and efficiency. Discrepencies between the data and Monte Carlo

should not be based on these points. The systematic error in the other bins is

Table 12. Multiplicity of Pi Zeros as a function of x_{Bj}.

W range	x_{Bj} Range	$\langle x_{Bj} \rangle$	$\sigma_{x_{Bj}}$	N_{evts}	N_{π^o}	$\langle N_{\pi^o} \rangle$	$\sigma_{N_{\pi^o}}$	$\langle W^2 \rangle$	$\langle Q^2 \rangle$
12-15	.01-.02	.0156	.0028	280	66	.24	.03	189	2.9
	.02-.04	.0288	.0056	411	125	.30	.03	183	5.4
	.04-.10	.0608	.0160	377	130	.34	.03	179	11.6
15-18	0-.01	.0085	.0009	121	49	.40	.06	285	2.4
	.01-.02	.0150	.0029	423	135	.32	.03	272	4.1
	.02-.04	.0282	.0057	343	134	.39	.03	271	7.8
	.04-.10	.0620	.0172	250	120	.48	.04	268	17.7
18-22	0-.01	.0073	.0015	471	232	.49	.03	387	2.9
	.01-.02	.0141	.0029	499	282	.57	.03	378	5.4
	.02-.04	.0282	.0059	266	120	.45	.04	374	10.7

30%, as discussed below.

4.4.3.3 Average p_T^2 Distributions

Figure 63 shows the average square transverse momentum as a function of Feynman x. This plot shows the familiar increase in average transverse momentum for the higher energy hadrons (the so-called 'seagull' effect), reflecting the higher probability of their emitting a gluon.

Figure 64 shows the same data after correcting for geometrical acceptance and efficiency of finding the pi zero. The increase in this plot is less rapid than accounted for by the Lund model. However, the acceptance and efficiency corrections for transverse momentum are largest at small p_T values (see Fig. 48),
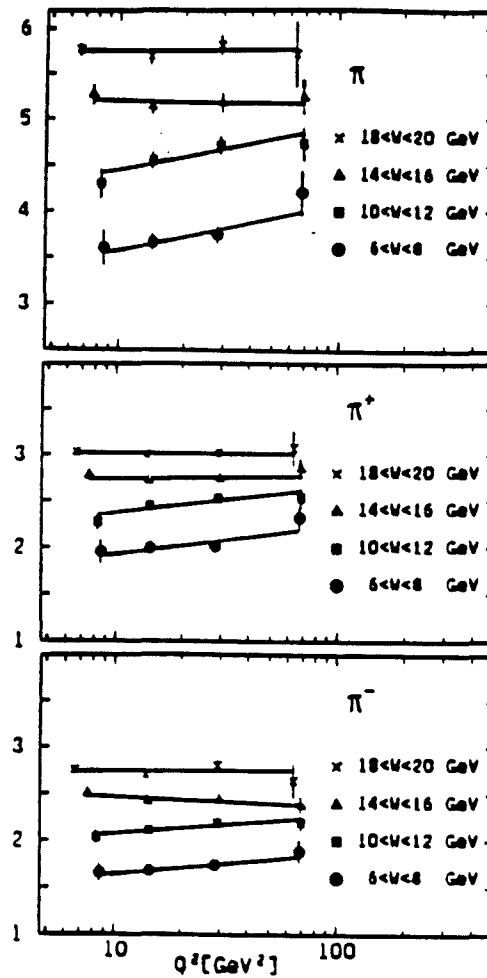
Figure 60.   EMC Result for Q^2 dependence of Pi Zero Multiplicity. The figure is taken from Ref. 7.

and if there are uncertainties in this procedure, then they may account for an

artificially lowered average.

No significant dependence on W^2 was seen for the seagull distribution.

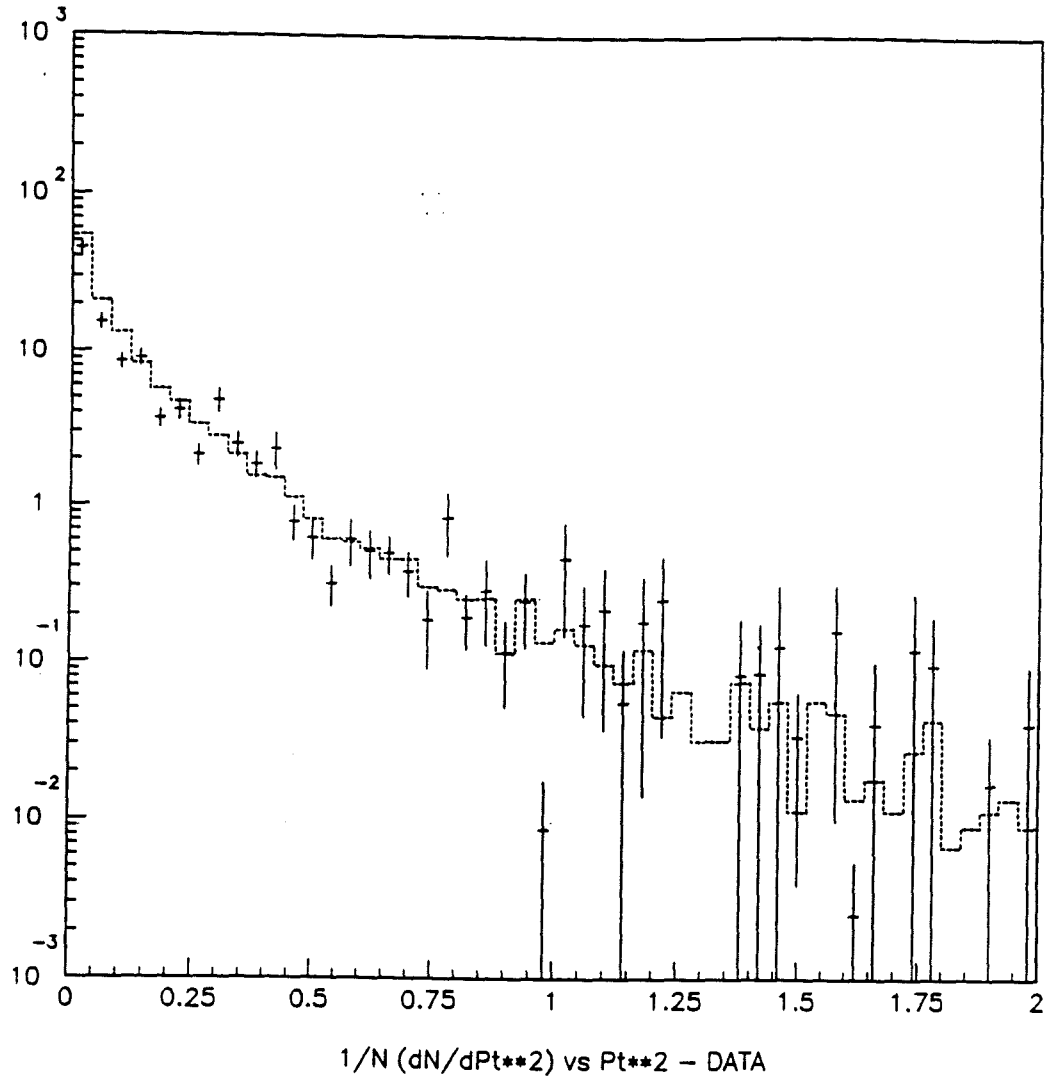Figure 65 shows the expected flat distribution of the transverse momentum

Figure 61. Normalized p_T Spectrum for Identified Pi Zeros. Data is corrected for acceptance and efficiency and has been normalized to the number of events. Dashed line is comparison with Monte Carlo for all produced pi zeros.

with respect to Q^2.

Figure 66 shows that there is no significant difference in average transverse momentum at the largest values of W. That dependence was found to exist at
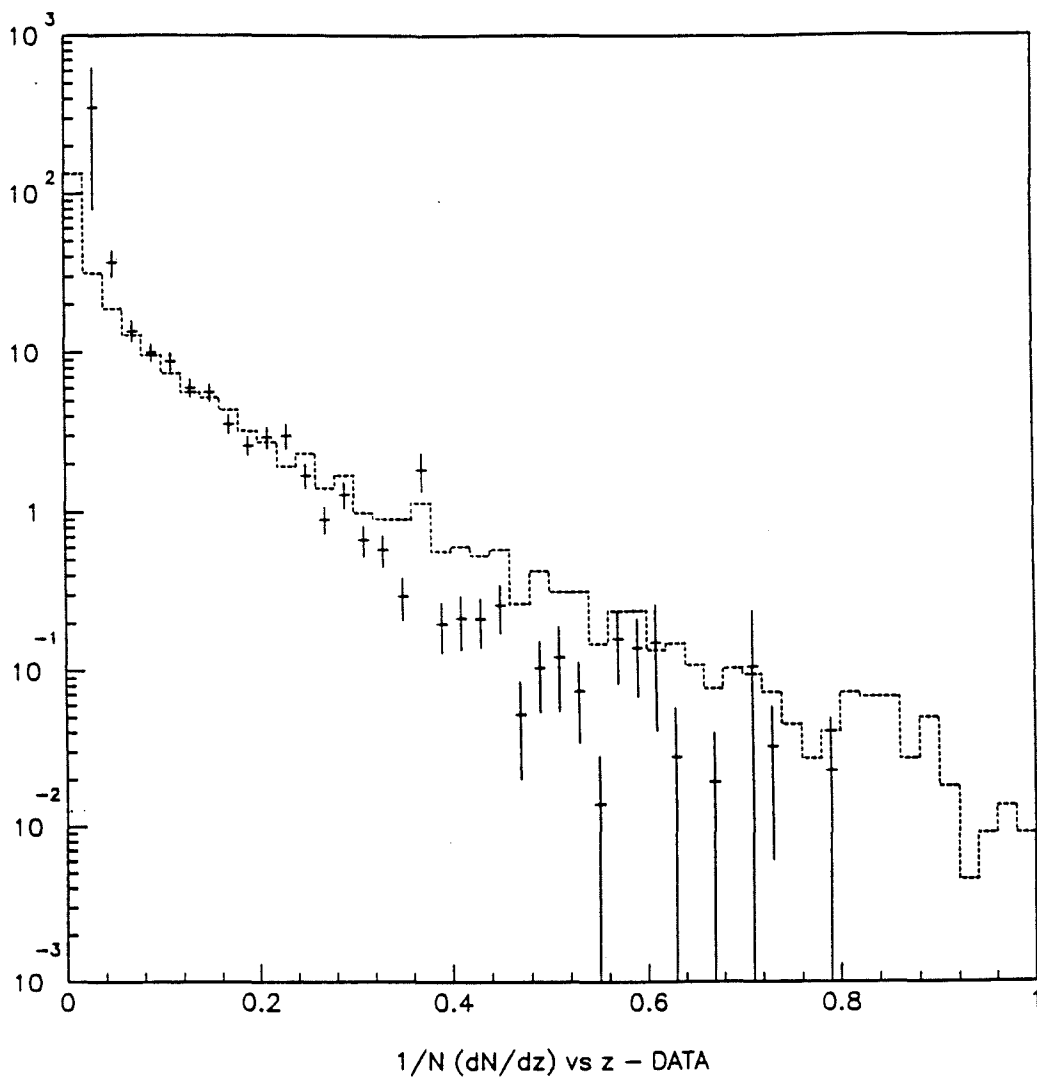
1/N (dN/dz) vs z — DATA

Figure 62. Normalized z Spectrum for Identified Pi Zeros. Data is corrected for efficiency and acceptance and has been normalized to the number of events. The dashed line is a comparison with Monte Carlo for all produced pi zeros.

a low level in EMC. [14]

4.4.3.4 Azimuthal Angle of Production

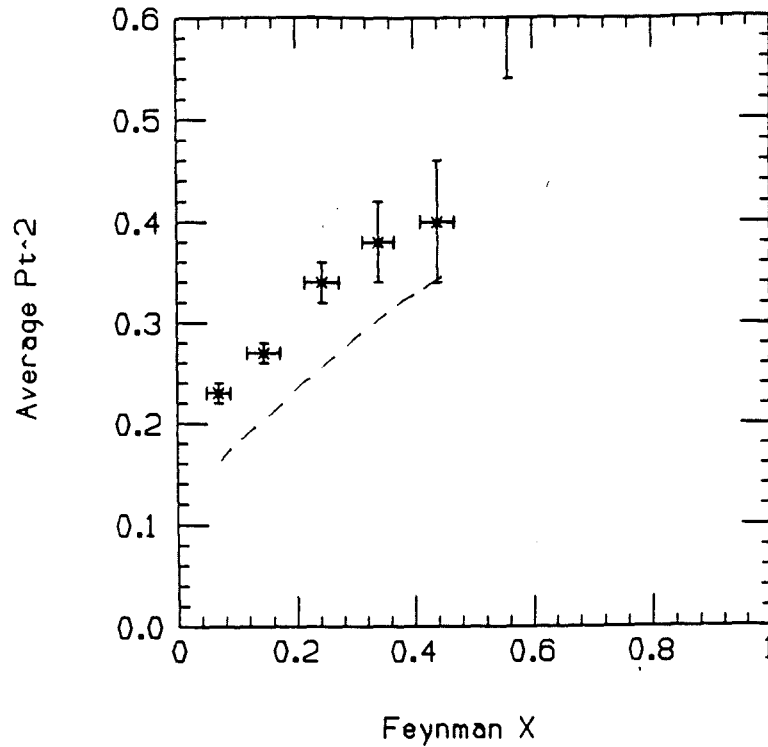Figure 67 shows the distribution of the azimuthal angle of production for

Figure 63. Average p_T^2 vs Feynman x. The dashed line is from the Lund Monte Carlo for detectable pi zeros.

identified pi zeros. As can be seen, the angle of production is very flat, with no correlation to the lepton plane of production.

Figure 68 shows the average cosine of the azimuthal angle as a function of Feynman x. Reference 7gives evidence that charged hadrons have a negative asymmetry in this angle as x_F increases positively. No such asymmetry is seen in this thesis' data for seperated pi zeros. This was verified for the sample of events where there are only two neutral clusters in the calorimeter. (That sample has a higher percentage of correct identification of pi zeros using the algorithm described in the previous section.)
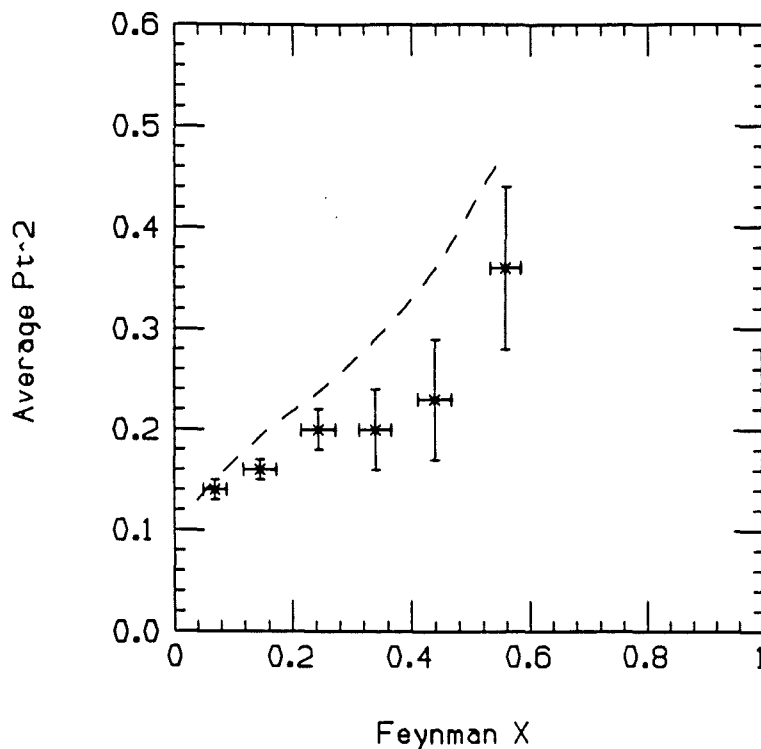
Figure 64. Corrected Average p_T^2 vs Feynman x. This data has been corrected for acceptance and efficiency. The dashed line is the Lund Monte Carlo comparison for all produced pi zeros.

4.4.4 η Production

Yields from electron-positron annihilation experiments at similar center of mass energies to the data in this thesis indicate that the π^o to η production ratio, after extrapolating to zero energy of production, should be approximately 10 to 1. [34-36] An early Kaon-proton scattering experiment found a ratio of production of 5.5, obtained from an invariant mass plot. [37] The Lund Monte Carlo I used also indicates there should be a 10 to 1 pi zero to eta multiplicity. For those mesons passing the acceptance of the calorimeter, the ratio should be
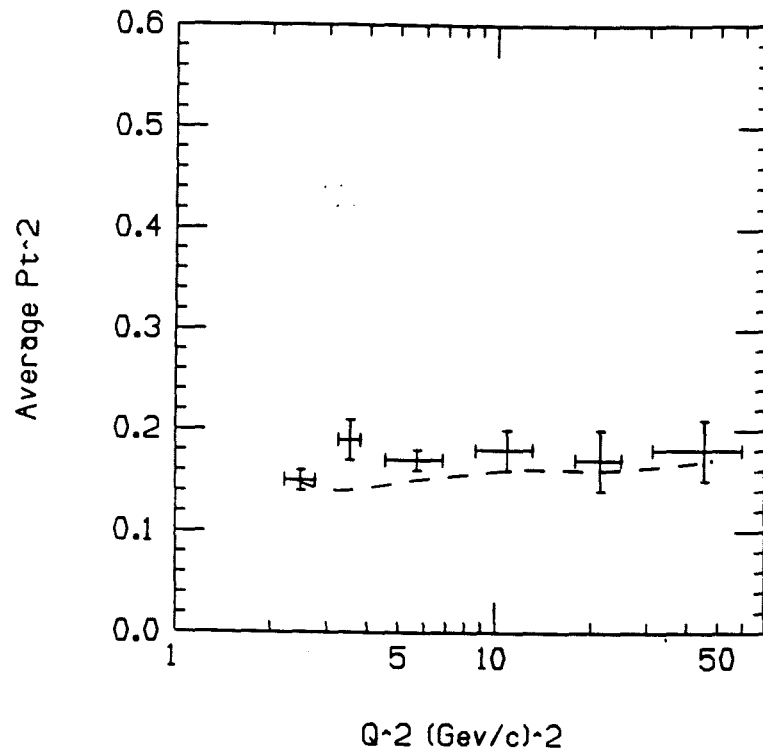
Figure 65. Corrected Average p_T^2 vs Q^2 This data has been acceptance and efficiency corrected. The dashed line is from the Lund Monte Carlo for all produced pi zeros.

on the order of 13 to 1.

Because of this reduced yield the signal for the eta is very difficult to see. In fact, the signal is only present in our data when the number of neutral clusters in an event is limited to 2. If more clusters are allowed to be present, then the combinatorial background increases far more than the signal.

Figure 69 shows the presence of both the pi zero and the eta in the same set of events. The signal in the eta mass region is approximately 2 standard deviations away from an estimated background and there may be a chance that
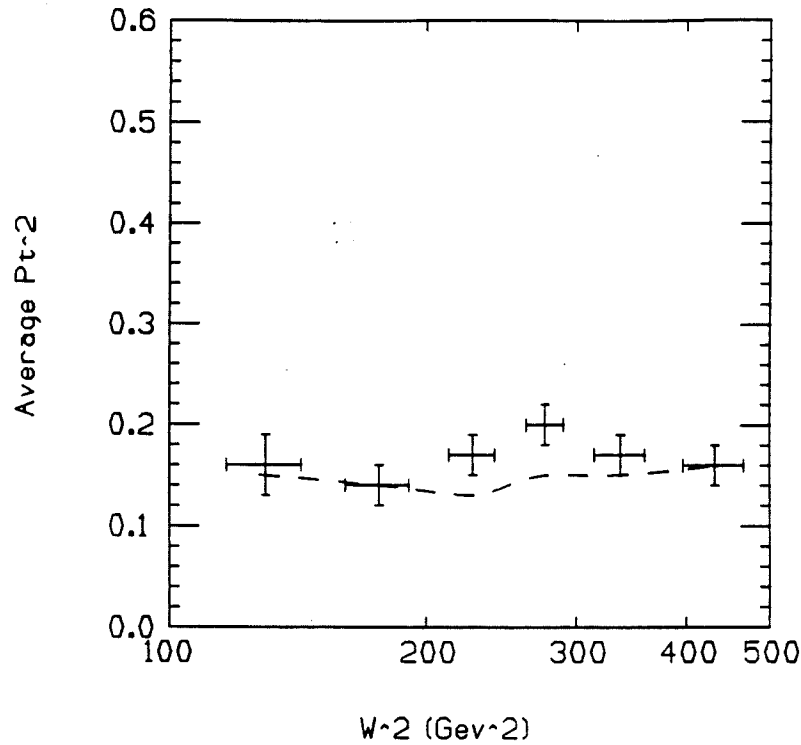
Figure 66. Corrected Average p_T^2 vs W^2 This data has been corrected for efficiencies and geometrical acceptances. The dashed line is Monte Carlo results for all pi zeros.

it is only a statistical fluctuation. However, the chance that this fluctuation would occur at the eta mass is small. If a polynomial is fit to the background data, the significance of the excess at the eta mass region remains the same. This excess of events in the eta mass region does not occur in the GEANT simulation, even though it has a better resolution than the physical device. The yield of pi zeros in the set of 1113 events passing the two cluster cut is 250 ± 25, while the number of excess events in the eta mass region is 42 ± 10. If all of these events are etas, then the ratio of the two yields is 6.0 ± 1.5. The prediction
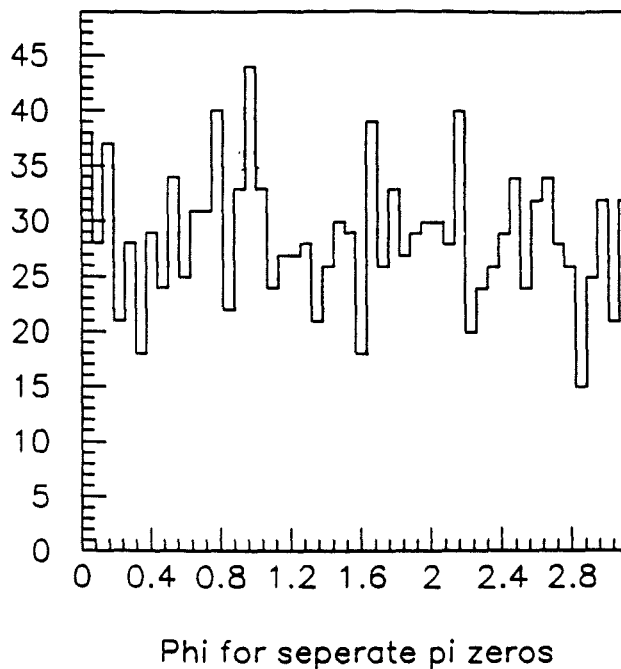
Phi for seperate pi zeros

Figure 67. ϕ for identified pi zeros. The azimuthal production angle for pi zeros.

for the observable pi zero to eta production ratio in the Lund Monte Carlo for the same size set of two cluster events is $\frac{245\pm12}{14\pm3} = 18 \pm 4$. The data thus may show a factor of two to three too many etas with the same number of pi zeros predicted by the Lund model.

The strict cut on the number of allowable calorimeter clusters biases the data sample. In Fig. 70 we see that the bias slightly favors lower W^2 and lower ν. This also shows up as a bias toward higher Bjorken x. This bias is understandable because the number of particles produced, and thus clusters, increases with W^2. An upper limit on the number of clusters will thus affect
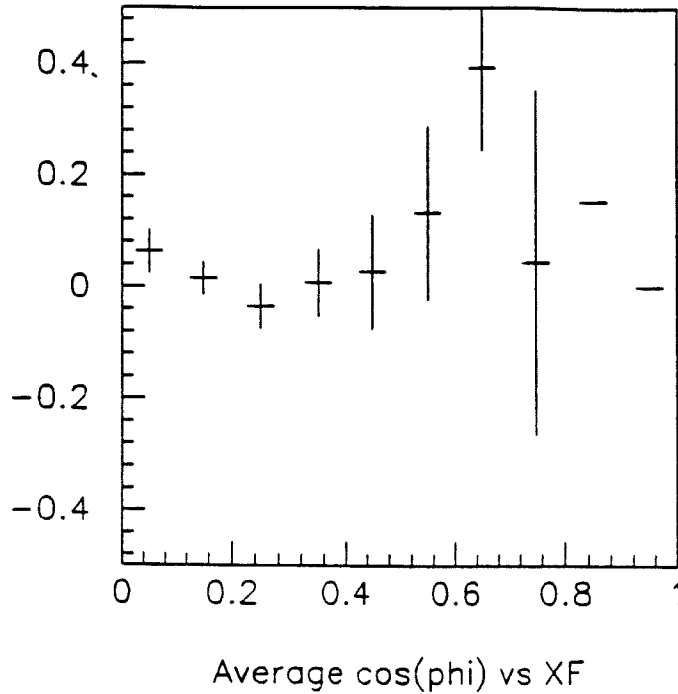
Figure 68. Average cos(ϕ) vs Feynman x. The mean cosine of the angle ϕ is plotted with respect to Feynman x for non-merged pi zeros.

higher W^2 more than lower. No significant bias occurs in the number of charged tracks in the event, however. Note that demanding two neutral clusters in the calorimeter biases the event toward middle range calorimeter energies, as would be expected.

The bias in selecting events with only two neutral clusters was found not to bias the energy or transverse momentum of the pi zeros in any fashion. Since the production of pi zeros in the Monte Carlo is both more numerous and well verified by the data in this thesis, it was therefore used to estimate the bias in eta production as well. No bias in the event variables for the two cluster sample
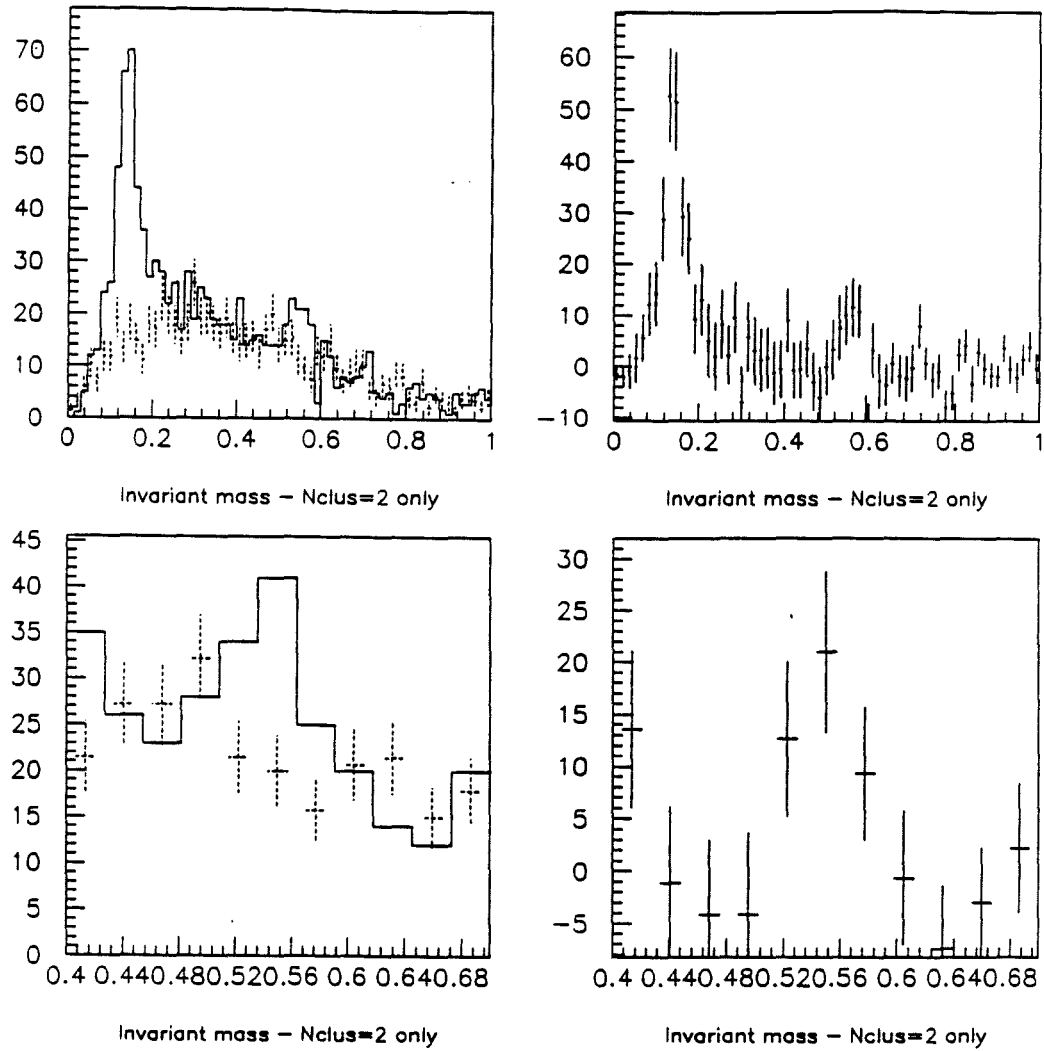
Figure 69. Eta Signal in the Invariant Mass Spectrum. a) Invariant mass spectrum for events having two neutral clusters, b) background subtracted mass spectrum, c) mass spectrum in the eta mass region, d) background subtracted mass spectrum in the eta region.

was seen for the eta mass region.

Figure 71 shows that the average pi zero multiplicity in two cluster events does not increase as a function of W^2 but instead is constant or even decreases.
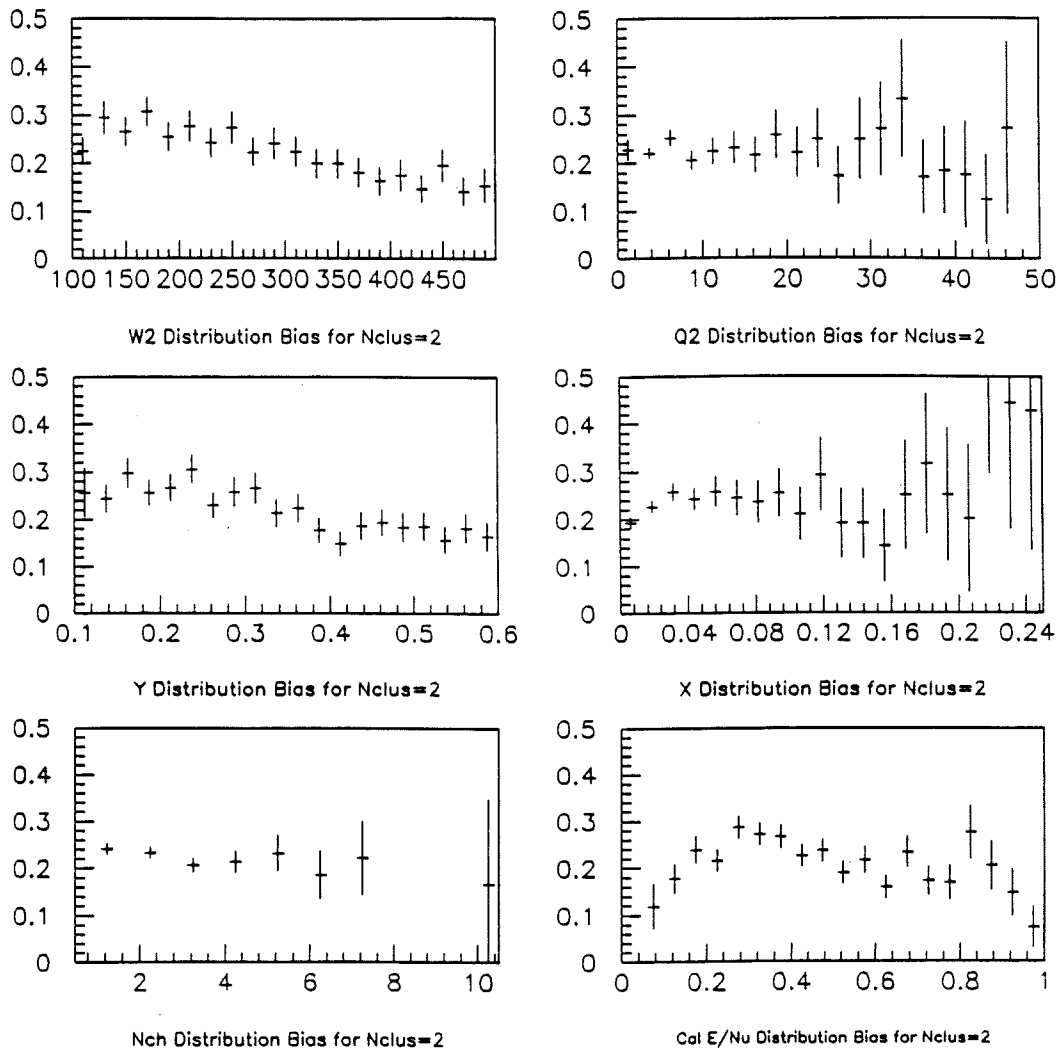
Figure 70.   Bias in Event Kinematics for Events Having 2 Neutral Clusters.   Fraction of events having only 2 neutral clusters as a function of a) W^2 b) Q^2 c) y d) x e) number of charged tracks and f) fraction of ν as energy in calorimeter.

This behavior is predicted by the Lund Monte Carlo but the magnitude of the decreased yield at high W is larger than predicted. (The reason for the expected slight decrease in multiplicity with W^2 is due to the greater chance

of background photons at greater center-of-mass energies.) I have limited the

data to the W^2=100 to 300 GeV^2 range where the cut on the number of neutral

clusters gives a flat acceptance. Table 13 gives the data shown in Fig. 71.

Figure 71. π^o Multiplicity for Two Cluster Events vs $\ln(W^2)$. Dashed line is Lund Monte Carlo values for detectable pi zeros. This data has not been corrected for geometrical acceptance.

Table 13. Multiplicity of Pi Zeros as a function of W^2. For events having two neutral clusters only.
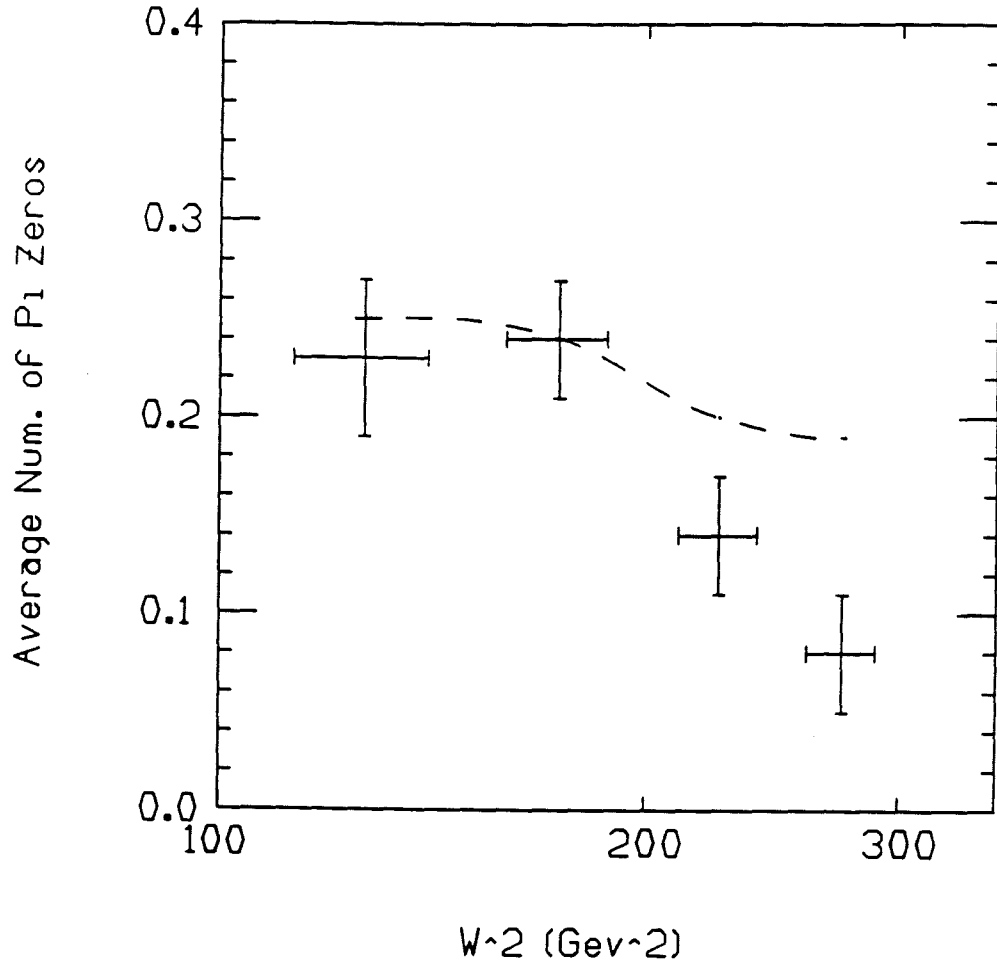
W^2 Range	$\langle W^2 \rangle$	σ_{W^2}	N_{evts}	N_{π^o}	$\langle N_{\pi^o} \rangle$	$\sigma_{N_{\pi^o}}$
100-150	126	14	174	40	.23	.04
150-200	174	14	225	54	.24	.03
200-250	225	14	164	23	.14	.03
250-300	274	15	138	11	.08	.03

The number of eta's was obtained by binning the mass spectrum in 7 bins between 200 and 700 Mev. The excess of pairs in the 500-600 MeV bin over an estimated linear background was used as the definition of the signal. The result is shown in Fig. 72 where the excess of events, assumed to be an eta signal, shows up more prominently at higher W.

In Fig. 73 the average eta multiplicity calculated in this manner shows a distinct increase with $\ln(W^2)$, not predicted by the Lund Model. The slope of this dependence on $\ln(W^2)$ is .08 ± .01 and shows that etas may be preferentially produced at higher values of W^2 than pi zeros in the same sample.

Table 14 gives the data shown in Fig. 73.

4.4.5 Systematic Errors

4.4.5.1 Multiplicities

The data presented in this thesis for multiplicities of pi and eta mesons was obtained from invariant mass plots where the background was estimated from
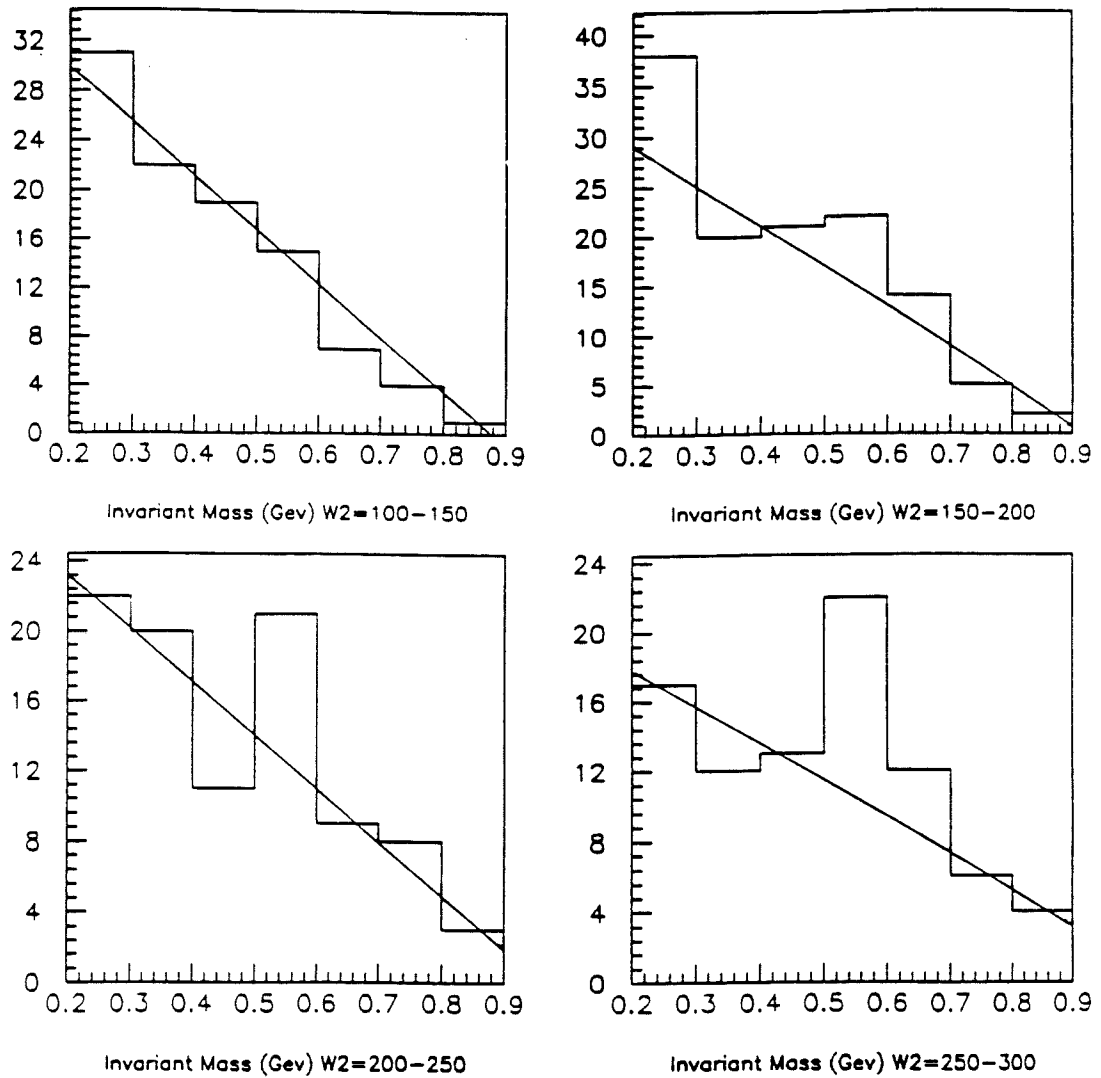
Figure 72. Invariant Mass Spectrum in the Eta Region. Four ranges of W^2 are shown. The straight lines are estimates for background levels.

random combinations of pairs of clusters in the data. Systematic errors in this method are as follows:

- Background shape: As can be seen in the spectrum for all pairs of clusters (see Fig. 53), the shape of the background estimation does not follow
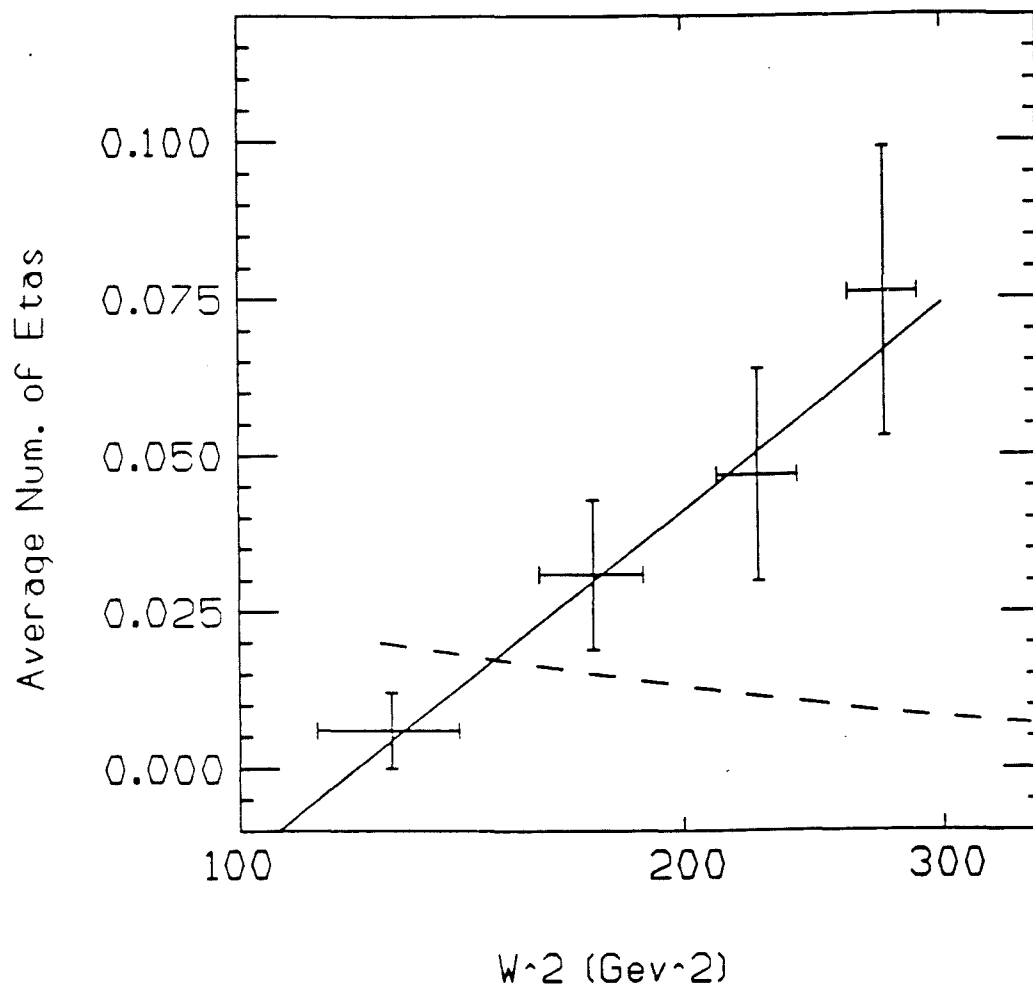
Figure 73. Average Eta Production vs logarithm of W^2. The straight line fit has a slope of .08 ± .01 and an intercept of -.39 ± .11.

exactly the shape of the true spectrum, especially at higher masses. This

is probably due to the fact that combining clusters from different events

will yield a systematically larger seperation between clusters if the virtual

photon direction differs. The number of pi zeros obtained from back-

Table 14. Multiplicity of Etas as a function of W^2. For events having two neutral clusters only.

W^2 Range	$\langle W^2 \rangle$	σ_{W^2}	N_{evts}	N_η	$\langle N_\eta \rangle$	σ_{N_η}
100-150	127	14	171	1	.006	.006
150-200	174	14	225	7	.031	.012
200-250	225	14	170	8	.047	.017
250-300	274	15	144	11	.076	.023

ground subtraction of a GEANT produced mass spectrum was compared with the known number of pi zeros produced in that set of data. It was determined that the method of background subtraction can overestimate the number of true pi zeros by up to 26% in this sample. The error for the data presented here may be smaller because any smearing of the mass spectrum due to poor energy resolution will result in a background estimation that does not differ as much from the true spectrum, especially in the lower mass region. However, the value of 26% will be used for this portion of systematic error.

• Background level: In studying the comparison between background estimates and the true invariant mass spectrum, it was found that there is an ambiguity as to the relative normalization. Estimates for the relative normalization varied by as much as 5%. It was decided that the simplest normalization would be 1.0 (i.e. the same number of entries in both the

background and the true mass plots). This yielded the best results. However, this arbitrary normalization leads to a $\pm$ 5%systematic error in the result for the yield.

- Histogram binning: A study was made as to the dependence of the pi zero yield measurement as a function of bin size in the invariant mass plot. It was determined that this ambiguity leads to an error of $\pm$ 2.5%in the result.

- Cluster miminum energy cut: No clusters smaller than 4 GeV were used in the invariant mass plots. However, due to the energy resolution of the calorimeter, sometimes incident photons that are larger than 4 GeV may have energy in the calorimeter that fluctuates below 4 GeV. A study was made to determine the effect of this phenomenon. It was determined that as much as 5%of clusters above 4 GeV could fluctuate below this limit.

- Tracking cut: Clusters closer than 6 cm. to an extrapolated track were declared as charged. It was estimated that less than 5%of neutral clusters randomly happen to lie that close to a charged track.

- Inefficiencies in tracking: If the tracking is inefficient at the 50%level, and if approximately one-third of charged hadrons shower in the calorimeter and if charged clusters are randomly distributed in the mass spectrum, then this can result in a 1%change in the pi zero multiplicity.

- Calibration of calorimeter: If the calorimeter calibration is changed by as

much as 10%, the change in yield is approximately 1.5%, due to the large mass region counted as pi zeros.

- Gas Gain: Not accounting for changes in gas gain can change the calibration by as much as 10%. Thus this effect contributes to the systematic error as much as the error in calibration, or 1.5%.

These effects, added together as independent systematic effects, yield a total systematic error of 28%. The systematic error defined for the multiplicity data in this thesis is 30%. This error is added in an independent fashion to the statistical errors quoted in the data.

4.4.5.2   Pi Zero Properties

To determine specific properties of pi zeros, it is necessary to identify the individual photons arising from their decay. The software to do this was discussed above. Various systematic errors are associated with this process. Systematic errors also occur in the definition of the event kinematics, which subsequently define the pi zero properties. The magnitude of these effects are as follows:

- Event kinematics error: From a simple study, it was found that the average of 10% error in event kinematics can result in up to 7% errors in a typical z or W^2 bin population.

- Pi Zero reconstruction error: From both Monte Carlo and calibration data, the error in the energy of individual clusters on average lies between 15 and 20%. As shown in Fig. 49, this error yields on average an ap-

proximate 10%error in reconstructed variables such as z p_T and Feynman x.

- Acceptance and efficiency correction: Depending on binning and statistical significance, the corrections for acceptance and efficiency of the pi zero finding software in the most significant bins (i.e. the most populated) can vary by up to 25%.

These three systematic errors taken, as independent, yield a total of 28%systematic error. The systematic error defined for pi zero property measurements is 30%for this thesis.

5. Summary and Discussion

In this thesis, the production of pi zero and eta mesons in deep inelastic muon scattering was discussed. The calorimeter used to identify these mesons was a lead/proportional tube sampling calorimeter with $\frac{44}{\sqrt{E}} + 7\%$ resolution for electromagnetic clusters. Invariant mass spectra were used to determine multiplicities as a function of event variables. The systematic error in this method is approximately 30%. To determine individual properties of the mesons, a set of software was used to tag pairs of clusters arising from their decay. The efficiency of this software was on the order of 40% for pi zeros decaying into the calorimeter acceptance. The background of misidentified pi zeros was on the order of 35%. Using Monte Carlo acceptance corrections, the estimated systematic error on the results for pi zero properties was approximately 30%.

The average multiplicity of pi zeros in the data sample studied was 5.9 ± .7 ± 1.8, which is within limits of error of the Lund prediction of 5.1. It was found that the average multiplicity of pi zeros increases linearly with the logarithm of W^2, with the slope of that dependence being 1.49 ± .39 ± .45 in the center of mass system. This value is very consistent with Monte Carlo expectations given the level of statistical and systematic uncertainty. In the same sample of data, the charged track production in the same forward region shows a dependence on W^2 that is more than twice as steep as for the neutral pions. However, no systematic study was made for these charged tracks.

No significant Q^2 dependence was found for pi zero production in nucleon fragmentation for the data averaged over all W^2, although an increase was seen at a Q^2 value of 28 $(GeV/c)^2$. This increase is consistent with QCD scale violations. The Q^2 dependence of the pi zero multiplicity matched Lund Monte Carlo expectations very well.

A significant change in the average pi zero multiplicity was seen as a function of both Q^2 and Bjorken x when the W^2 range is limited. For the lowest W range, the multiplicity rises with the variable while at the highest W range, the production of neutral pions occurs at a lower rate than expected. The source of this effect is not understood but similar behavior been seen in another experiment for charged particles. This effect is not seen in the Lund Monte Carlo for most of the data but could be due to scaling violations from excess gluon emission for the large Q^2 data. The effect is most pronounced for the lower values of W studied.

The transverse momentum spectrum of identified pi zeros follows Monte Carlo expectations very well. The z spectrum of pi zeros is softer than expected, however. This is true also for the z spectrum of all observed photons, regardless of origin, and may indicate that there are more soft photons than expected. After extrapolating and integrating the mean z spectrum to zero values, it was determined that, on average, 27%$\pm$ 5%$\pm$ 8%of the energy in an event shows up as photons. The same method applied to the π^o z spectrum yields 25%$\pm$ 7%$\pm$

8%.

The average transverse momentum shows no significant increase with respect to Q^2 or W^2. The increase in transverse momentum of pi zeros with respect to the variable x_F is slower than expected. However, the corrections made for detection efficiency and geometrical acceptance may artifically lower the data.

No asymmetry is seen in the azimuthal angle of production for the entire range of Feynman x even though this asymmetry has been seen in charged pion data.

A signal in the eta mass region was observed in those events that had only two neutral clusters. This observation was not expected from Monte Carlo expectations and previous experiments. This signal is reduced by a factor of 6.0 ± 1.5 ± 3.0 from observable pi zeros in the same sample. If this signal is due to eta meson production, then the eta yield is approximately 2-3 times larger than predicted by the Lund Monte Carlo, detailed theoretical calculations and comparisons to results from e+e- annihilation experiments. The pi zero yield is consistent with the Monte Carlo. An unexpected logarithmically increasing dependence on W^2 was seen for the average eta multiplicity in this restricted data sample while the pi zero multiplicity decreased faster than expected. The slope of the average identified eta multiplicity as a function of of the logarithm of W^2 is .08 ± .01 ± .03.

This result indicates, with a large degree of statistical uncertainty, that eta mesons are produced preferentially to pi zero mesons at higher center of mass energies in the very deep inelastic region studied in this experiment. There could be two sources of this effect. At high values of W^2, and low values of Bjorken x, the virtual photon is probing deeper into the virtual 'sea' of quarks and gluons. An enhancement of eta production over pi zero production at this level may reflect the greater chance that a strange or anti-strange quark absorbs the energy of the photon and this quark may preferentially fragment into eta mesons, which contain a strange component.

Alternatively, it may not be the primary quark identity that determines what type of meson is produced. Instead, at very large values of center-of-mass energy, the surrounding medium may be the determining factor. No enhancement of eta production is seen in the comparatively clean reaction of electron-positron annihilation, while the data shown here indicates there may be such an enhancement inside a nucleon. This may indicate that the fragmentation of the color field into hadrons is influenced by its surroundings.

REFERENCES

1. R. Francis and T. Kirk, Physics Reports, 54, 5, (1979)

2. J.D. Bjorken, Physics Review, D9, (1974)

3. J. Drees, H. Montgomery, Annual Review of Nuclear and Particle Sciences, 33, 383-452, (1983)

4. J.D. Bjorken, E.A. Paschos; Physical Review; 185, 5; (1969)

5. S. Dasu, et.al.; Physical Review Letters; 61; p. 1061; (1988)

6. T. Sloan, G. Smadja and R. Voss, Physics Reports, 162, 2 and 3, p. 45-167 (1988)

7. N. Schmitz, "Hadron production in High Energy Lepton-Nucleon and Lepton-Nucleus Collisions", International Journal of Modern Physics A; vol. 3, number 9; p. 1997; (1988)

8. D. Perkins, "Proceedings of a Nato Advanced Study Institute on Techniques and Concepts of High-Energy Physics", Plenum Press, 279-334, (1981)

9. C. Quigg, "Gauge Theories of the Strong, Weak and Electromagnetic Interactions", Benjamin/Cummings, (1983)

10. G. Altarelli, R. K. Ellis, G. Martinelli; "Processes Involving Fragmentation Functions Beyond the Leading Order in QCD"; Nuclear Physics B; 160; p. 301; (1979)

11. J. Ashman, et. al.; "A Measurement of the Spin Asymmetry and Deter-

mination of the Structure Function G(1) in Deep Inelastic Muon - Proton Scattering."; Physics Letters B; 206; p. 364; (1988)

12. M.F. Gari, N.G. Stefanis; "Determination of the Scale Parameter Lambda from Elastic Electron-Proton Scattering at High Q**2"; Physics Letters B; 187; p. 401; (1987)

13. M. Arneodo, et.al.; "Measurement of Hadron Azimuthal Distributions in Deep Inelastic Muon Proton Scattering"; Zeitschrift fur Physik C; 34, p. 277; (1987)

14. J.J. Aubert, et.al.; "Production of π^o Mesons in Muon-Hydrogen Interactions at 200 GeV"; Zeitscrift fur Physik C; 18; p.189; (1983)

15. T.P. McPharin, et.al.; "Inclusive π^o Electroproduction in the Deep Inelastic Region"; Physics Letters B; 90; number 4; p.479; (1980)

16. S.J. Wheeler; "A Study of Neutral Pion and Omega Meson Production by 280 GeV/c Muon-Proton Scattering"; Ph.D. Thesis; University of Sheffield; December, 1985

17. J.G. Williamson; "Neutral Pion Production and Single Photon Asymmetries in Deep Inelastic Muon Scattering"; Ph.D. Thesis; University of Sheffield; March, 1985

18. M.R. Adams, et. al.; "A Spectrometer for Muon Scattering at the Tevatron"; submitted to Nuclear Instrumentaion and Methods; (April,1989)

19. S. Aid, et. al.; " An Electromagnetic Calorimeter for E665"; FNAL Gas

Sampling Calorimetry Workshop; p. 249; (1985)

20. B. Rossi, H. Straub; "Ionization Chambers and Counters: Experimental Techniques"; McGraw-Hill; New York; (1949)

21. Particle Data Group; "Review of Particle Properties"; Physics Letters B; 170; (1986)

22. C.W. Fabjan, T. Ludlum; "Calorimetry in High Energy Physics"; Annual Review of Nuclear and Particle Science; 32; p. 335; (1982)

23. T. Ferbel, "Experimental Techniques in High Energy Physics", Addison-Wesley, (1985)

24. B. Andersson, et. al.; Zeitschrift fur Physik C; 6; p. 235-240; (1980)

25. M. Bengtsson, T. Sjostrand; Zeitschrift fur Physik C; 37; p. 465-476; (1988)

26. T. Sjostrand; "The Lund Monte Carlo for Jet Fragmentation"; Lund preprint LU TP 82-3; (1982)

27. R. Field, R. Feynman, Nuclear Physics, B136, 1., (1978)

28. R.Brun, et. al.; GEANT 3 Users Guide; CERN DD/EE/84-1; (1986)

29. R. Brun, et. al.; "The GEANT3 electromagnetic shower program and a comparison with the EGS code"; CERN preprint)

30. S. Youssef, "Clustering with Local Equivalence Relations"; FSU preprint FSU-SCRI-87-02; (1987)

31. M. Arneodo, et. al.; "Multiplicities of Charged Hadrons in 280 GeV/c

Muon-Proton Scattering"; Nuclear Physics B; 258; p. 249; (1985)

32. J.J. Aubert, et.al.; "Evidence for Anomalous Prompt Photons in Deep Inelastic Muon Scattering at 200 GeV"; CERN preprint EP/88-33; (1988)

33. Aachen, et.al.; "Hadron Multiplicity with Q^2 and Scale Breaking of the Hadron Distributions in Deep Inelastic Muon-Proton Scattering"; CERN-EP/85-143; (1985)

34. S. Abachi, et.al.; "Production of η mesons in e+e- Annihilation at $\sqrt{s} = 29$ GeV"; Physics Letters B; vol. 205, number 1; p. 111; (1988)

35. W. Bartel, et.al.; "A Study of Photon Production in Hadronic e+e- Annihilation"; Zeitschrift fur Physik C; 28; p. 343; (1985)

36. H.J. Behrend, et.al.; "Measurement of inclusive γ, π^o and η Production in e+e- Annihilation at $\sqrt{s} = 35$ GeV"; DESY preprint 89-008; (1989)

37. A.C. Borg, et. al.; "Inclusive Pion and Eta Production in K-p Interactions at 14.3 GeV/c"; Nuclear Physics B; 106; p. 430; (1976)